



AFRL-RY-WP-TR-2014-0006

EXPERIMENTS ON PLASMA TURBULENCE CREATED BY SUPERSONIC PLASMA FLOWS WITH SHEAR

R.L. Stenzel and J.M. Urrutia

University of California

**APRIL 2014
Final Report**

Approved for public release; distribution unlimited.

See additional restrictions described on inside pages

STINFO COPY

**AIR FORCE RESEARCH LABORATORY
SENSORS DIRECTORATE
WRIGHT-PATTERSON AIR FORCE BASE, OH 45433-7320
AIR FORCE MATERIEL COMMAND
UNITED STATES AIR FORCE**

NOTICE AND SIGNATURE PAGE

Using Government drawings, specifications, or other data included in this document for any purpose other than Government procurement does not in any way obligate the U.S. Government. The fact that the Government formulated or supplied the drawings, specifications, or other data does not license the holder or any other person or corporation; or convey any rights or permission to manufacture, use, or sell any patented invention that may relate to them.

This report was cleared for public release by the USAF 88th Air Base Wing (88 ABW) Public Affairs Office and is available to the general public, including foreign nationals. Copies may be obtained from the Defense Technical Information Center (DTIC) (<http://www.dtic.mil>).

AFRL-RY-WP-TR-2014-0006 HAS BEEN REVIEWED AND IS APPROVED FOR PUBLICATION IN ACCORDANCE WITH ASSIGNED DISTRIBUTION STATEMENT.

//SIGNED//

SABA MUDALIAR, Program Manager
Antenna & Electromagnetic Technology Branch

//SIGNED//

TONY KIM, Chief
Antenna & Electromagnetic Technology Branch

//SIGNED//

TRACY W. JOHNSTON, Chief
Multispectral Detection & Technology Division
Sensors Directorate

This report is published in the interest of scientific and technical information exchange, and its publication does not constitute the Government's approval or disapproval of its ideas or findings.

*Disseminated copies will show “//signature//” stamped or typed above the signature blocks.

REPORT DOCUMENTATION PAGE					Form Approved OMB No. 0704-0188	
<p>The public reporting burden for this collection of information is estimated to average 1 hour per response, including the time for reviewing instructions, searching existing data sources, gathering and maintaining the data needed, and completing and reviewing the collection of information. Send comments regarding this burden estimate or any other aspect of this collection of information, including suggestions for reducing this burden, to Department of Defense, Washington Headquarters Services, Directorate for Information Operations and Reports (0704-0188), 1215 Jefferson Davis Highway, Suite 1204, Arlington, VA 22202-4302. Respondents should be aware that notwithstanding any other provision of law, no person shall be subject to any penalty for failing to comply with a collection of information if it does not display a currently valid OMB control number. PLEASE DO NOT RETURN YOUR FORM TO THE ABOVE ADDRESS.</p>						
1. REPORT DATE (DD-MM-YY) April 2014		2. REPORT TYPE Final		3. DATES COVERED (From - To) 3 December 2010 – 5 January 2014		
4. TITLE AND SUBTITLE EXPERIMENTS ON PLASMA TURBULENCE CREATED BY SUPERSONIC PLASMA FLOWS WITH SHEAR				5a. CONTRACT NUMBER FA8721-11-C-0009		
				5b. GRANT NUMBER		
				5c. PROGRAM ELEMENT NUMBER 62204F		
6. AUTHOR(S) R.L. Stenzel and J.M. Urrutia				5d. PROJECT NUMBER 4916		
				5e. TASK NUMBER HE		
				5f. WORK UNIT NUMBER Y0A9		
7. PERFORMING ORGANIZATION NAME(S) AND ADDRESS(ES) University of California Department of Physics and Astronomy Los Angeles, CA 90095-1547				8. PERFORMING ORGANIZATION REPORT NUMBER 444025-ST-25188		
9. SPONSORING/MONITORING AGENCY NAME(S) AND ADDRESS(ES) Air Force Research Laboratory Sensors Directorate Wright-Patterson Air Force Base, OH 45433-7320 Air Force Materiel Command United States Air Force				10. SPONSORING/MONITORING AGENCY ACRONYM(S) AFRL/RYM		
				11. SPONSORING/MONITORING AGENCY REPORT NUMBER(S) AFRL-RY-WP-TR-2014-0006		
12. DISTRIBUTION/AVAILABILITY STATEMENT Approved for public release; distribution unlimited.						
13. SUPPLEMENTARY NOTES PAO Case Number 88ABW-2014-0581, Clearance Date 18 Feb 2014. Report contains color.						
14. ABSTRACT <p>The turbulence created by streaming ions through a stationary plasma has been studied. The velocity of the streaming ions was selected via a biasing voltage. In situ probes were used to measure the local and time-varying plasma parameters, ion distribution functions, and the turbulence itself. Density fluctuations were recorded in time and space, Fourier transformed into frequency space and cross-correlated in space. The fluctuations were identified as ion sound modes and their growth rate was shown to depend on the beam energy. The interaction of density fluctuations with electromagnetic waves was investigated. Strong scattering of electromagnetic signals was observed when the wave was guided by a transmission line through a turbulent plasma. The effect was enhanced by forming a transmission line resonator and applying frequencies on the slope of the resonance curve. This suggests a method to eliminate the modulation of a high frequency signal by plasma turbulence. In addition a new method of generating plasma flows with shear has been devised. It is based on creating electron MHD flows with pulsed magnetic fields. Shear flow ion acoustic turbulence has been observed. The work also inspired new methods for eliminating the blackout problem.</p>						
15. SUBJECT TERMS ion sound waves, nonlinear phenomena, electron scattering						
16. SECURITY CLASSIFICATION OF:			17. LIMITATION OF ABSTRACT: SAR	18. NUMBER OF PAGES 74	19a. NAME OF RESPONSIBLE PERSON (Monitor)	
a. REPORT Unclassified	b. ABSTRACT Unclassified	c. THIS PAGE Unclassified			Saba Mudaliar	
					19b. TELEPHONE NUMBER (Include Area Code) N/A	

Table of Contents

Section	Page
List of Figures	iii
1. Summary	1
2. Introduction	2
3. Methods Assumptions, And Procedures	4
3.1 Technical Approach	4
3.2 Plasma Diagnostics	6
3.3 Generation of Ion Beams	6
3.4 Wave Diagnostics	7
3.5 Oscillating Sheath Production	9
4. Results And Discussion	12
4.1 Evidence of Ion Beam Plasma Instabilities	12
4.2 Velocity Shear Influence	12
4.3 Ion Beam Properties	14
4.4 Propagation of Test Waves and Pulses	14
4.5 Ion Beam-Plasma Instability	17
4.6 Pulsed Plasma Sources	19
4.7 Microwave Scattering	20
4.8 Oscillations in Plasma Bubbles	23
4.8.1 Sheath Instability	23
4.8.2 Sheath Resonance	25
4.8.3 Scaling of Instability with Plasma Density	26

4.8.4	Sheath Oscillation Discontinuities	27
4.8.5	Pulsed Discharges	27
4.8.6	Pulsed Grid Voltage	30
4.8.7	Triggering the Instability	32
4.8.8	Bubble Properties with an Internal Emissive Probe	34
4.8.9	Spectra with Langmuir and Emissive Probes	35
4.8.10	Electron Leakage Through Coarse Grids	41
4.8.11	Mode Jumps And Sidebands	43
4.9	Recommendations	44
4.9.1	Further Work	44
4.9.2	Proposal To Ameliorate Electromagnetic Scattering Effects	45
4.10	ALTERNATE APPROACHES	46
4.10.1	Introduction	46
4.10.2	Experimental Setup	47
4.10.3	Experimental Results	49
4.10.4	Conclusions Of This Experiment And Suggestions For Further Work	52
4.11	Recent Publications	53
5.	Conclusions	54

List of Figures

Figure	Page
1 Schematic of the Experimental Setup for Injecting an Ion Beam into a Background Plasma	4
2 (a) Photograph of the source container (inner cylinder, end view) inside the larger target plasma device (outer container with many flanges) (b) Side view of the ion beam source inside the larger target plasma device. The bright light is due to the incandescent tungsten cathode filaments. A probe is in front of the beam source	5
3 Basic plasma diagnostic and results. (a) Langmuir probe I-V characteristics with evaluation of electron temperature, density and plasma potential. (b) Dependence of density on discharge current and axial magnetic field.	5
4 Identification of an ion beam from the current-voltage characteristics and its derivative of a plane Langmuir probe.	7
5 (a) Ion velocity analyzer traces for different beam energies and (b) ion energy distributions obtained from the derivative of the above I-V curves.	8
6 Schematic picture of the microwave resonator probe for studying the scattering of electromagnetic waves by density fluctuations.	8
7 (a) Schematic diagram of the plasma bubble experiments with typical plasma parameters. (b) Photographs of two spherical grids with different mesh sizes which exhibit different probe I-V characteristics. The coarse mesh leaks electrons even when the bias should reflect all energetic electrons.	10
8 (a) Schematic setup to produce and diagnose pulsed plasma bubbles in an ambient discharge plasma. (b) Schematic diagram of tuning a parallel $L - C$ resonance circuit to harmonic lines of the sheath instability. (c) Logarithmic plot of the spectrum of $I_{\text{grid,rf}}$ with multiple harmonics. Top line is the full spectrum without circuit. Below are spectra where the high impedance circuit tunes out lines of successively higher harmonics without affecting the other lines.	11
9 Fluctuation spectrum of the probe current in the presence of ion beams with different velocities. The fluctuations lie in the ion acoustic branch and were created by the ion beam. The spectrum and intensity of ion sound turbulence depended on beam velocity: for very slow beams the noise was negligible. The amplitude was largest for beam velocities of a few times the sound speed. The fluctuations decrease again for very fast beams.	12

10	(a) Instantaneous fluctuation at edge of mica sheet (extending from $r=0$ to $r=4.6$ cm) blocking the ion beam, (b) its power spectrum (blue), together with the average power spectrum over many single observations (black), and (c) spatial variation of average power spectrum as the probe is swept radially away from behind the obstruction to the edge of the ion beam column at $r=10$ cm.	13
11	Ion distribution function at different axial distances z from the beam source. The traces were taken in 0.5 cm increments. The insert shows the ion beam density decay. The beam decay was partly due to scattering from ion sound turbulence and partly due to ion charge exchange collisions.	14
12	Propagation of a test wave excited by a modulation of the beam velocity. Waveforms detected in 0.5 cm axial increments showing a continuous propagation delay. The propagation speed ($v = f \times \lambda \simeq 3.6 \times 10^5$ cm/s) was supersonic and close to the beam velocity, hence the wave is a fast beam mode.	15
13	Propagation of a density pulse created by modulating the beam velocity with a 10 μ s pulse. (a) Waveforms of the density perturbation in the target plasma at different axial distances from the beam injection point. The density perturbation grew initially, which indicates a convective instability. The perturbation decayed when the beam was scattered. (b) Time-of-flight diagram showing the propagation velocity was close to the sound speed, $v \simeq 2 \times 10^5$ cm/s.	15
14	Dependence of pulse amplitude on different parameters. (a) Density perturbation as a function of pulse amplitude, which modulated the beam velocity. For strong modulations the normalized density perturbation $\delta n/n \propto \delta I_e/\langle I_e \rangle$ could reach 30%. (b) Density perturbation at a fixed position ($z=5$ cm) for different ion beam velocities, showing an optimum growth when the beam velocity was slightly faster than the sound speed.	16
15	Noise waveform (a) and spectrum (b) of the ion-beam plasma instability ($V_{\text{beam}} \simeq 4$ eV, $f_{p,i} \simeq 1$ MHz). A smoothed (red) line was been added to the spectrum.	16
16	Cross correlation functions vs time at different axial probe separations. The peak shifted in time indicating propagation along the beam at a velocity $\Delta z/\Delta t \simeq 5 \times 10^5$ cm/s.	17
17	Growth and decay of the fluctuation amplitude (a) and spectrum (b) vs axial position.	18
18	Ion distribution functions (a,b) and noise spectra (c,d) for different beam energies.	18

19	Ion beam-plasma instability in a pulsed target plasma. (a) Electron saturation current of a plane Langmuir probe showing density rise and fall for different peak discharge currents. (b) Density fluctuations on an rf probe showing large amplitudes in the early discharge and in the afterglow where the ratio of ion beam density to background ion density is large.	19
20	Ion beam-plasma instability in a pulsed target plasma for different steady-state source plasma densities. (a) Density fluctuations during the rise of the target discharge for different ion beam densities, controlled by the source discharge current. (b) Rise of plasma turbulence on ion beam density. . . .	20
21	Principle of detecting density fluctuations with a microwave resonator probe. (a) Measured resonance curves at two different plasma densities. (b) Amplitude change for a density pulse when the microwave frequency was tuned to the low frequency side of the resonance curve (f_1). (c) Reverse sign for the amplitude change occurs when the microwave frequency was tuned to the high frequency side of the resonance curve (f_2).	21
22	Shift of the resonance line with target plasma density. (a) Line plots showing also the slope of a resonance curve. (b) Contour plot of the above lines which yields the slope, dn/df . The absolute density fluctuations can be determined from the slopes dV/df and dn/df	22
23	Microwave measurement of a density pulse for different ion beam energies. (a) Ion velocity analyzer traces for different beam energies. (b) Density perturbation measured with the microwave resonator at $z = 5$ cm from the beam source vs time and beam energy. The largest growth and amplitude occurs for a 4 eV beam.	23
24	(a) Resonance curves in a quiescent and a noisy background plasma. (b) Spectrum of the microwave signal tuned to the slope of the resonance line in a noisy plasma.	23
25	Microwave spectra effected by density fluctuations. (a) Natural line width of the microwave source. (b) Line spectrum in a quiescent plasma. (c) Line spectrum broadened by plasma turbulence.	24
26	Growth of density fluctuations with magnetic field.	24
27	Sheath oscillations at different negative grid voltages. (a) I-V characteristics of the 8 cm diam grid. Insert shows waveform and spectrum of the grid current oscillations at the floating potential ($I_{\text{grid,dc}} = 0$). (b) Frequency of the sheath oscillations vs dc grid voltage.	25

28	Excitation of the sheath oscillation with a tone burst. (a) Probe signal inside the bubble exhibits a long-lasting ringing at the instability frequency. (b) A probe outside the bubble observed no ringing response or instability. (c) Tone bursts of different frequencies excite a sharp resonance in the bubble but (d) no resonance in the ambient plasma.	25
29	Mode change from a virtual anode mode to a bubble volume oscillation. (a) Spectrum of grid oscillations vs density. The grid voltage is much larger than the discharge voltage, hence repels all electrons at low densities. But as the density increases the Debye length becomes smaller than the grid opening and electrons enter into the bubble which changes the spectrum and (b) lowers the potential inside the bubble.	26
30	Bubble and instability properties as density and grid voltage are varied. (a) Spectra of $I_{\text{grid,rf}}$ vs $V_{\text{grid,dc}}$ for different densities. (b) Floating potential and grid current vs $V_{\text{grid,dc}}$ for different densities. (c) Frequency scaling with plasma frequency. (d) Simultaneous single-shot traces of $I_{\text{grid,rf}}$ and V_{float} , showing that a positive potential jump coincides with the loss of oscillations. Both effects are only observed inside the bubble.	28
31	Probe I-V curve inside a plasma bubble embedded in a pulsed discharge plasma. (a) Probe current vs time for different probe voltages, showing a voltage-dependent electron decay time short than the ion decay. It is caused by electron depletion by the probe which results in a negative differential conductance, $dI/dV < 0$, in the afterglow where no electrons can enter the sphere. (c) Rf waveform of the grid current for different probe voltages. Note oscillations extend into the afterglow where electrons are trapped inside the bubble. (d) Spectrum of the oscillations in the afterglow [time indicated in (c)]. The line is broad since the density decays during the FFT. The probe changes the frequency when electrons are collected.	29
32	Sheath instability in an afterglow plasma. (a) Oscillations in the grid current of a biased sphere whose frequency decays in time. (b) Frequency decay vs time, $f(t)$. Since the frequency is proportional to the plasma frequency, a plot of $\log f_p^2$ yields the density decay time <i>inside</i> the oscillating bubble. (c) The density decay of the <i>outside</i> plasma, obtained from the decaying ion grid current, is comparable to the bubble decay. Electrons are trapped in the bubble while ions flow in and out of the bubble.	30

- 33 Pulsed grid voltage to observe the emptying and filling of a plasma bubble. (a) Grid voltage $V_{\text{grid}}(t)$ and the floating potential measured with a second probe near the center of the sphere. Initially the floating potential approaches the discharge voltage, indicating trapping of primary electrons. (b) Ion saturation current to a Langmuir probe in the center of the 8 cm diam. sphere. The ions are expelled slowly because the electrons are trapped and both species must decay at the same rate. (c) Oscillation in the grid current which continue as virtual anode oscillations when the bubble is empty. (d) Time-resolved spectrum of the grid current oscillations showing a frequency rise while the density in the bubble decreases. Thus the ion plasma frequency in the bubble volume does not determine the instability frequency, but only in the vicinity of the grid. (e) Dc ion current vs grid voltage showing an empty bubble at large negative grid voltages. (f) Frequency and amplitude dependence of $I_{\text{grid,rf}}$ vs $V_{\text{grid,dc}}$ 31
- 34 Triggering sheath oscillations with a short trigger pulse applied to an electrode in the center of the sphere. (a) Oscillations in the grid current vs time for different grid voltages. For $V_{\text{grid}} < V_{\text{dis}}$ low frequency transient oscillations are excited which decay in time. For $V_{\text{grid}} > V_{\text{dis}}$ the high frequency sheath instability is excited. (b) Evolution of the high frequency instability on an expanded time scale. The frequency increases with $|V_{\text{grid}}|$ and becomes a virtual anode oscillation when electrons cannot enter into the bubble. (c) Contour plot of the oscillations in the probe ion current near the inner sheath. Three different modes of oscillations can be distinguished. . . 33
- 35 Change of bubble parameters by a pulsed emissive probe. (a) Ion saturation current of a Langmuir probe, bias voltage of an emissive probe and grid rf oscillations. The initially empty bubble is filled with ions which are neutralized by electrons from the emissive probe. The instability is quenched by a large electron supply. (b) Langmuir probe currents for different probe bias, collecting electrons from the emissive probe. (c) Probe I-V characteristic at the onset of the emissive probe pulse. The peak electron energy is close to the emissive probe voltage. (c) Langmuir probe characteristic after the end of the emissive probe pulse where the energetic electrons are lost to the probe. 34
- 36 Frequency and amplitude of the sheath instability vs electron emission current. The grid is biased so as to exclude electrons from the ambient plasma. The frequency drops when electrons reduce the space charge in the sheath. A large electron supply quenches the instability. Without electrons virtual anode oscillations remain. 36

37	Spectrum of the sheath instability $I_{\text{grid,rf}}$ vs Langmuir probe voltage V_{probe} for different emissive probe voltages, V_{emfil} . The grid bias prevents electrons from the ambient plasma to enter into the bubble. The Langmuir probe changes the amplitude and frequency of the instability because it collects electrons from the emissive probe which modifies the plasma potential and sheath properties. Interesting features are multiple modes, copious harmonics and a frequency dip when V_{probe} is close to the ambient plasma potential.	36
38	Spectrum of grid current oscillations vs dc grid voltage perturbed by Langmuir probe currents. (a) Spectrum $I_{\text{grid,rf}}$ vs $V_{\text{grid,dc}}$ when the probe draws ions which produces negligible perturbations. (b) $I_{\text{grid,rf}}$ vs $V_{\text{grid,dc}}$ when the probe draws electrons, which changes the frequency and its dependence on V_{grid} . (c) Probe I-V characteristics for different $V_{\text{grid,dc}}$. For $ V_{\text{grid}} > V_{\text{dis}}$ the electrons are supplied from the emissive probe, for $ V_{\text{grid}} < V_{\text{dis}}$ electrons from the ambient plasma also enter into the bubble. When the Langmuir probe collects electrons the plasma potential rises with increasing probe bias.	38
39	Bubble plasma parameters and instability properties for different Langmuir probe voltages and grid voltages. (a) Spectrum of $I_{\text{grid,rf}}$ vs V_{probe} for different V_{grid} and fixed $V_{\text{emfil}} = -50$ V and $V_{\text{dis}} = -35$ V. When $ V_{\text{grid}} > V_{\text{dis}}$ the electrons in the bubble are supplied by the emissive probe which excites mode A for negative probe bias and mode B for probe bias $V_{\text{probe}} > V_{\text{emfil}}$. For $ V_{\text{grid}} \leq V_{\text{dis}}$ electrons from the ambient plasma enter the sphere which reverses the frequency dependence $f(V_{\text{probe}})$. A pronounced frequency dip occurs when the probe is biased close to the ambient plasma potential. Copious harmonics arise when the electrons are neither collected by the grid ($V_{\text{grid}} \leq V_{\text{emfil}}$) or probe ($V_{\text{probe}} \leq V_{\text{emfil}}$). (b) Floating potential of the Langmuir probe vs grid voltage showing that the emissive probe prevents the formation of a virtual anode. (c) Probe electron and ion saturation currents vs V_{grid} . (d) Ratio of ion to electron current vs V_{grid} , showing a pronounced maximum when $V_{\text{grid}} \simeq V_{\text{emfil}}$ where mode B has a frequency maximum, mode A a minimum.	40
40	Grid bias variation in a 3.5 cm diam. sphere of coarse mesh. (a) Spectrum of $V_{\text{probe,rf}}$ vs V_{grid} . For $ V_{\text{grid}} < 110$ V the leaky grid has no control over the electron supply, hence $f = \text{const}$. For $ V_{\text{grid}} > 110$ V the grid restricts the electron supply which increases the frequency and suppresses harmonics. (b) Floating potential vs V_{grid} showing a sharp rise at $V_{\text{grid}} > -110$ V when the electron leakage stops.	42
41	Spectrum of $I_{\text{grid,rf}}$ in a 2 cm diam sphere of <i>fine mesh</i> grid, exhibiting a mode jump at $V_{\text{grid}} \simeq -60$ V. (b) Amplitude $I_{\text{grid,rms}}$ vs V_{grid} . The mode jump is not caused by electron leakage through the grid.	43

42	(a) Spectrum of a coarse wire sphere with mode jump and formation of multiple sidebands. (a) $I_{\text{grid,rf}}$ vs f and V_{grid} with subharmonic creation at $V_{\text{grid}} \simeq -95$ V. (b-d) Spectra of $I_{\text{grid,rf}}$ at different V_{grid} showing main instability, sidebands and subharmonics.	44
43	Schematic picture how to eliminate the phase modulation of an electromagnetic wave passing through a noisy plasma.	45
44	(a) Schematic setup for producing supersonic ion flows with shear. (a) Side view of plasma device, showing cathode and anode for producing a plasma column (in black). An insulated wire traverses the plasma and carries a pulsed current in x-direction. The unmagnetized ions flow are radially away from the wire at supersonic speeds. (b) End view of the device. The rising wire current produces an opposing inductive electric field which together with the B field around the wire causes an electron ExB drift. The ions are unmagnetized. A radial space charge electric field is created which accelerates the ions radially outward. The ion flow is supersonic and has shear due to the up-down asymmetry produced by the circular return current loop. (c) Side view in the y-z plane showing the radial ion outflow from the wire during the rise of the wire current. (d) Waveform of the wire current. Only the rise up to I_{max} is considered here.	46
45	Snapshot of the radial density profile and its fluctuations. The density is proportional to the measured electron saturation current of a small Langmuir probe at $z = 5$ cm from the wire. The peak in the density profile occurs at the front of the expanding plasma. Density fluctuations arise during the ion flow (I_{rms}). The flow depletes the density at the wire and leaves a radial density gradient.	47
46	Properties of the density fluctuations in the time and frequency domain. (a) Fluctuations in the electron saturation current ($\propto n_e$) at a fixed position ($y = 0, z = 5$ cm) for 25 repeated shots. The expansion front (first pulse) is repetitive while the waves have amplitude and phase fluctuations. (b) Average over the traces in (a), showing the repetitive part of the waves. (c) Frequency spectra of 25 repeated traces from (a). (d) Frequency spectrum of the averaged waveform which has the same center frequency but fewer high frequency components due to phase mixing by averaging.	48
47	Contours of the Fast Fourier Transform (FFT) of the density fluctuations vs radial position, $\delta I_{e,\text{sat}}(f, z, y=0)$. The center of the spectrum shifts slightly due to the radial density gradient.	49

48	Contour plot of the plasma density in the half plane to the right of the wire, located at $y = z = 0$, taken during the radial plasma expansion front whose peak is the red contour. The density before the expansion ($t' < 0$) and outside the expansion front are uniform and at rest. Between the wire and expansion front the plasma streams radially outward. In this region ion acoustic waves are created. The radial flow has an azimuthal asymmetry hence a shear, $dv_r/d\phi \neq 0$	50
49	Space-time plot of the density fluctuations. The probe electron saturation current is plotted at $z=3\text{cm}$ vs y and time t during the rise of the wire current. First large contour is the expansion front ($v_y \simeq 5 \times 10^5 \text{ cm}/\mu\text{s}$), followed by a multitude of oscillations during the sheared ion outflow. The wave propagation is not radially outward. The wave properties are obtained from two-probe cross correlations and conditional averaging of probe signals.	50
50	Five consecutive snapshots of averaged density fluctuations in the right half plane of the wire. Wave contours stream from bottom and top toward the midplane, forming almost field-aligned phase fronts, then propagating radially inward and outward. Frequency (150 kHz) and wavelength ($\lambda \simeq 2 \text{ cm}$) show that the waves propagate near the ion sound speed, $c_s \simeq 3 \times 10^5 \text{ cm}/\mu\text{s}$	51
51	Contours of the plasma density profile in the y - z plane during the time interval of wave propagation. The density profile changes slowly compared to the time scale for wave propagation.	52

1. Summary

We have observed the interaction of streaming ions with a stationary plasma with the aim of studying ion acoustic turbulence, possibly involving an instability caused by velocity shear. The ion beam source was a dc discharge in an enclosed container which could be biased positive with respect to a second dc discharge in a main plasma chamber. The bias controlled the ion beam velocity, which could be varied from sonic, $v \simeq c_s = (kT_e/m_i)^{1/2}$, to supersonic, $v \geq c_s$. In-situ probes were used to measure the local and time-varying plasma parameters, ion distribution functions, and unstable waves. The ion beam-plasma instability was observed and characterized. Density fluctuations were recorded in time and space, Fourier transformed into frequency space, and cross-correlated in space. The waves were identified as ion sound modes and little evidence of velocity shear-induced effects was found. The propagation of test waves and pulses, including their growth and decay, in the presence of the instability was studied. The dependence of the growth rate on beam energy was demonstrated. The effect of magnetizing the electrons on the level of plasma turbulence was also investigated. Finally, the interaction of density fluctuations with electromagnetic waves were investigated. Strong scattering of electromagnetic signals was observed when the wave was guided by a transmission line through a turbulent plasma. The effect was enhanced by forming a transmission line resonator and applying frequencies on the slope of the resonance curve. The scattered signal was used to diagnose the turbulence. As a result of the laboratory findings, a new approach is proposed to eliminate the modulation of a high frequency signal by plasma turbulence.

We have also studied the oscillations taking place at the sheath present in the grid forming the boundary between the ion beam source and the background plasma. By modifying the geometry of the grid, we have shown that the oscillations are caused by the self-consistent currents passing through the grid. These currents, consisting of electron and ion flows, are controlled by the electrical potentials applied to the grid as well as the behavior of sources and sinks enclosed by the grid. These findings are important because they demonstrate that the oscillations discussed above originate from the interaction between the ion beam and the background plasma and not from the beam injection boundary. In addition, the findings suggest possibly uses as plasma diagnostics as well as provide an environment where ion expansion into vacuum can be modeled.

2. Introduction

The communication blackout with space vehicles during atmospheric reentry has been a subject of interest since the dawn of space flight [1]. Research has demonstrated that this problem is due to a plasma generated via mechanical processes enveloping the rapidly moving vehicle [2]. The plasma, in accordance to general theory, acts as a barrier for rf waves emitted by, or transmitted to, antennas located in the spacecraft. Most research to date has treated the plasma sheath as a stationary plasma attached to the vehicle [3], and several approaches have been suggested to remediate blackout [1]. One such method is the use of a magnetic “window” to allow rf to cross the plasma sheath barrier [2] and some work has recently been done in this area [4, 5] with some promise of success.

Unfortunately, little attention has been paid to other plasma issues such as, for example, interaction of the sheath with the ambient plasma naturally present at the start of reentry. It is well known that there are natural plasma instabilities, such as electrostatic ion acoustic waves, present at the interface of two plasmas streaming with respect to each other [6, 7]. These instabilities can conceivably scatter the waves that may transmit through the near-vehicle plasma sheath. It is already known that incoming signals are scattered by plasmas created by space vehicles [8].

The study of turbulent diffusion layers in space plasmas is difficult due to the spacecraft motion and time variations of plasma conditions not to mention the extremely hazardous conditions for most materials. On the other hand, scaled laboratory experiments are well suited to investigate instabilities leading to plasma turbulence and scattering of electromagnetic waves. For example, Thomson scattering of electromagnetic waves from electrostatic waves is a common remote diagnostic technique in laser plasmas [9].

A related, well-diagnosed example of ion-ion streaming instabilities is the configuration of double plasma devices [10], where two plasmas are produced with a potential difference such that ions stream from a source plasma into a target plasma. Extensive studies of ion acoustic instabilities, nonlinear waves, and plasma turbulence have been performed [11, 12, 13]. However, little attention has been given to the velocity shear at the stream boundaries in double-plasma devices, although they have been investigated in strongly magnetized plasmas [14, 15, 16]. Recently, the influence of velocity shear has been examined theoretically and computationally by Sotnikov et al [17] who show that shear in the ion velocity can be significant and dominant over other wave turbulence. This report is on work designed to create an ion beam/background plasma experiment where such ideas could be tested.

The experimental group lead by Prof. Reiner L. Stenzel at UCLA has developed a unique expertise on careful plasma experimentation and submitted a proposal to conduct laboratory research on the characterization of ion acoustic turbulence in a plasma where there could be velocity shear. Ion acoustic turbulence was created by using a small diameter source plasma to inject ions into a larger diameter target plasma as well as introducing barriers to the free transit of beam ions. The turbulence was characterized, and studies on microwave scattering by the ion acoustic turbulence were undertaken.

The scope of work was expanded to include further measurement of the observed instabilities as well as explore other methods to introduce an external velocity shear region. In order to advance the research, it was noted that the observed turbulence in the ion beam could be originating at the source of the ion beam instead of due to interaction between ion acoustic waves and the observed ion beam velocity distribution. The origin of the ion beam, as described below, is at the boundary between a “double plasma” device [18] and the ambient plasma. This boundary is a transparent sheath. Such sheaths are known to oscillate [19] and it is important to know if these oscillations are not part of the spectrum associated with the ion acoustic waves under study. Research has shown that the oscillations at transparent sheaths between plasma regions arise because particle flows across these boundaries are controlled by the electrical potentials between these regions. This is a multivariate problem which has been investigated in order to understand turbulence at plasma-wall interfaces [20, 21, 22, 23].

While the initial experiments focused on ion beams with velocity shear injected into a stationary plasma the next research phase was concerned on creating bulk ion flows with shear. This has been accomplished in a large discharge plasma by accelerating the plasma with pulsed magnetic fields. The associated inductive electric field accelerates first the electrons and then the ions via space charge electric fields. Nonuniform magnetic fields create shear flows. No ion beam instabilities or sheath instabilities are involved. The shear flow produces ion acoustic turbulence. Scattering experiments were started when the funding ended. As an afterthought we proposed a method to expel plasma from the reentry vehicle. This would open up a “window” of transparency and mitigate the communication blackout [24].

3. Methods Assumptions, And Procedures

3.1 Technical Approach

The research was to be conducted in Prof. Stenzel's laboratory at UCLA. Their main facility consists of a large (1 m diam, 2.5 m length) pulsed dc discharge plasma generated with a 1 m diam oxide-coated cathode. The parameter regime ($n_e \simeq 10^{12} \text{ cm}^{-3}$, $kT_e \simeq 2 \text{ eV}$, $B_0 = 5\text{-}10 \text{ G}$, $p_n \simeq 0.4 \text{ mTorr Argon}$) is that described by electron magnetohydrodynamics.

The work reported here was conducted in a smaller device consisting of a cylindrical aluminum chamber of 38 cm diameter and 120 cm length. A schematic diagram of this experimental setup is shown in Fig. 1. In order to create the flow, we accelerated ions from a plasma source into a stationary target plasma. This technique is well established from the "double plasma" (DP) devices [18]. The source plasma was contained in a cylindrical stainless steel chamber of 20 cm diameter and 25 cm length. One end of the closed cylinder had a grid for the extraction of ions. Inside the cylinder, three tungsten filaments formed the cathode. The cylinder wall formed the anode. Insulated feedthroughs provided the power to heat the cathode (15 V, 20 A) and the discharge current (50 V, 0.3 A). Typical parameters for both source and target plasmas were: density of $n_e \simeq 10^9 \text{ cm}^{-3}$, electron temperature $kT_e \simeq 2 \text{ eV}$ in Argon at a pressure of $p_n \simeq 10^{-4} \text{ Torr}$.

The source plasma was placed inside the chamber, separated by ceramic standoff insulators. The outer cage also had a grid on one end through which the ions can flow. The outer cylinder was also insulated from ground, which refers to the wall of the larger chamber containing the target plasma. The source plasma was inserted coaxially into the target chamber as shown in Fig. 2(a). The outer source cylinder was biased negatively so as to reflect the electrons from the target plasma. This was important to establish a

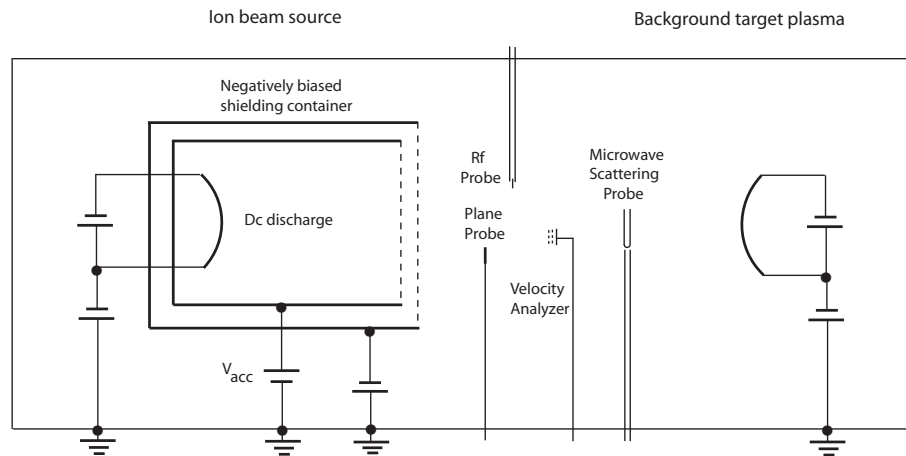


Figure 1. Schematic of the Experimental Setup for Injecting an Ion Beam into a Background Plasma

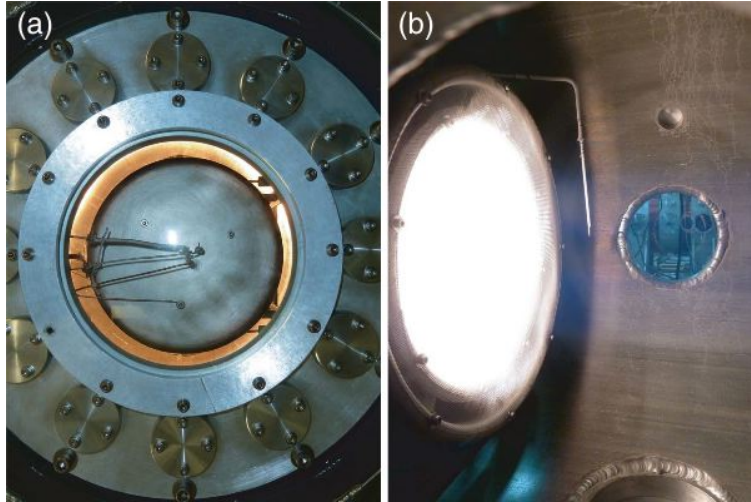


Figure 2. (a) Photograph of the source container (inner cylinder, end view) inside the larger target plasma device (outer container with many flanges) (b) Side view of the ion beam source inside the larger target plasma device. The bright light is due to the incandescent tungsten cathode filaments. A probe is in front of the beam source

potential difference between the source and target plasma. The target plasma potential was usually close to ground. When the source plasma potential was positive, the ions from the source did stream into the target plasma. The ion beam velocity could be readily varied from zero up to Mach 10.

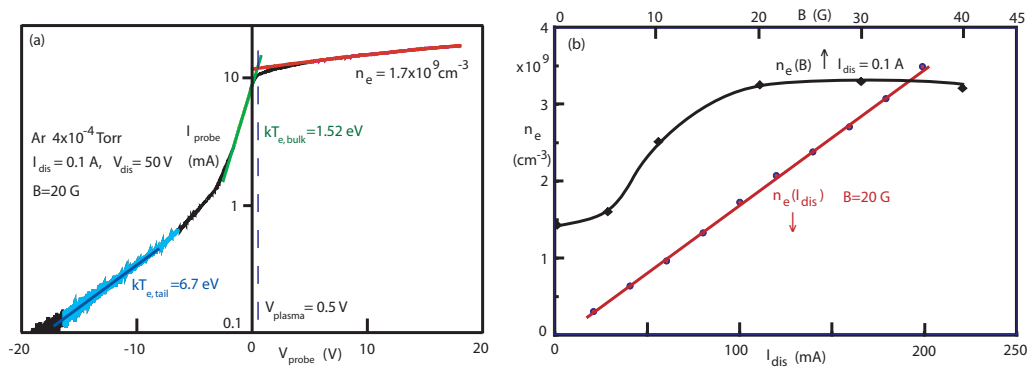


Figure 3. Basic plasma diagnostic and results. (a) Langmuir probe I-V characteristics with evaluation of electron temperature, density and plasma potential. (b) Dependence of density on discharge current and axial magnetic field.

3.2 Plasma Diagnostics

The plasma parameters were diagnosed with a plane, one-sided Langmuir probe (1×1 cm). The current-voltage (I-V) characteristics was displayed in real time using a voltage ramp generator ($-20... + 30$ V) and a digital oscilloscope. The probe traces were evaluated as explained in Fig. 3(a). The logarithmic plot of current vs voltage shows two regions with linear slopes, corresponding to energetic tail electrons (6.7 eV) and colder bulk electrons (1.5 eV). The former were due to scattered primary electrons from the cathode (-50 V), the latter were the colder secondary electrons produced by ionization. The “knee” in the I-V characteristics, defined by the intersection of linear fits to the retardation and saturation regimes, was near ground potential. Given the probe size and the electron temperature, the saturation current yielded the indicated electron density.

Figure 3(b) shows that the electron density varied linearly with discharge current. The density also had a linear dependence with the neutral gas pressure (not shown). When a weak axial magnetic field was applied, the primary electrons were radially confined which enhances the ionization probability and electron density as shown. Such weak magnetic fields, however, did not confine ions.

3.3 Generation of Ion Beams

The injection of an ion beam was accomplished by bringing two plasmas with different plasma potentials in contact and providing a negative potential well at the interface. The latter was accomplished with a negatively biased grid and served to prevent electrons to pass from one plasma to the other which would have created large currents and short circuited the plasma potential difference.

In order to verify the presence of an ion beam in the target plasma one could use an energy analyzer or a plane Langmuir probe. For simplicity, the latter was used in the early stage of the experiment. The principle of detecting an ion beam in the I-V characteristics of a probe is as follows: When the probe is biased positive with respect to the plasma potential, it is surrounded by an electron-rich sheath. The ion beam is reflected when the probe bias exceeds the ion beam energy. The stagnation and reflection of ions inside the sheath reduces the space charge density which expands the sheath thickness. The surface area for electron collection increases which raises the probe current. The I-V characteristics now exhibits two “knees”, one at the plasma potential, $V_{\text{probe}} = V_{\text{plasma}}$, and a second one at the beam potential, $eV_{\text{probe}} = m_i v_{\text{ion}}^2 / 2$. The two knees are more easily visible in the derivative of the probe trace, $dI_{\text{probe}}/dV_{\text{probe}}$. This effect has been studied and established earlier [25].

We inserted a plane Langmuir probe near the center of the beam injection region and verified the presence of the ion beam. Figure 4 shows the IV characteristic of the the probe and its derivative which exhibits a peak at the plasma potential and another at the ion beam energy. By varying the bias of the inner discharge container, the source plasma potential, hence ion beam energy, was varied.

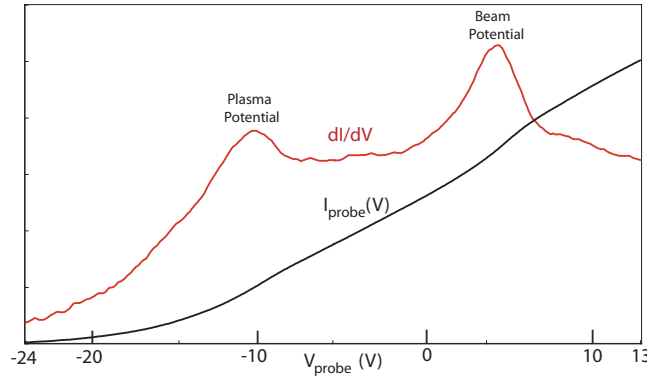


Figure 4. Identification of an ion beam from the current-voltage characteristics and its derivative of a plane Langmuir probe.

The ion distribution function was obtained from a plane retarding-grid velocity analyzer. It consisted of two fine-mesh grids (100 lines/inch) and a collector (1 cm²). The first grid repelled electrons, the second discriminated the ions by their energy and the collector collected the ion flux. The derivative of the $I_{\text{ion}} - V_{\text{grid}}$ characteristics yielded the ion distribution function. As with the Langmuir probe, it exhibits one peak at the plasma potential due to the target ions and a second peak due to the ion beam from the source plasma. The beam energy is given by the potential difference between the peaks. The ratio of the ion beam flux and the background ion flux yields the normalized beam density. The velocity analyzer was also radially and axially movable.

Figure 5(a) displays a set of ion velocity analyzer traces for different acceleration voltages on the source plasma chamber. The ion current to the collector exhibits, as expected, two steps with grid voltage, one when beam ions are collected, another one when background ions are collected near the plasma potential ($V_{\text{grid}} \simeq 0$). The ion beam flux is comparable to the background ion flux. The ion beam flux does not change significantly with beam velocity since the Bohm current from the source is constant. It is shown below that the ion-ion beam instability had an optimum beam velocity and vanished for both slow and fast beams.

Figure 5(b) shows the ion distribution function, obtained from a derivative of I_{ion} vs V_{grid} . The traces were smoothed because noise was introduced by the digital differentiation process. Except for low energies (< 3 eV), the beam distribution was distinct from the background ion population. At the injection point the beam was cold.

3.4 Wave Diagnostics

Density fluctuations and waves were detected with two rf probes. These consist of 50 Ohm semirigid coaxial cables whose center conductor protrudes about 0.5 cm from the end of the cable. Special high temperature coax was required since the probes pass close to the incandescent cathode filaments. The insulating material is ceramic powder. The probes could be moved axially and radially to study wave propagation and

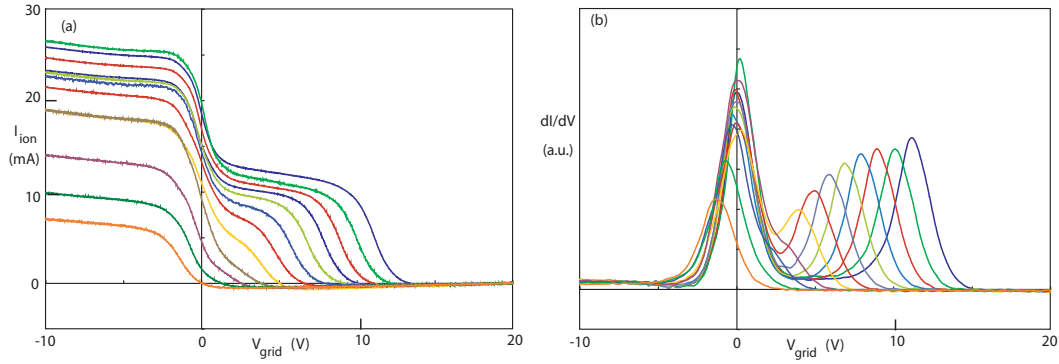


Figure 5. (a) Ion velocity analyzer traces for different beam energies and (b) ion energy distributions obtained from the derivative of the above I-V curves.

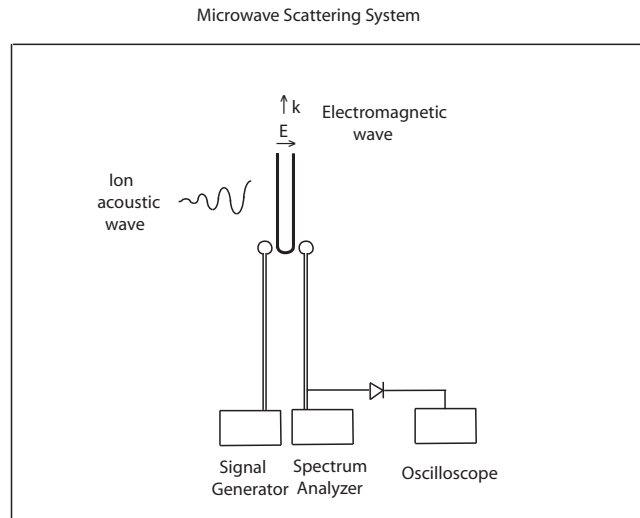


Figure 6. Schematic picture of the microwave resonator probe for studying the scattering of electromagnetic waves by density fluctuations.

cross-correlation of density turbulence.

In order to study the scattering of electromagnetic signals by density fluctuations, a special diagnostic probe shown in Fig. 6 was used. Ideal wave scattering theory applies to plane waves which satisfy frequency and wavenumber matching ($\omega_1 + \omega_2 = \omega_3, \mathbf{k}_1 + \mathbf{k}_2 = \mathbf{k}_3$), arising from energy and momentum conservation. These conditions are not satisfied in a bounded plasma layer around a conducting rocket body. Likewise, plane waves were scattered by the conducting chamber wall in a bounded laboratory plasma and established a complicated interference pattern. Since the typical wavelength of the ion wave turbulence was on the order of 1 cm, coherent scattering experiments would typically require 30 GHz microwaves. Such equipment was not available and is out of the range of the present contract budget.

A new approach was been chosen for this reason. The dominant wavenumber of the electromagnetic wave on a parallel-wire transmission line is given by the transverse wire spacing, not the wavelength along the line. It can be easily adapted to the wavelength of ion acoustic waves. When the latter propagate transverse to the transmission line, the electromagnetic wave is “scattered” or phase modulated. In order to obtain spatial resolution along the line, the shortest dimension is that of a quarter wavelength standing wave. At microwave frequencies, a quarter-wavelength resonator is only a few cm long. Its resonance frequency depends on the plasma dielectric function, $\epsilon_{rel} = 1 - [\omega_p/\omega]^2$, i.e., on the electron density, which has earlier and elsewhere been used for density diagnostics [26, 27, 28].

Once the resonance curve is characterized for a given base electron density, then any density fluctuations cause shifts in the frequency peak of the resonance curve. This can be translated into an amplitude fluctuation by tuning the detector’s frequency to either slope of the resonance curve. Under these conditions, the collected electromagnetic signal showed large amplitude fluctuations under the influence of the ion acoustic instability. This is shown below and demonstrates that the microwave signal could be used to measure the properties of the density fluctuations.

3.5 Oscillating Sheath Production

A low temperature plasma is produced by a dc discharge in a vacuum chamber of 45 cm diam. and 150 cm length shown schematically in Fig. 7(a). The typical parameters are an electron density $n_e \simeq 10^9 \text{ cm}^{-3}$, electron temperature $kT_e \simeq 2 \text{ eV}$, Argon pressure $p \simeq 5 \times 10^{-4} \text{ mTorr}$ and a uniform axial magnetic field $0 < B_0 < 20 \text{ G}$. Gridded spheres, shown in Fig. 7(b, insert), are inserted into the center of the plasma. The 2.5 cm diam sphere is made of a single sheet of fine grid (mesh size 0.25 mm, 80 % transparent). The 3.5 cm diam sphere is made of a coarser grid (mesh size 1 mm, wire diameter 0.2 mm) which was formed by spot welding two hemispheres together. A 2 mm hole allowed the insertion of a ceramic shaft containing a cylindrical Langmuir probe (0.13 mm diam, 3mm length). Care was taken to avoid any other openings through which electrons could enter the cavity. A larger cavity of rectangular shape has also been used ($10 \times 10 \times 2 \text{ cm}$). It allows to bias different portions of the grid surface separately so as to investigate gradients in the ambient electron flux.

The grid is biased negatively which attracts ions into the sheath at the Bohm flux. If the plasma potential of the bubble is not above that of the ambient plasma most ions enter into the cavity. Neutralizing electrons are also supplied from the ambient plasma provided their energy $mv_{perp}^2/2 > e|V_{grid}|$ and the grid forms an equipotential surface at V_{grid} . When the grid rejects all electrons the ions build up a large space charge layer (virtual anode) which reflects them back into the ambient plasma and the bubble is empty. Plasma and grid voltage can be pulsed.

Figure 8(a) shows a schematic of the typical pulsing circuit and bubble diagnostics. The plasma parameters are measured with a radially movable Langmuir probe. An emissive probe in the center of the bubble is used to measure the approximate plasma potential and

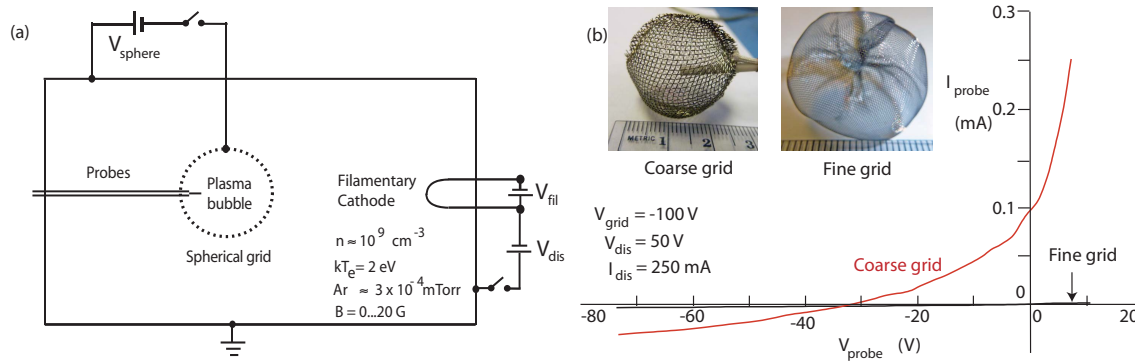


Figure 7. (a) Schematic diagram of the plasma bubble experiments with typical plasma parameters. (b) Photographs of two spherical grids with different mesh sizes which exhibit different probe I-V characteristics. The coarse mesh leaks electrons even when the bias should reflect all energetic electrons.

to inject electrons into the bubble to neutralize the ion space charge. The probe diagnostics requires careful interpretation since the probe currents can modify the plasma properties, as will be shown below. Even the ceramic probe shaft presents a perturbation since it causes surface recombination of confined charged particles.

The grid voltage is pulsed with the switching circuit shown in Fig. 8(a). In order to minimize capacitances to ground, the power supply consists of a charged, floating capacitor ($4000 \mu\text{F}$, 250 V). The switching circuit consist of a simple transistor switch. The grid current is obtained from the voltage drop of a series resistor to ground. Grid current oscillations are measured with an rf broadband transformer ($100 \text{ kHz} \dots 100 \text{ MHz}$) inserted close to the grid feed which minimizes stray capacitive currents.

The same switching circuit has also been used to pulse the ambient discharge plasma. Likewise pulsed voltages have been applied to the Langmuir probe and the emissive probe. The emissive probe requires a heater power supply which has a large capacitance to ground. In order to prevent capacitive currents, the emissive probe (0.125 mm diam, 5 mm length W wire) is heated with a floating battery (3 V , 2 A). For measuring floating potentials a 10:1 oscilloscope probe (20 pF , $10 \text{ M}\Omega$) is used or a capacitive divider with a low voltage high impedance ($10^{15} \Omega$) op amp.

The mechanism of harmonic generation of the sheath oscillations has been investigated by perturbing individual spectral lines. As shown in Fig. 8(b) a parallel L-C resonance circuit has been inserted into the line feeding the grid. When tuned to the frequency of the instability, the high impedance ($Z \simeq 10 \text{ k}\Omega$) highly suppresses the rf grid current. If the harmonics were produced by nonlinear effects of the fundamental grid current, its suppression should eliminate all higher harmonics. Surprisingly, any of the lines of the instability spectrum, shown in Fig. 8(c) can be eliminated without influence on the others. Even the fundamental line can be eliminated and the harmonics continue to oscillate. Thus, each line is an eigenmode of the sheath rather than a nonlinear product of the

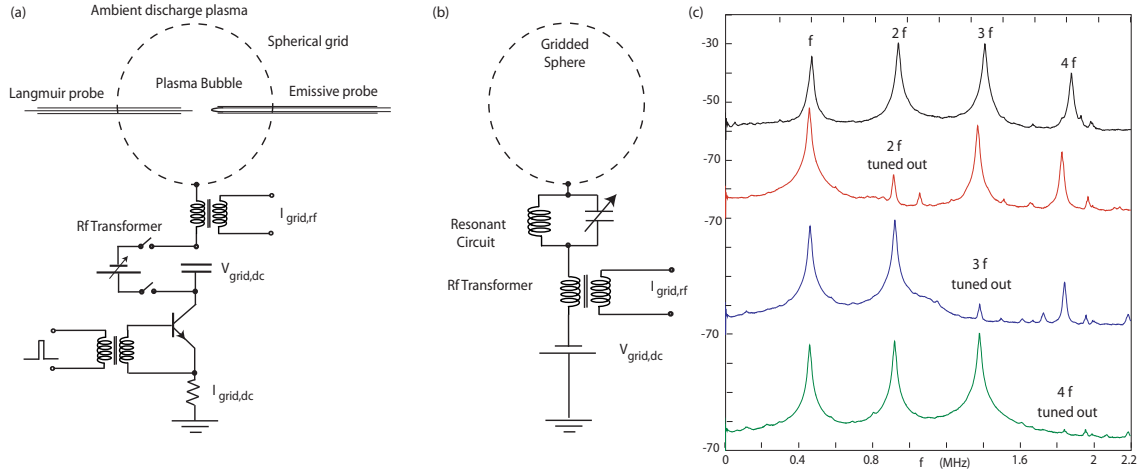


Figure 8. (a) Schematic setup to produce and diagnose pulsed plasma bubbles in an ambient discharge plasma. (b) Schematic diagram of tuning a parallel $L - C$ resonance circuit to harmonic lines of the sheath instability. (c) Logarithmic plot of the spectrum of $I_{grid,rf}$ with multiple harmonics. Top line is the full spectrum without circuit. Below are spectra where the high impedance circuit tunes out lines of successively higher harmonics without affecting the other lines.

fundamental mode. This is consistent with observations in pulsed experiments where the instability can start at the second harmonic and later excite the fundamental mode. Furthermore, Fig. 8(c) shows that the harmonics can be larger than the fundamental mode which also excludes harmonic generation by nonlinearity of the fundamental.

4. Results And Discussion

4.1 Evidence of Ion Beam Plasma Instabilities

Fluctuations were observed in the electron saturation current of the Langmuir probe. The probe was located in the center of the ion beam about 5 cm beyond the injection plane. It was biased at a fixed potential (+24 V). The ac probe current was Fast Fourier transformed (FFT) by the digital oscilloscope. Figure 9 displays the magnitude of the FFT for different beam velocities.

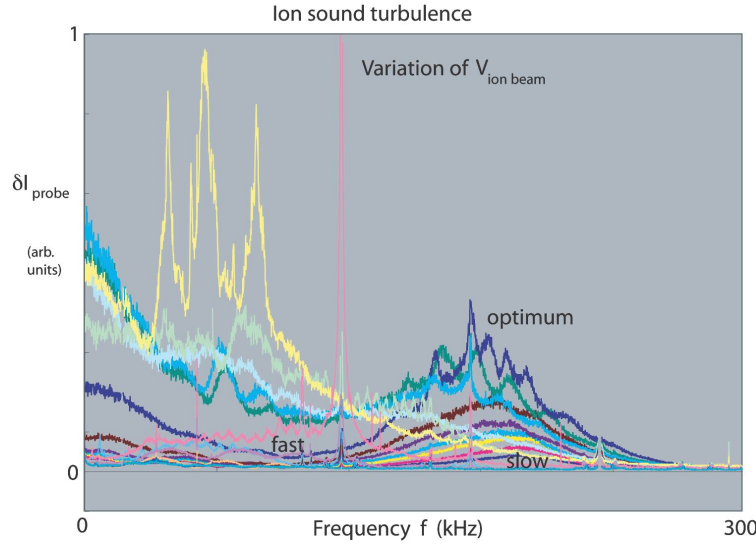


Figure 9. Fluctuation spectrum of the probe current in the presence of ion beams with different velocities. The fluctuations lie in the ion acoustic branch and were created by the ion beam. The spectrum and intensity of ion sound turbulence depended on beam velocity: for very slow beams the noise was negligible. The amplitude was largest for beam velocities of a few times the sound speed. The fluctuations decrease again for very fast beams.

The fluctuations for very slow beams were negligibly small. Some sharp spectral lines were due to external rf sources which was readily verified since their frequencies did not depend on plasma parameters. As the beam velocity was raised, a band of noise in the middle of the ion acoustic branch grew. The ion plasma frequency in the present parameter regime was $f_{p,i} \simeq 1$ MHz. For beam velocities of Mach 3 to 5, the noise maximized and shifted to lower frequencies. Pronounced lines in the low frequency sound spectrum developed. Further increase in beam velocity *decreased* the fluctuation level.

4.2 Velocity Shear Influence

Having established the existence of the instability, we then explored the influence of spatial gradients in the beam velocity on the instability. A natural location is the edge of the beam, as we originally proposed, but the gradient in that region likely is likely gentle.

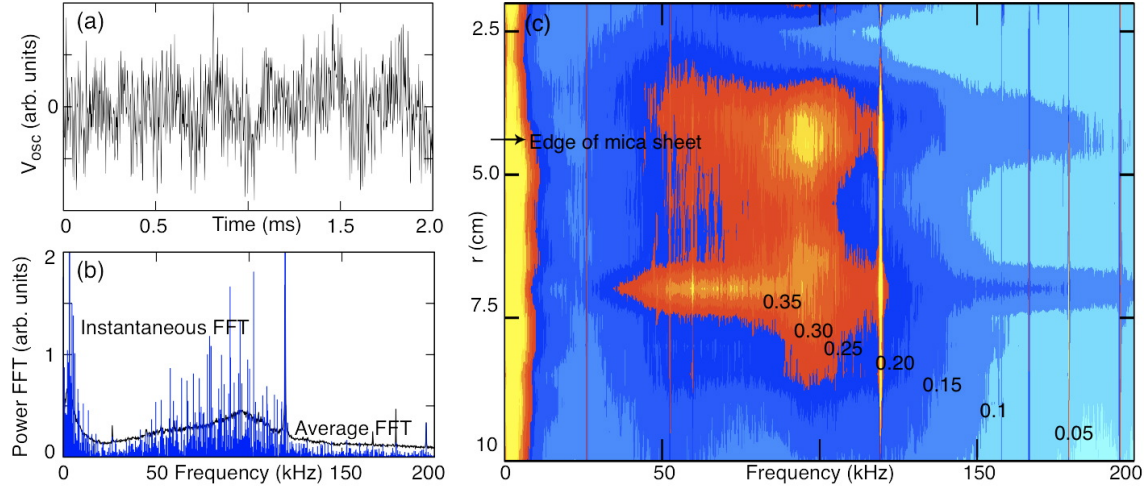


Figure 10. (a) Instantaneous fluctuation at edge of mica sheet (extending from $r = 0$ to $r = 4.6$ cm) blocking the ion beam, (b) its power spectrum (blue), together with the average power spectrum over many single observations (black), and (c) spatial variation of average power spectrum as the probe is swept radially away from behind the obstruction to the edge of the ion beam column at $r = 10$ cm.

Thus, we elected to also install an insulating mica sheet adjacent to the ion beam launching assembly and thereby obstruct it. We believed that this could create a much sharper boundary and, together with the beam's edge region, provide a reasonable comparison.

The results of this experiment are summarized in Fig. 10. Figure 10a displays a typical unstable waveform. By inspection, it's spectrum is clearly not monochromatic. Obtaining its spectrum (Fig. 10b, blue) by performing an FFT on the waveform clearly shows that the instability consists mainly of waves whose frequency is concentrated around the ion sound range, as previously shown in Fig. 9. This range is better displayed by obtaining an ensemble average of the spectra, as shown by the black line in Fig. 10b, and then sweeping the receiver probe across the beam column. The result is displayed in Fig. 10c, where the two regions of interest are observed. First, the edge of the beam at $r = 10$ cm does not present an increase in the turbulence power spectra. There is a region of enhancement, but this is fairly inside the beam column at $r \simeq 7.5$ cm. The enhancement disappears if the accelerator voltage is decreased (not shown) indicating that there must be an optimum value for n_{beam}/n_{plasma} . The enhancement, however, is not as dramatic as predicted by Sotnikov et al [17]. The instability is also observed to be enhanced around the neighborhood of the obstruction's edge ($r \simeq 4.5$ cm). This effect persists as the accelerating voltage is lowered, but the enhancement, while visible, is not as great as theoretically predicted.

Given the limited scope of the work, we elected to continue to characterize the optimum conditions leading to the instability and leave the physical details of the apparent enhancement to future work.

4.3 Ion Beam Properties

With increasing distance from the source, the ions underwent scattering by neutral collisions and by turbulence created by the beam. Figure 11 shows the measured change of ion distribution with distance from the injection point. The beam simply broadened and decayed. This has repercussions on the ion beam instability to be shown next.

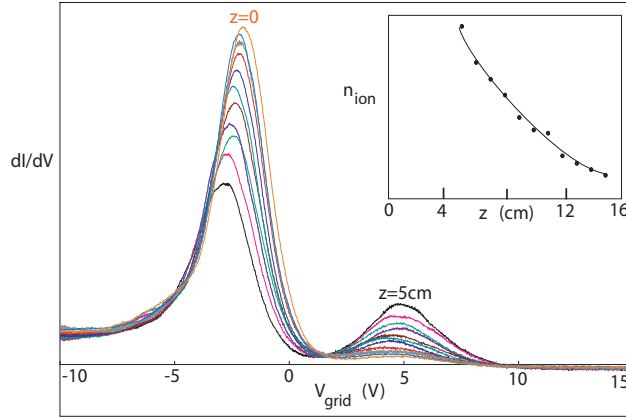


Figure 11. Ion distribution function at different axial distances z from the beam source. The traces were taken in 0.5 cm increments. The insert shows the ion beam density decay. The beam decay was partly due to scattering from ion sound turbulence and partly due to ion charge exchange collisions.

4.4 Propagation of Test Waves and Pulses

The beam velocity became modulated when an ac signal was superimposed on the dc accelerator voltage (V_{acc} , see Fig. 1). Since the ion flux was conserved, the velocity modulation implies a density modulation which can be detected by rf probes in the target chamber. By employing a typical interferometry setup [29] with the ac signal acting as the local oscillator (LO) signal and the rf probe supplying the transmitted signal (RF), a waveform of the phase of the modulation was obtained. Figure 12 shows a test wave excitation with a monochromatic beam modulation ($f = 122$ kHz). The distances z in this figure refer to the separation between the rf probe and the grid separating the target plasma from the beam source plasma. In the explored region, the wave propagated at the beam velocity ($\simeq 4$ eV), hence appeared to be a supersonic ballistic space charge mode of the beam.

A second method of beam modulation is to apply a wide frequency spectrum. This was achieved by applying a $10 \mu\text{s}$ pulse to the beam voltage instead of an oscillation at a fixed frequency. Rather than use interferometry, it was more informative to observe the entire density perturbation as shown in Figure 13(a). As the distance was increased, the perturbation grew and clearly propagated away from the region of beam injection. Figure 13(b) shows that its velocity ($v \simeq c_s \simeq 2 \times 10^5$ cm/s) was lower than the one

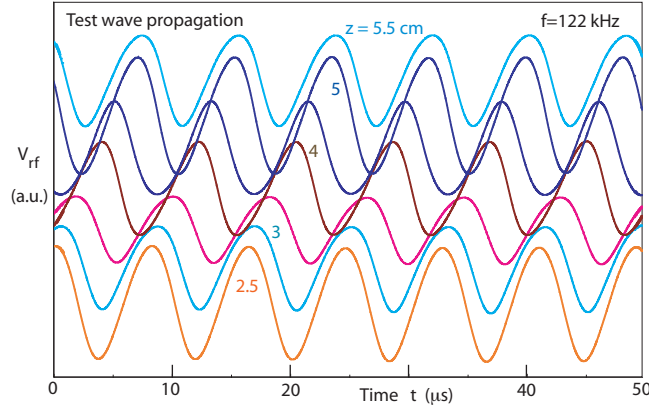


Figure 12. Propagation of a test wave excited by a modulation of the beam velocity. Waveforms detected in 0.5 cm axial increments showing a continuous propagation delay. The propagation speed ($v = f \times \lambda \simeq 3.6 \times 10^5$ cm/s) was supersonic and close to the beam velocity, hence the wave is a fast beam mode.

obtained from a time-of-flight diagram obtained with a monochromatic modulation [see caption, Fig. 12]. This figure also shows that the amplitude grew with distance, which is a property of sound wave convective instabilities. This growth, however, depended on the beam maintaining its integrity and, as observed, the wave amplitude decayed in the region where the beam was scattered, as mentioned above.

The beam modulation generated larger density perturbations than an instability which grows self-consistently out of the noise. Figure 14(a) displays both the dc and ac probe current vs time for different pulsed modulation voltages at the location of peak growth

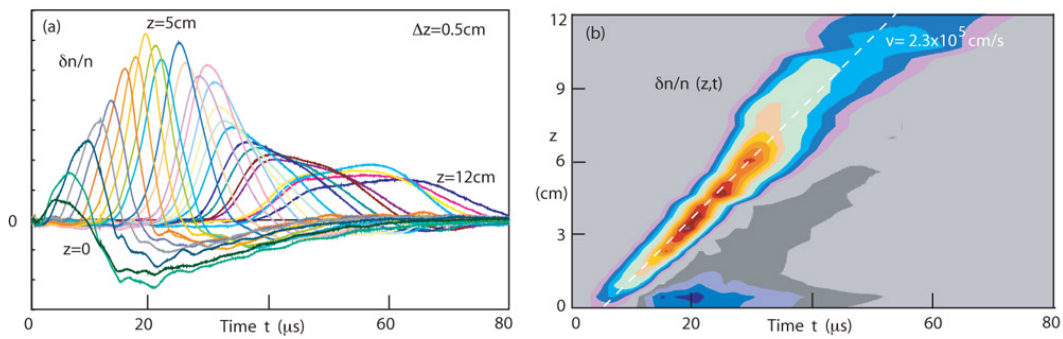


Figure 13. Propagation of a density pulse created by modulating the beam velocity with a 10 μ s pulse. (a) Waveforms of the density perturbation in the target plasma at different axial distances from the beam injection point. The density perturbation grew initially, which indicates a convective instability. The perturbation decayed when the beam was scattered. (b) Time-of-flight diagram showing the propagation velocity was close to the sound speed, $v \simeq 2 \times 10^5$ cm/s.

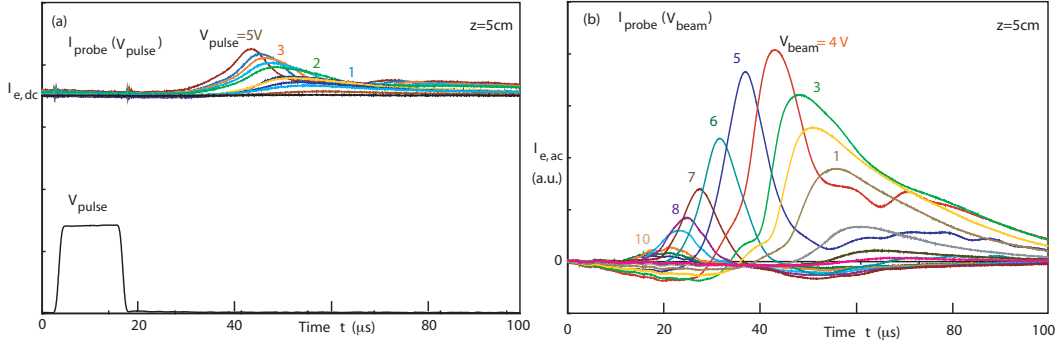


Figure 14. Dependence of pulse amplitude on different parameters. (a) Density perturbation as a function of pulse amplitude, which modulated the beam velocity. For strong modulations the normalized density perturbation $\delta n/n \propto \delta I_e / \langle I_e \rangle$ could reach 30%. (b) Density perturbation at a fixed position ($z = 5$ cm) for different ion beam velocities, showing an optimum growth when the beam velocity was slightly faster than the sound speed.

found by inspection of Fig. 13(b). At this location ($z \simeq 5$ cm), the normalized density perturbation, $\delta I_e / I_{e,dc} \propto \delta n/n$ could readily reach 30%, which is a highly nonlinear sound wave. However, this large amplitude was only obtained for an optimum beam velocity, as shown in Fig 14(b). At this fixed position and modulation level ($V_{pulse} = 5$ V), the figure shows the density perturbation peaked for a beam energy of $eV_{beam} \simeq 4$ eV. It is worth noting that the beam energy was not given by the modulation voltage, V_{pulse} , added to the bias voltage, V_{acc} . Rather, it was obtained from the difference in potential between the beam and the plasma potentials, as indicated in Figure 5(b). These observations indicate that neither high nor low velocity ion beams produced much growth.

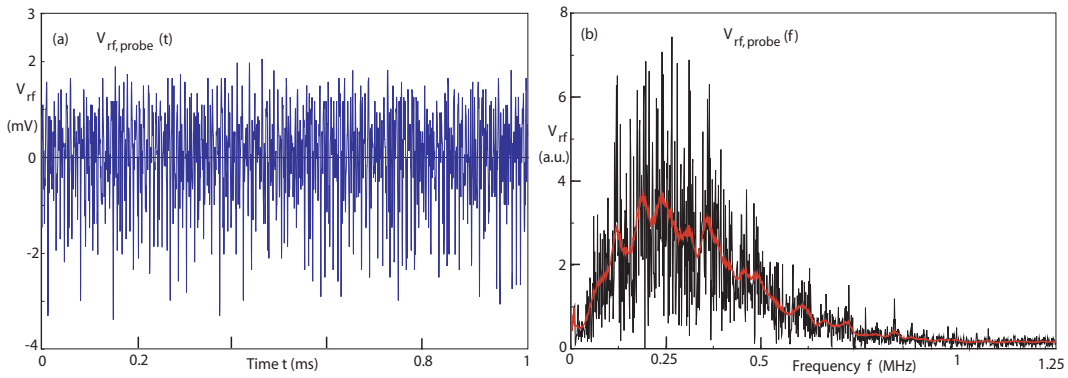


Figure 15. Noise waveform (a) and spectrum (b) of the ion-beam plasma instability ($V_{beam} \simeq 4$ eV, $f_{p,i} \simeq 1$ MHz). A smoothed (red) line was been added to the spectrum.

4.5 Ion Beam-Plasma Instability

The injection of an ion beam into the background plasma created turbulence. A typical waveform of the fluctuations in the electron saturation current of an rf probe is shown in Fig. 15(a). It consisted of broadband noise below the ion plasma frequency ($f_{p,i} \simeq 1$ MHz). The normalized fluctuation level for this unmodulated beam was relatively small, $\delta I_e / I_{e,dc} \propto \delta n / n \simeq 3\%$. The waveform was Fast-Fourier transformed (FFT) and is displayed in Fig. 15(b). The spectrum has a broad peak in the low frequency regime of the ion acoustic branch. Since no other eigenmodes exist in this frequency regime, the noise can be considered to consist of ion acoustic waves. For a sound speed of $c_s = (kT_e/m_i)^{1/2} \simeq 1.9 \times 10^5$ cm/s, the wavelength for the most unstable mode ($f \simeq 250$ kHz) was $\lambda = 0.76$ cm.

Cross-correlation measurements using two identical rf probes were performed, i.e., the product of the two probe voltages was ensemble-averaged, $\langle V_1 V_2 \rangle$. Figure 16 shows the cross-correlation functions vs time for different axial probe separations Δz . The correlation shows a dominant peak which dies out within a few cm while shifting in time along the beam. The average axial propagation speed was supersonic, $\Delta z / \Delta t \simeq 5 \times 10^5$ cm/s, but this may only be one component of obliquely propagating sound waves which was in resonance with the ion beam. Two-dimensional cross-correlation measurements could resolve the propagation direction, if desired.

The variation of the spectrum with distance along the beam was also mapped. As shown in Fig. 17(a), the most dramatic feature was the initial amplitude growth along the beam and the subsequent decay. With increasing distance, the spectral peak [Fig. 17(b)] shifted to lower frequencies, that is, longer wavelengths, which have a longer decay length. Waves and beam particles were strongly coupled since large wave amplitudes scattered the beam ions, which in turn decreased the wave growth rate.

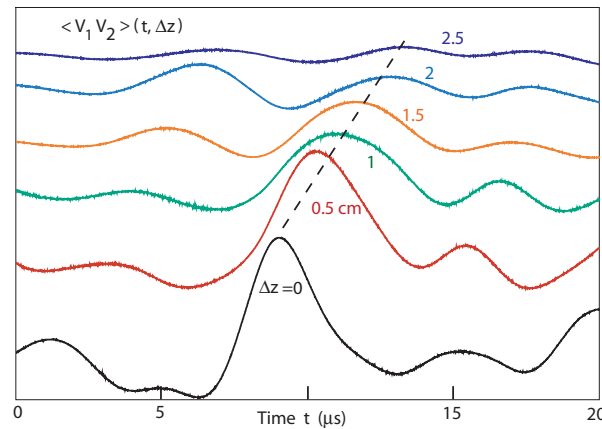


Figure 16. Cross correlation functions vs time at different axial probe separations. The peak shifted in time indicating propagation along the beam at a velocity $\Delta z / \Delta t \simeq 5 \times 10^5$ cm/s.

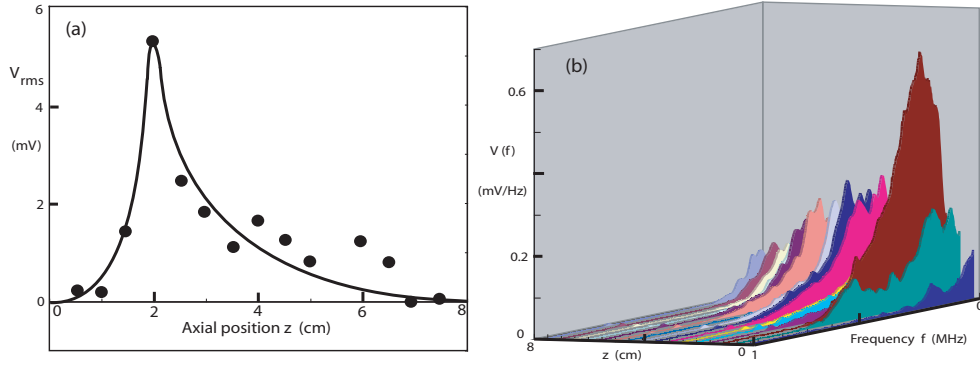


Figure 17. Growth and decay of the fluctuation amplitude (a) and spectrum (b) vs axial position.

As expected from the test wave experiments, the noise amplitude also strongly depended on ion beam energy. In Fig. 18, the probe position was fixed at $z = 5$ cm and the beam energy was varied via the acceleration voltage on the source plasma. Simultaneous measurements of ion distribution functions and wave spectra were made and are displayed as line and surface plots. The ion distributions [Figs. 18(a,b)] show beams with energies in the range $eV_{\text{beam}} = 0 \dots 10$ eV. However, the spectra [Figs. 18(c,d)] show two pronounced

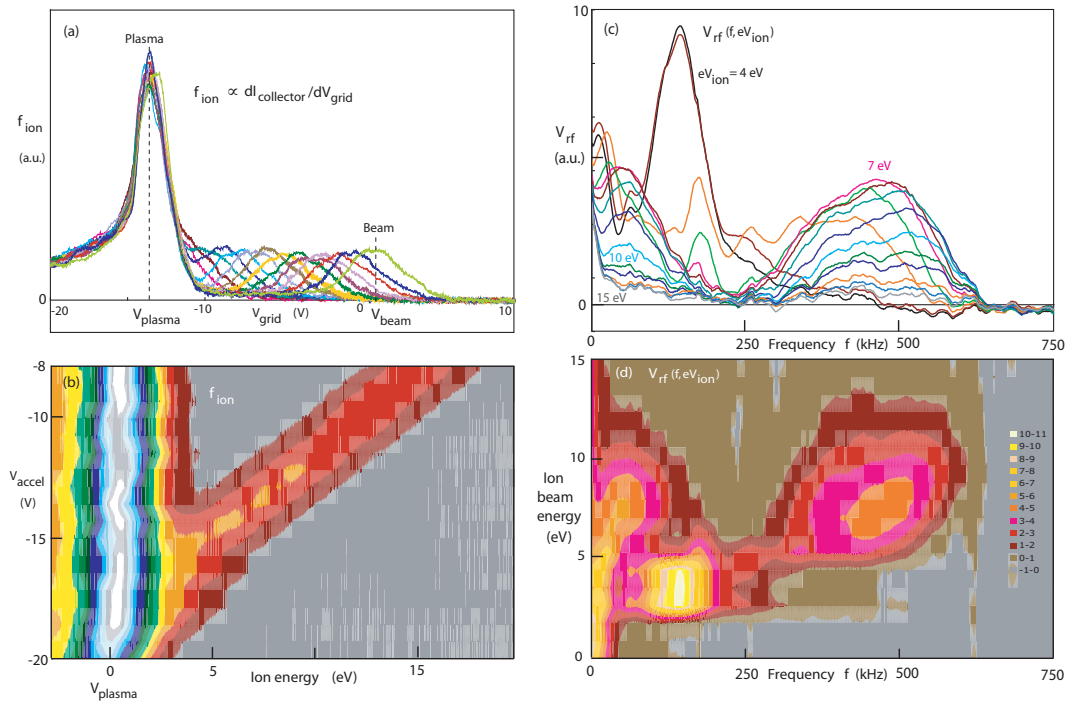


Figure 18. Ion distribution functions (a,b) and noise spectra (c,d) for different beam energies.

features: a large peak at $f \simeq 150$ kHz and a broad lower peak near $f \simeq 450$ kHz. The peaks occurred at different beam velocities. Higher frequencies were excited by faster beams, lower and larger modes by slower beams. However, no significant noise was produced for $eV_{\text{beam}} < 2$ eV or $eV_{\text{beam}} > 15$ eV. The spectral features were not due to boundary effects since the waves died out before reaching the chamber walls. Investigations focused on the generation of the instability are required in order to understand these spectral features.

4.6 Pulsed Plasma Sources

The instability also depended on plasma and beam densities. The plasma density in the target chamber was pulsed so as to observe the instability during the build-up and decay of the background density. The source density and accelerating voltage, that is, ion beam density, remained constant.

Figure 19(a) shows a set of traces of the electron saturation current of a 1 cm^2 Langmuir probe, biased in the electron saturation region. As is natural, the probe current, proportional to the plasma density, grew during the discharge pulse and decayed in the afterglow. The peak discharge current depended on the number of primary electrons, which in turn was controlled via the filament temperature. As observed, the discharge assumed steady-state within $\simeq 0.5$ ms and decayed on a time scale of $\simeq 0.3$ ms.

Simultaneously, the instability was monitored by measuring the density fluctuations on the rf probe. As displayed in Fig. 19(b), the fluctuations had an optimum beam/target plasma density range as they vanished for both high and very low densities. For large discharge currents, the noise existed only while the density was rising and late in the afterglow where the density became small. At low discharge currents (75 mA), the optimum background density, where the largest noise amplitude was observed, lasted throughout

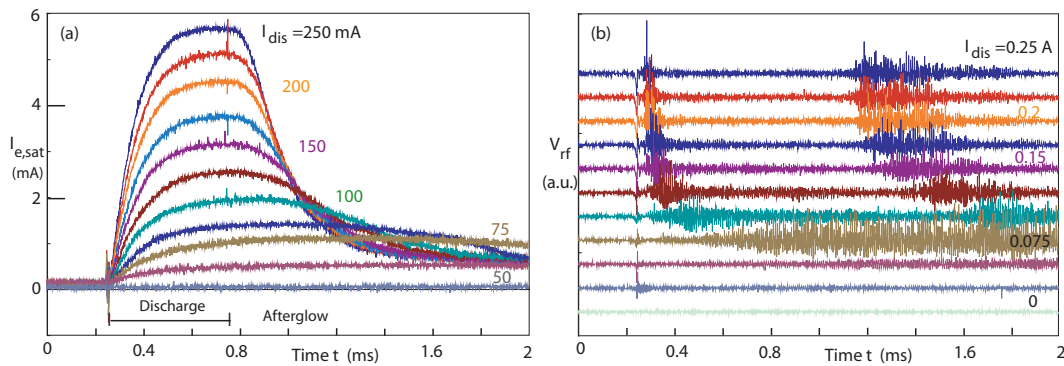


Figure 19. Ion beam-plasma instability in a pulsed target plasma. (a) Electron saturation current of a plane Langmuir probe showing density rise and fall for different peak discharge currents. (b) Density fluctuations on an rf probe showing large amplitudes in the early discharge and in the afterglow where the ratio of ion beam density to background ion density is large.

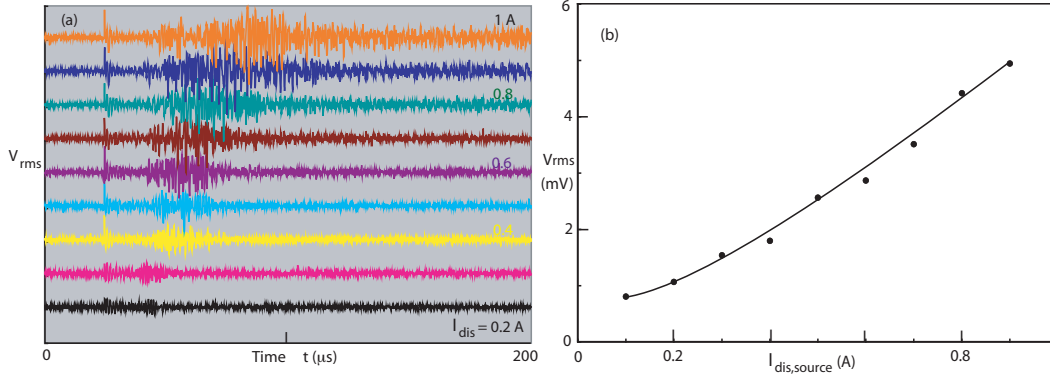


Figure 20. Ion beam-plasma instability in a pulsed target plasma for different steady-state source plasma densities. (a) Density fluctuations during the rise of the target discharge for different ion beam densities, controlled by the source discharge current. (b) Rise of plasma turbulence on ion beam density.

the discharge pulse and into the afterglow.

As the background density was lowered, the normalized beam density n_{beam}/n_{plasma} increased which produced a stronger growth rate and larger fluctuation amplitude. The same effect can be observed when the source density was varied. In Fig. 20, the discharge current in the source plasma was varied while that in the target plasma was kept constant, although still pulsed. Figure 20(a) displays the density fluctuations at the onset of the target discharge pulse. These steadily grew as the ion beam density increases. This can readily be noted when the rms value of the fluctuations is plotted vs discharge current and displayed as in Fig. 20(b).

4.7 Microwave Scattering

We measured the effects of density fluctuations on the propagation of electromagnetic waves. The most sensitive method was to match the scale length of the electromagnetic wave to that of the ion acoustic waves. As discussed in Subsection 3.4, this was accomplished by guiding the electromagnetic wave along a parallel wire line with spacing comparable to the sound wavelength. The phase velocity of the electromagnetic (e-m) wave depends on plasma density, hence the e-m wave was phase modulated. The axial length of the line was chosen to be a quarter e-m wavelength which formed a resonant structure when one end of the line was shorted, as schematically shown in Fig. 6. The resonance frequency was upshifted by the dielectric constant, i.e., plasma density, as shown in Fig. 21(a) where the rectified output of the probe is displayed as the applied signal was swept in plasmas with slightly different densities. Thus, if the density increases, the rectified output would decrease because the resonance curve has shifted to higher frequency and viceversa. Hence, if the e-m frequency produced by the signal generator is kept constant and chosen to lie on the slope of the resonance curve, a density

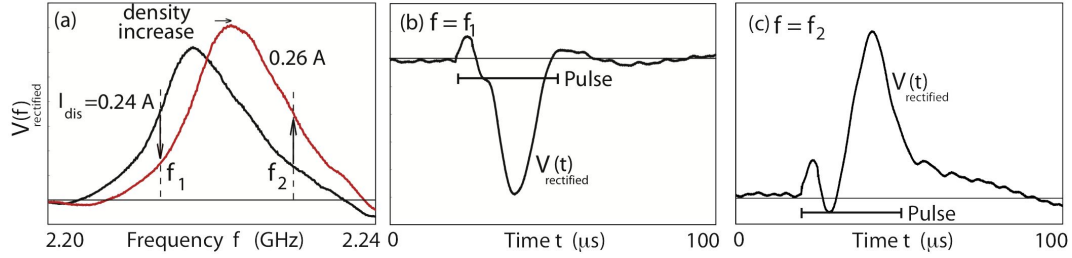


Figure 21. Principle of detecting density fluctuations with a microwave resonator probe. (a) Measured resonance curves at two different plasma densities. (b) Amplitude change for a density pulse when the microwave frequency was tuned to the low frequency side of the resonance curve (f_1). (c) Reverse sign for the amplitude change occurs when the microwave frequency was tuned to the high frequency side of the resonance curve (f_2).

fluctuation produces a large amplitude fluctuation. The sign of the fluctuation is defined by which side of the resonance curve the selected frequency lies on. This is best shown by, as was done in Subsection 4.4, by adding a pulse to the source plasma accelerating voltage, which in turn produced a propagating density increase in the target plasma. When the microwave frequency was chosen to coincide with the positive slope of the resonance line ($f = f_1$), the upshift of the resonance curve produced a decrease in microwave signal on the resonator, hence a negative pulse [Fig. 21(b), pulse starts at first]. On the other hand, a positive pulse was observed when the microwave frequency was chosen to coincide with the negative slope of the resonance line [$f = f_2$, Fig. 21(c)]. Thus, the sign and amplitude of small ion acoustic fluctuations could be clearly identified.

In order to relate the amplitude change to the density change one has to determine the shift of frequency with density and the slope of the resonance curve. Figure 22(a) shows the shift of the resonance curve with density in the target plasma. The slope of the resonance curve can be obtained from this figure. When the data is presented as a contour plot in Fig. 22(b), following the maximum yields the slope, dn/df , displaying the relation between discharge current and density [Fig. 3(b)]. From the slope of the resonance curve, dV/df , and the line shift, dn/df , one obtains the relation between amplitude and density fluctuations, dn/dV .

We then used this scattering technique to diagnose plasma density perturbations due to test signals and turbulent waves. First we verified the properties of test pulse propagation obtained earlier from probe measurements. Figure 23(a) shows a family of ion velocity analyzer traces for different beam energies. Figure 23(b) displays a corresponding contour plot of the microwave amplitude perturbation vs time at a fixed distance from the beam injection point. As observed before, the largest perturbation occurs for intermediate beam energies, $eV_{beam} \simeq 4$ eV, where the ion beam instability has the largest growth rate. Low and high beam energies showed little density perturbations. Thus, the microwave scattering measurements were entirely consistent with the earlier probe measurements.

We then analyzed the effect of density fluctuations on the electromagnetic wave signal. Figure 24(a) displays the resonance line in a plasma with and without magnetic field. The observed increase in density is due to improved electron confinement but it is very clear that the fluctuation level was greatly enhanced in the presence of a magnetic field. The rectified microwave signal fluctuated strongly as the frequency was swept over the resonance line.

Keeping the microwave frequency constant and tuned to the slope of the resonance curve, we then investigated the spectrum of the microwave with a spectrum analyzer. Figure 24(b) displays a logarithmic plot of the microwave spectrum of the signal transmitted through the resonator. The applied signal was monochromatic, the transmitted signal had strong sidebands due to scattering (phase modulation) by the low frequency plasma turbulence. The same effect arises when an electromagnetic wave penetrates through a layer of turbulent plasma around a reentry rocket.

Further scattering measurements are presented in Fig. 25 for three conditions: (a) The incident electromagnetic wave (no plasma), (b) the spectrum in a quiescent plasma and (c) in a turbulent plasma. The large center line is the applied signal at $f = 2.3$ GHz. It appears narrower than in Fig. 24(b) but this is instrumental since the bandwidth of the spectrum analyzer was reduced to 1 kHz to allow a display with higher resolution. The four small lines adjacent to the main line were not due to plasma effects but picked up extraneously. The broad sidebands were produced by density fluctuations in the plasma.

The effect of the axial magnetic field was to confine the electrons to move along \mathbf{B}_0 which produced a denser plasma column along the axis of the device. The ions were not confined by the relatively weak magnetic field. The different ion and electron motions are thought to lead to the observed enhancement of the fluctuation levels.

The variation of noise with magnetic field is shown in Fig. 26. The waveforms [Fig. 26(a)]

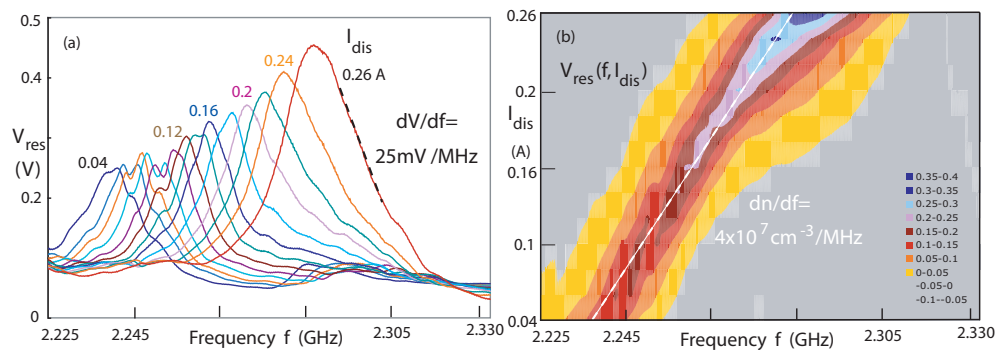


Figure 22. Shift of the resonance line with target plasma density. (a) Line plots showing also the slope of a resonance curve. (b) Contour plot of the above lines which yields the slope, dn/df . The absolute density fluctuations can be determined from the slopes dV/df and dn/df .

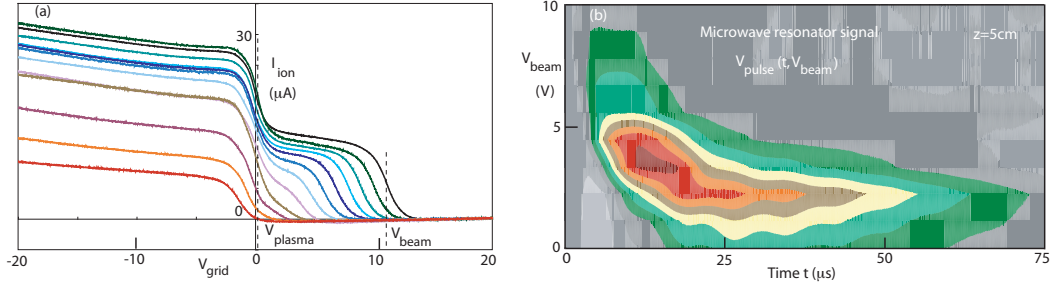


Figure 23. Microwave measurement of a density pulse for different ion beam energies. (a) Ion velocity analyzer traces for different beam energies. (b) Density perturbation measured with the microwave resonator at $z = 5$ cm from the beam source vs time and beam energy. The largest growth and amplitude occurs for a 4 eV beam.

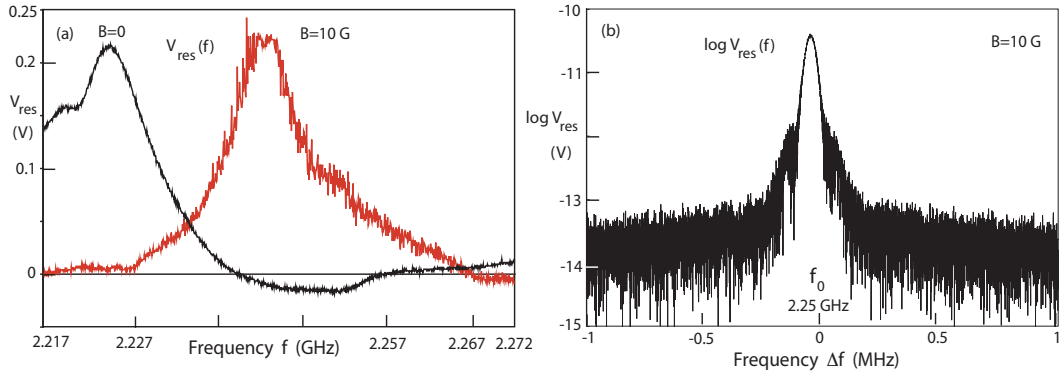


Figure 24. (a) Resonance curves in a quiescent and a noisy background plasma. (b) Spectrum of the microwave signal tuned to the slope of the resonance line in a noisy plasma.

show broadband noise in the low-frequency ion acoustic branch. The amplitude [Fig. 26(b)] increased rapidly with field strength but leveled off when the energetic electrons became fully magnetized. The mechanism for generating this noise could be current-driven ion sound turbulence as shown in earlier similar experiments [30].

4.8 Oscillations in Plasma Bubbles

4.8.1 Sheath Instability

The presence of an instability is readily observed in the probe and grid currents. A few basic properties are shown here but the instability has many features which will be described in more detail below. Since most external variables as well as diagnostic probes modify the bubble the instability becomes a coupled multi-parameter problem. A firm conclusion is that the source of the instability lies in the inner sheath.

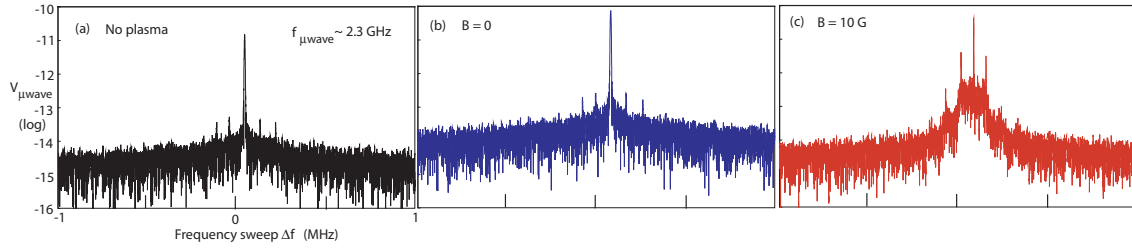


Figure 25. Microwave spectra effected by density fluctuations. (a) Natural line width of the microwave source. (b) Line spectrum in a quiescent plasma. (c) Line spectrum broadened by plasma turbulence.

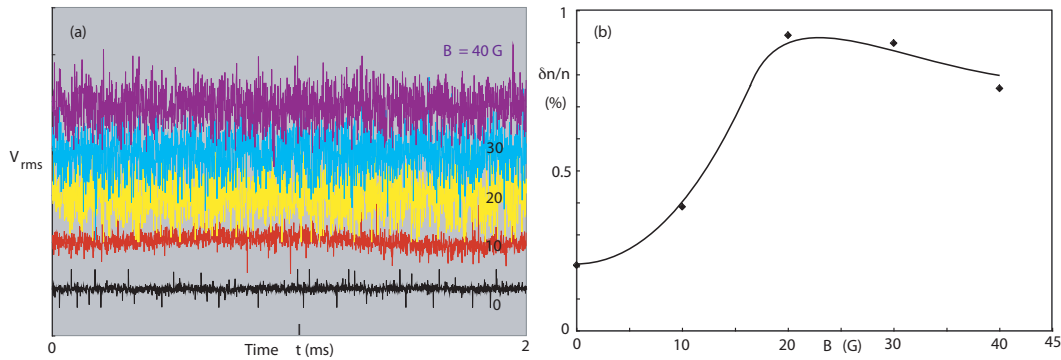


Figure 26. Growth of density fluctuations with magnetic field.

Starting with the grid current, Fig. 27(a) depicts the dc and ac current for a range of grid voltages. The grid current oscillation can be fairly monochromatic as shown by the inserted ac waveform and spectrum. The frequency is close to the ambient ion plasma frequency. The ac to dc current ratio can be of order 10%, but this does not represent the fluctuation in the ion density since the ac current is mainly a displacement current, as shown below. Frequency and amplitude depend on grid voltage as shown in Fig. 27(b). The largest amplitude is observed for grid voltages near the discharge voltage, i.e. when energetic electrons are prevented from entering the sphere. In this regime a subharmonic and several harmonics are also observed. For high grid voltages which form a virtual anode the sheath oscillates at the highest frequency and has a relatively broad bandwidth.

It can be seen that the dc current to the grid has no influence on the instability. The instability even exists without dc grid current ($V_{\text{grid}} \simeq -48$ V). Thus a floating grid oscillates provided it encloses a bubble. The frequency dependence on grid voltage is not universal and can depend on grid mesh size and geometry as will be shown later.

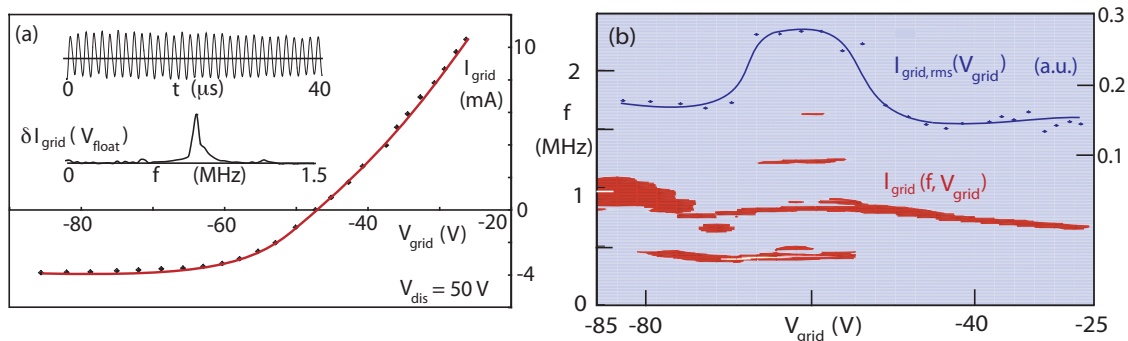


Figure 27. Sheath oscillations at different negative grid voltages. (a) I-V characteristics of the 8 cm diam grid. Insert shows waveform and spectrum of the grid current oscillations at the floating potential ($I_{\text{grid,dc}} = 0$). (b) Frequency of the sheath oscillations vs dc grid voltage.

4.8.2 Sheath Resonance

The source of the instability has been determined with movable probes. In order to also demonstrate the sheath resonance the instability is triggered with a tone burst whose frequency can be varied. The tone burst is applied to the discharge voltage which changes the energy and density of the energetic electrons that can enter the bubble. The ion density

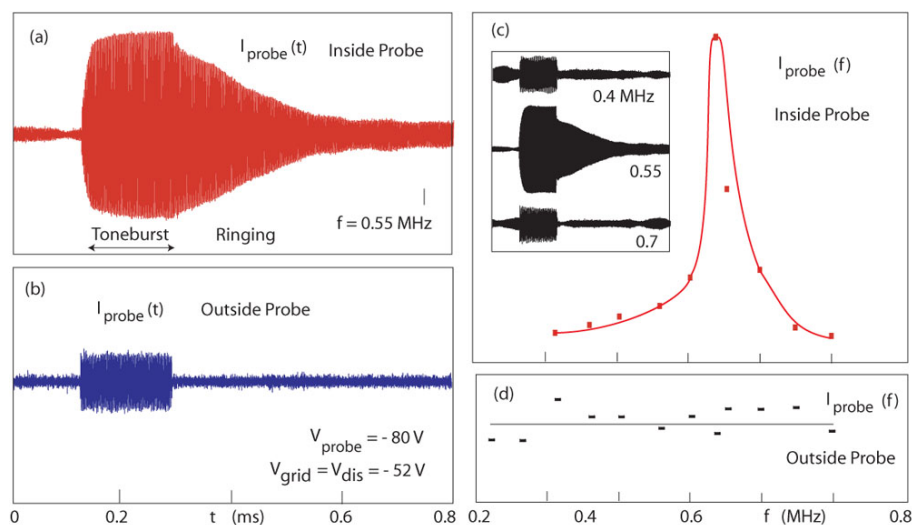


Figure 28. Excitation of the sheath oscillation with a tone burst. (a) Probe signal inside the bubble exhibits a long-lasting ringing at the instability frequency. (b) A probe outside the bubble observed no ringing response or instability. (c) Tone bursts of different frequencies excite a sharp resonance in the bubble but (d) no resonance in the ambient plasma.

is not changed since I_{dis} is nearly independent of V_{dis} . The probes are biased in the ion saturation regime. Figure 28(a,b) show the probe signals observed inside and outside the bubble. The latter, only 5 mm from the grid, shows only the applied tone burst, while the inner probe shows not only a much larger signal but also a long-lasting ringing whose duration depends on frequency. When the frequency is tuned [Fig. 28(c,d)] the inside oscillations exhibit a pronounced resonance, the outside sheath does not. The resonance frequency is the same as the instability frequency without tone burst. Passive measurements of the oscillation amplitude without tone burst show the same result: It is the *inside* sheath which oscillates while the outside sheath is stable.

4.8.3 Scaling of Instability with Plasma Density

The instability exhibits predictable scaling only in limited parameter regimes. For example, the density dependence was found to be $f \propto f_p$ but this result breaks down at high densities where the grid becomes transparent to electrons. Figure 29(a) shows the spectrum of $I_{\text{grid,rf}}$ vs density which exhibits two distinctly different modes. For low discharge currents or large Debye lengths and a grid voltage sufficiently negative to repel all ambient electrons, the ions are reflected at the inner grid and oscillate in a “virtual anode” mode. Its frequency scales as mentioned earlier. For large discharge currents the 1 mm grid opening [Fig. 1(b, left picture)] is too large to form closed equipotential surfaces such that electrons leak into the bubble. This is evident from the drop in floating potential shown in Fig. 29(b). This “electron” mode has a fundamental frequency well below the “virtual anode” mode and a rich spectrum of harmonics whose frequencies rise little with density.

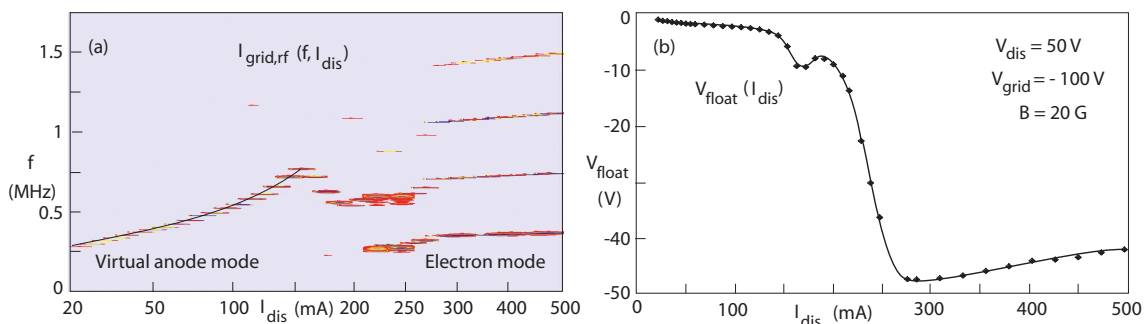


Figure 29. Mode change from a virtual anode mode to a bubble volume oscillation. (a) Spectrum of grid oscillations vs density. The grid voltage is much larger than the discharge voltage, hence repels all electrons at low densities. But as the density increases the Debye length becomes smaller than the grid opening and electrons enter into the bubble which changes the spectrum and (b) lowers the potential inside the bubble.

4.8.4 Sheath Oscillation Discontinuities

The frequency scaling with grid voltage also exhibits sheath discontinuities. Figure 30(a) shows a set of spectra for $I_{\text{grid,rf}}$ vs $V_{\text{grid,dc}}$ for different densities. The grid voltage is swept slowly (0.5 s) which is essentially the same as steady-state conditions. The sphere is made of fine-mesh grid which avoids the mode jump of Fig. 29. With increasing negative grid voltage the floating potential drops to a minimum and then rises again as all electrons are all repelled [Fig. 30(b)]. The sheath oscillates in the virtual anode mode which exhibits several discrete frequencies that may also appear as a broadband modulation. The frequency assumes a minimum near the potential minimum. All frequencies scale with density as shown earlier [Fig. 30(c)].

The new feature is a gap in emission at $V_{\text{grid,dc}} \simeq -35$ V just before the virtual anode is formed. A positive jump in floating/plasma potential coincides with the loss of sheath oscillations [Fig. 30(d)]. No potential changes occur in the ambient plasma. The I-V traces of the grid indicate no density modifications in the ambient plasma. The emission gap narrows as the density increases and eventually vanishes. The potential jump appears to be a nonoscillatory sheath instability. As the potential rises the electron density decreases while the ion density increases ($nv = \text{const}$), which leads to a further potential rise, i.e. a runaway process whereby a thick virtual anode is produced which cannot oscillate. Further work is needed to understand these sheath phenomena in detail.

4.8.5 Pulsed Discharges

In order to vary the electron distributions of the ambient plasma the discharge has been pulsed. During the active discharge the electrons have two populations: Primary electrons with energy given by the discharge voltage (20...80 V) plus the voltage drop along the cathode filament ($\simeq 7$ V) and the bulk of secondary low temperature (2 eV) electrons created by ionization. In the afterglow the primaries are absent and the secondaries have a Maxwellian distribution.

Probes are usually used to measure the energy distribution, but in a bubble plasma the restricted electron supply is easily perturbed by a probe as shown in Fig. 31. The probe is biased to a fixed voltage and the current is recorded vs time during the discharge and afterglow. From a family of current-voltage (I-V) traces shown in Fig. 31(a) the probe characteristics can be constructed at different times as shown in Fig. 31(b). At the start of the discharge (t_1, t_2) a relatively large population of energetic electrons is present which passes through the grid biased at the discharge voltage. The ion current rises as the ambient plasma is produced. In the afterglow no cold electrons can enter or leave the bubble. When the probe is biased negatively the ion current decays slowly but when it is biased positively the current decays faster and as more electrons are collected the decay rate increases. The reason is that the probe depletes the electrons trapped inside the bubble. When I-V traces are constructed in the afterglow they exhibit a negative slope. The electron current decreases with probe voltage since the electrons are depleted faster at

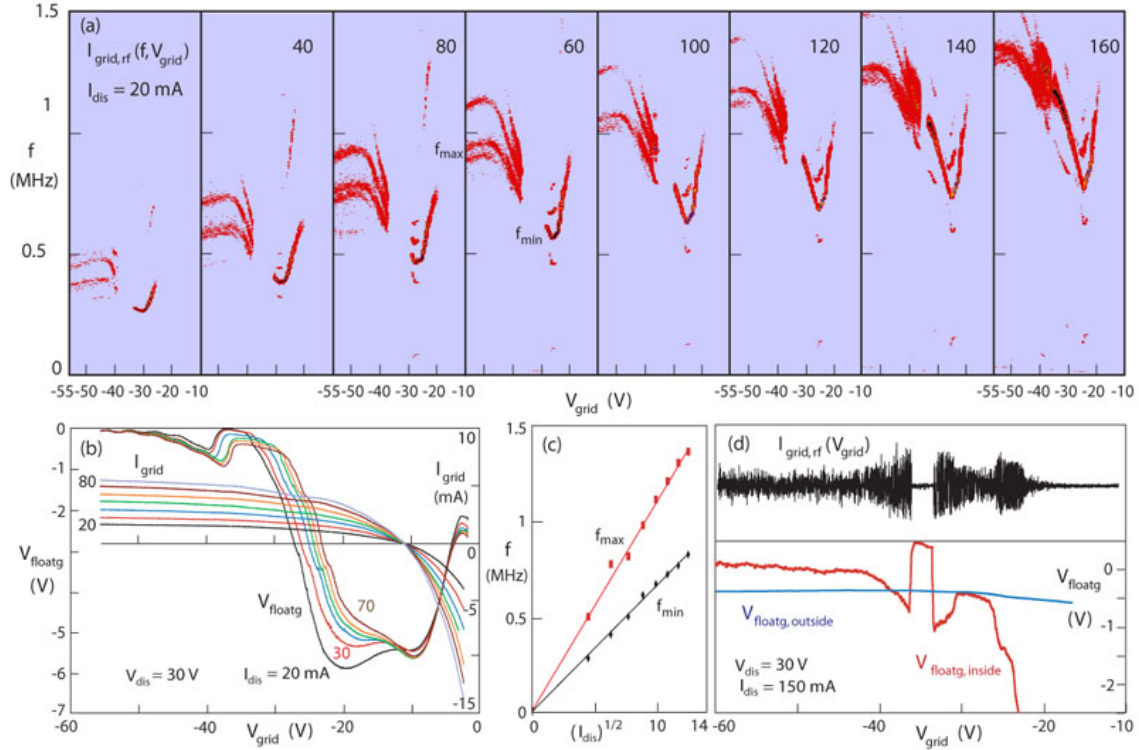


Figure 30. Bubble and instability properties as density and grid voltage are varied. (a) Spectra of $I_{\text{grid,rf}}$ vs $V_{\text{grid,dc}}$ for different densities. (b) Floating potential and grid current vs $V_{\text{grid,dc}}$ for different densities. (c) Frequency scaling with plasma frequency. (d) Simultaneous single-shot traces of $I_{\text{grid,rf}}$ and V_{floatg} , showing that a positive potential jump coincides with the loss of oscillations. Both effects are only observed inside the bubble.

high probe currents. Similar depletion effects have been studied earlier [31].

The probe current affects the sheath oscillations as shown in Fig. 31(c). As the density rises the sheath oscillations start and continue well into the afterglow due to electron and ion trapping. However, when the probe depletes the electrons ($V_{\text{probe}} > 0$) the instability approaches the virtual anode oscillation which has a smaller amplitude, higher frequency and shorter duration in the afterglow. Figure 31(d) displays the spectrum of the oscillations in the afterglow during a time interval indicated in Fig. 31(c). Since the density decays the line width is broadened but the upshift in frequency upon electron depletion by the probe is clearly visible.

Since the bubble plasma is starved for electrons it is easily perturbed by both electron collection and emission. The collection of ions produces little perturbations since the ion flow through the negatively biased grid is not restricted.

How long electrons are trapped is demonstrated in Fig. 32. Although decaying, the oscillations in $I_{\text{grid,rf}}$ are observable for at least 300 μs [Fig. 32(a)]. By measuring the rf

period at discrete intervals one obtains a plot of $f(t)$ [Fig. 32(b)]. Since the frequency scales proportional to the plasma frequency, a plot of f^2 is proportional to the density decay, conveniently displayed on a logarithmic scale. The e -folding density decay inside the bubble has a time constant $\tau \simeq 100 \mu\text{s}$ which is comparable to that of the outside plasma measured from the ion current to the grid [Fig. 32(c)]. Thus, the bubble plasma decays at the same rate as the ambient plasma. Electrons which entered during the discharge are confined inside the bubble. Ions can pass the grid and equalize the inside and outside densities.

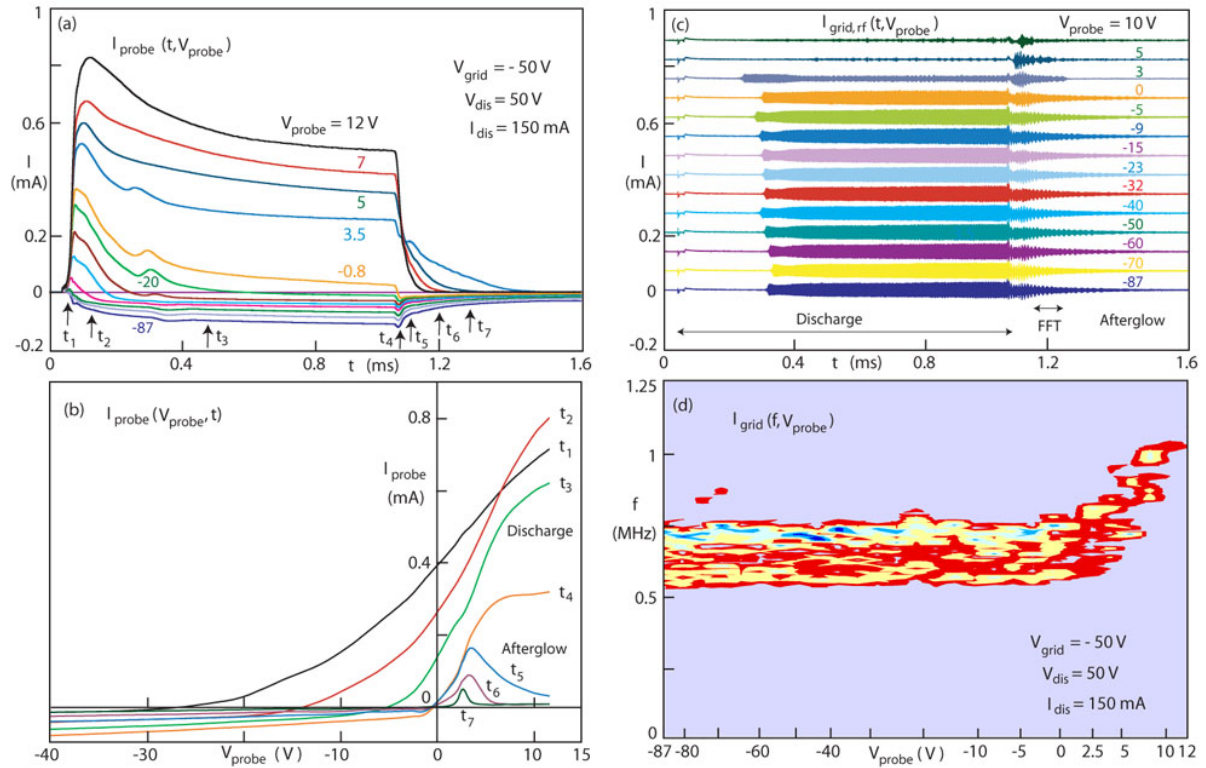


Figure 31. Probe I-V curve inside a plasma bubble embedded in a pulsed discharge plasma. (a) Probe current vs time for different probe voltages, showing a voltage-dependent electron decay time short than the ion decay. It is caused by electron depletion by the probe which results in a negative differential conductance, $dI/dV < 0$, in the afterglow where no electrons can enter the sphere. (c) Rf waveform of the grid current for different probe voltages. Note oscillations extend into the afterglow where electrons are trapped inside the bubble. (d) Spectrum of the oscillations in the afterglow [time indicated in (c)]. The line is broad since the density decays during the FFT. The probe changes the frequency when electrons are collected.

4.8.6 Pulsed Grid Voltage

The grid voltage controls the electron flow into the bubble. For large negative voltages the electrons cannot enter the sphere and a large positive space charge layer develops near the inner grid which reflects the incident ions, leaving the volume essentially empty. By pulsing the grid voltage the growth and decay of the bubble can be observed.

Figure 33 summarizes the main observations of emptying and refilling of the bubble. In a dc discharge the grid voltage is pulsed from 0 to $V_{\text{grid}} = -120$ V which stops primary electrons of energy $eV_{\text{dis}} = 50$ eV from either entering or leaving the bubble. Due to the electron trapping a large negative transient floating potential develops [Fig. 33(a)]. The ions cannot leave the bubble while the electrons are trapped [Fig. 33(b)]. The decay is *not* given by the ion transit time through the bubble but by the electron loss. Surface recombination on the ceramic probe shafts is the major loss since neither grid nor probe collects electrons.

One can estimate the electron decay as follows: The probe shaft is 2 mm in diameter and 4 cm long when the probe is in the center of the sphere. The probe surface area is $2\pi r_{\text{probe}} l_{\text{probe}} \simeq 2.5 \text{ cm}^2$. The electron flux to a nonconducting surface equals the ion flux, $I_e = I_i = A_{\text{probe}} n e v_i$. The electron current leads to a decay of the electron charge inside the bubble, $I_e = (dn/dt) e (4/3) \pi r_{\text{bubble}}^3$. Thus, for $v_i \simeq 2 \times 10^5$ cm/s and $r_{\text{bubble}} = 4$ cm, the decay time constant is $\tau = n / (dn/dt) = (4/3) \pi r_{\text{bubble}}^3 / (A_{\text{probe}} v_i) \simeq 0.54$ ms, which agrees with the observed decay time $I_i / (dI_i/dt) \simeq 0.5$ ms in Fig. 33(b).

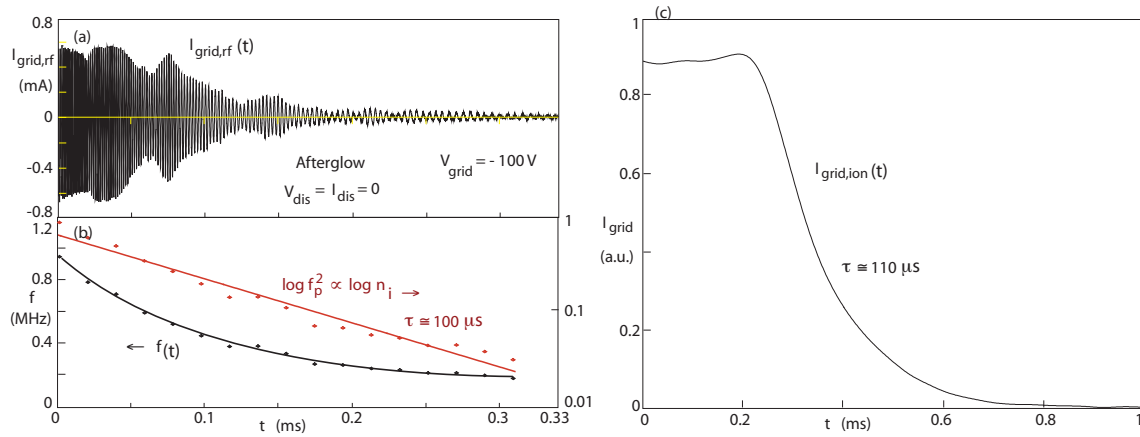


Figure 32. Sheath instability in an afterglow plasma. (a) Oscillations in the grid current of a biased sphere whose frequency decays in time. (b) Frequency decay vs time, $f(t)$. Since the frequency is proportional to the plasma frequency, a plot of $\log f_p^2$ yields the density decay time *inside* the oscillating bubble. (c) The density decay of the *outside* plasma, obtained from the decaying ion grid current, is comparable to the bubble decay. Electrons are trapped in the bubble while ions flow in and out of the bubble.

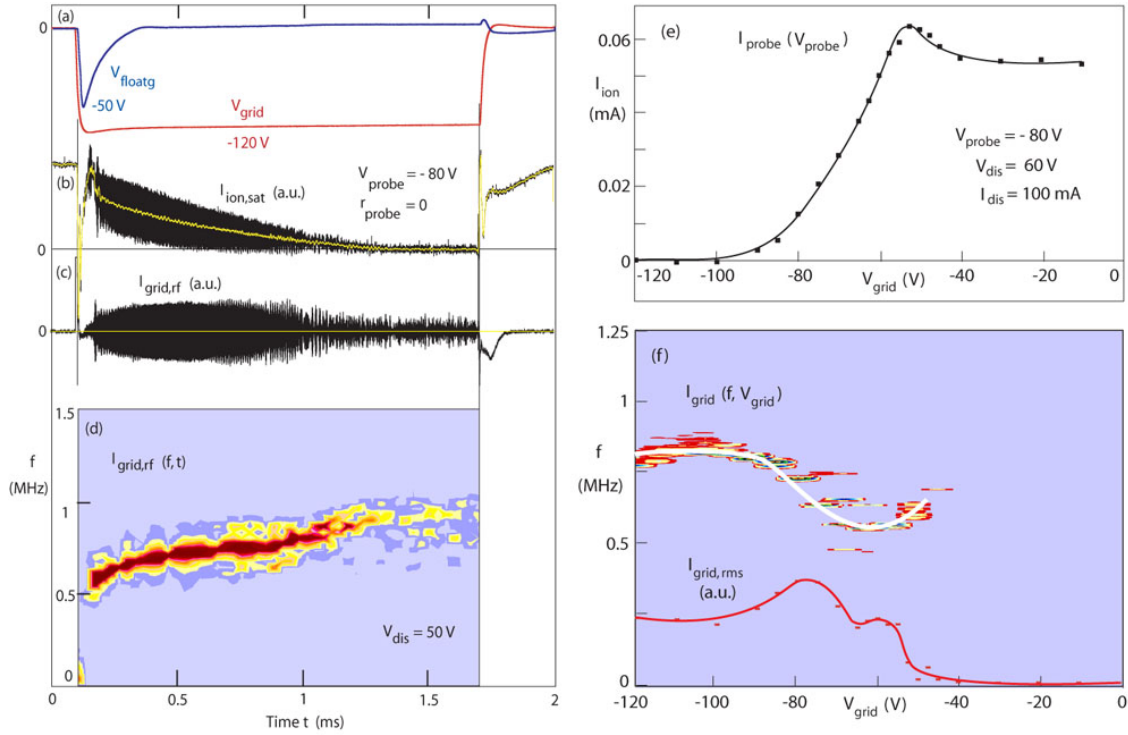


Figure 33. Pulsed grid voltage to observe the emptying and filling of a plasma bubble. (a) Grid voltage $V_{\text{grid}}(t)$ and the floating potential measured with a second probe near the center of the sphere. Initially the floating potential approaches the discharge voltage, indicating trapping of primary electrons. (b) Ion saturation current to a Langmuir probe in the center of the 8 cm diam. sphere. The ions are expelled slowly because the electrons are trapped and both species must decay at the same rate. (c) Oscillation in the grid current which continue as virtual anode oscillations when the bubble is empty. (d) Time-resolved spectrum of the grid current oscillations showing a frequency rise while the density in the bubble decreases. Thus the ion plasma frequency in the bubble volume does not determine the instability frequency, but only in the vicinity of the grid. (e) Dc ion current vs grid voltage showing an empty bubble at large negative grid voltages. (f) Frequency and amplitude dependence of $I_{\text{grid,rf}}$ vs $V_{\text{grid,dc}}$.

The impact of 120 eV ions on the stainless steel grid does not release sufficient secondary electrons to balance the electron losses. After about 1 ms there are no ions or electrons left in the center of the bubble.

The instability is visible on the probe as long as there is plasma in the center of the bubble. On the grid the oscillations continue while the bubble is empty, showing again that the instability arises from the sheath [Fig. 33(c)]. By dividing the waveform into 50 bins, 400 samples each, and performing a fast Fourier transform (FFT) of each, a time-resolved spectrum of $I_{\text{grid,rf}}$ is obtained [Fig. 33(d)]. As electrons are gradually removed from the sheath the frequency increases to that of virtual anode oscillations.

When the grid voltage is turned off, the empty bubble refills [$t > 1.7$ ms, Fig. 33(b)]. Analogous to free plasma expansion into vacuum electrons and ions expand together at the ion transit time into the sphere. The abundant electron supply from the ambient plasma prevents the sheath from oscillating. When the electron supply is limited, e.g. by switching the grid voltage to V_{dis} instead of 0, the ion flux rises slowly and linearly in time at a rate controlled by the electron flux (not shown).

The amplitude of the grid voltage pulse has been varied in a steady-state plasma. As shown in Fig. 33(e) the ion current in the bubble vanishes only when the grid voltage is more negative than the discharge voltage. For smaller grid voltages the ion influx is not inhibited by the grid voltage. A small enhancement in the ion flux is observed when the grid begins to stagnate the primary electrons.

The spectrum and amplitude of the instability in the grid current as a function of grid voltage are shown in Fig. 33(f). When the bubble is empty ($V_{\text{grid}} = -100$ V) the frequency of the virtual anode oscillations has a maximum. Leaking electrons into the bubble lowers the frequency and increases the oscillation amplitude. The frequency minimum occurs for $|V_{\text{grid}}| \simeq V_{\text{dis}}$ where electrons stagnate in the sheath. For small grid voltages the increase in electron supply prevents the sheath instability.

4.8.7 Triggering the Instability

Pulsing the probe positively creates perturbations in potential and density inside the bubble. When the trigger pulse is made as short as the instability period the growth of the sheath instability can be observed. Transient sheath ringing effects are also generated.

Figure 34 shows the response in the grid and probe currents when a positive trigger pulse (+10 V peak, -20 V baseline, 1 μ s length) is applied to a probe in the center of the bubble. The oscillations in the grid current for different dc grid voltages are shown in Fig. 34(a). For $|V_{\text{grid}}| < V_{\text{dis}} = 60$ V low-frequency (< 100 kHz) oscillations are excited. These are transient phenomena which die out after a few cycles. Their frequency is lowest where the floating potential assumes a minimum or the injected ions have the largest velocity. The period corresponds approximately to the transit time of fast ions through the sphere. Thus the trigger pulse causes a ballistic ion signal to travel from one side of the grid to the other, which triggers the next pulse and the process repeats but decays.

For $|V_{\text{grid}}| > V_{\text{dis}} = 60$ V higher frequency (700 kHz) oscillations are excited. These also exist at a lower level prior to the trigger pulse and continue after the pulse without damping. They are the sheath plasma instability near the ion plasma frequency. Their frequency and amplitude also vary with V_{grid} which is best seen on an expanded time scale shown in Fig. 34(b). The instability has a large amplitude and low frequency at $V_{\text{grid}} \simeq 65$ V. For $|V_{\text{grid}}| \gg V_{\text{dis}}$ the bubble is empty and the probe has no effect on the virtual anode oscillations near the grid. The frequency dependence of the triggered instability on V_{grid} mirrors that of the steady-state instability [Fig. 33(f)].

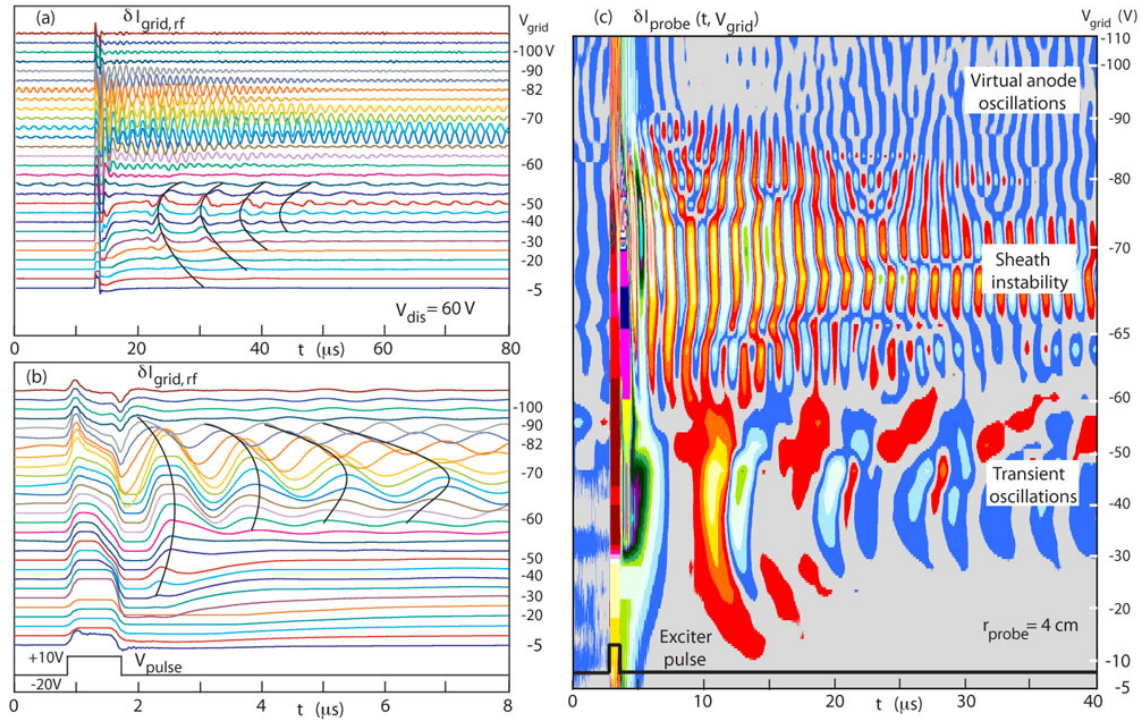


Figure 34. Triggering sheath oscillations with a short trigger pulse applied to an electrode in the center of the sphere. (a) Oscillations in the grid current vs time for different grid voltages. For $V_{\text{grid}} < V_{\text{dis}}$ low frequency transient oscillations are excited which decay in time. For $V_{\text{grid}} > V_{\text{dis}}$ the high frequency sheath instability is excited. (b) Evolution of the high frequency instability on an expanded time scale. The frequency increases with $|V_{\text{grid}}|$ and becomes a virtual anode oscillation when electrons cannot enter into the bubble. (c) Contour plot of the oscillations in the probe ion current near the inner sheath. Three different modes of oscillations can be distinguished.

The oscillations in the probe current have the same character as those in the grid current. The contour plot of Fig. 34(c) shows low-frequency transients, the sheath instability and virtual anode oscillations of the inner bubble sheath. Since the probe is near the grid the virtual anode oscillations are detected, although weaker than those in $I_{\text{grid,rf}}$ showing that the positive space charge layer extends a few mm beyond the grid. No virtual anode oscillations are observed in the center of the bubble [Fig. 33(b)].

By comparing probe and grid signals a timing difference is observed. The low-frequency perturbation is first seen on the probe, followed by a delayed one on the grid. Thus the perturbation travels toward the grid and must have originated from the center or opposite side of the sphere.

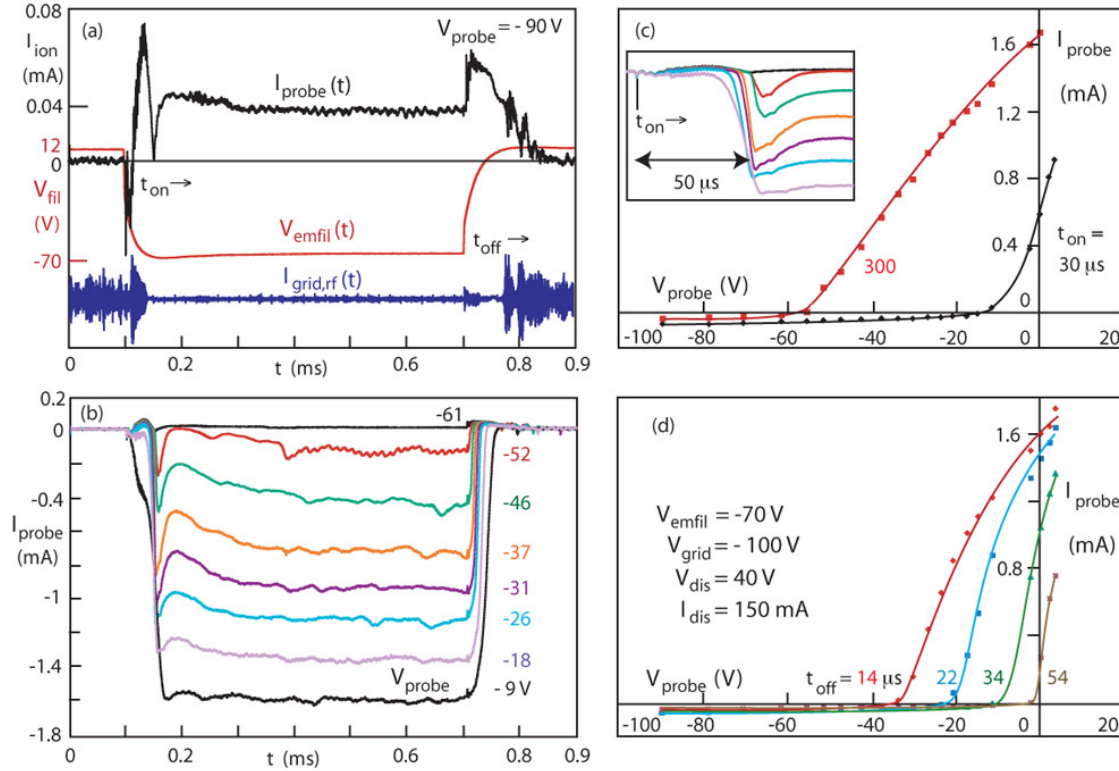


Figure 35. Change of bubble parameters by a pulsed emissive probe. (a) Ion saturation current of a Langmuir probe, bias voltage of an emissive probe and grid rf oscillations. The initially empty bubble is filled with ions which are neutralized by electrons from the emissive probe. The instability is quenched by a large electron supply. **(b)** Langmuir probe currents for different probe bias, collecting electrons from the emissive probe. **(c)** Probe I-V characteristic at the onset of the emissive probe pulse. The peak electron energy is close to the emissive probe voltage. **(d)** Langmuir probe characteristic after the end of the emissive probe pulse where the energetic electrons are lost to the probe.

4.8.8 Bubble Properties with an Internal Emissive Probe

In a steady state discharge plasma an empty bubble has been established by biasing the grid sufficiently negative to exclude all ambient electrons. Then the internal emissive probe is pulsed negatively to study the filling of the bubble by space charge neutralized ions. Figure 35(a) shows the ion saturation current of the Langmuir probe, the emissive probe voltage and the grid current oscillations in time. Within the rise time of V_{emfil} the ion current rises with an overshoot and the virtual anode instability is quenched. When V_{emfil} is switched off the ion current decays after an initial overshoot and the sheath oscillations start again.

Figure 35(b) shows probe traces for different probe voltages when electrons are collected.

The emissive filament is the electron source which supplies the probe current and the injected ion current. The current rises fast but its onset is delayed as shown in the insert of Fig. 35(c). The delay indicates the time of arrival of ions at the center of the bubble since without plasma the electron emission is negligibly small. The rapid rise in electron emission causes a drop in plasma potential which leads to the decrease of ion current during the emissive probe pulse. The I-V trace shows that the potential drops by at least 50 V when the electron current rises after turn-on. At the end of the pulse [Fig. 35(d)] the floating potential rises within the fall time of V_{emfil} , which increases the ion current until it drops due to the loss of neutralizing electrons. As the bubble empties virtual anode oscillations reappear in the grid current.

The emissive filament current has been varied by changing the heater current. The ion current into the bubble varies proportional to the emitted electron current. When the emission is decreased the potential drop also decreases. The resulting ion current vanishes and so does the appearance of the current overshoots. Furthermore, restricting the electron supply restarts the sheath instability during the pulse. Its frequency is lower than that of virtual anode oscillations, as shown in Fig. 33(d). The frequency drops with increasing electron supply since the charge density in the sheath is reduced (Fig. 36). For the same reason, the frequency assumes a minimum at $|V_{\text{grid}}| \simeq V_{\text{dis}}$ when external electrons stagnate in the grid [see Fig. 30(a) or Fig. 33(f)].

The electron injection into an ion-rich sheath is complementary to the ion injection into an electron-rich sheath which has been studied earlier [25, 32]. It lowers the charge density in the sheath which requires the sheath to widen and/or its potential to drop.

For very low emission currents the bubble density becomes negligibly small and so does the instability amplitude. Thus, there is an optimum emissive probe current producing the largest oscillations as is documented in Fig. 36. The nonlinear scale for I_{emfil} results from the strong temperature dependence of emission. The probe rf current amplitude can exceed the dc ion current from which it is concluded that it is not an ion density oscillation but a displacement current due to the oscillating plasma potential.

4.8.9 Spectra with Langmuir and Emissive Probes

A positively biased Langmuir probe modifies the emission from an emissive probe inside a bubble. Now we show how the instability is affected by sweeping the probe voltage.

Figure 37 displays spectra of $I_{\text{grid,rf}}$ vs V_{probe} for different V_{emfil} in a constant ambient plasma. Since the probe voltage was not a linear function of time the scale of V_{probe} is nonlinear. The grid voltage is constant and sufficiently negative to keep all external electrons from entering the bubble. Ions enter the bubble with the Bohm flux. The grid also remains negative with respect to the emissive probe so as to reflect all internal electrons. Electrons are lost only by surface recombination with ions on insulators except when the Langmuir probe is biased positive with respect to the emissive probe. The electron confinement is the reason why a probe can easily perturb the electron distribution

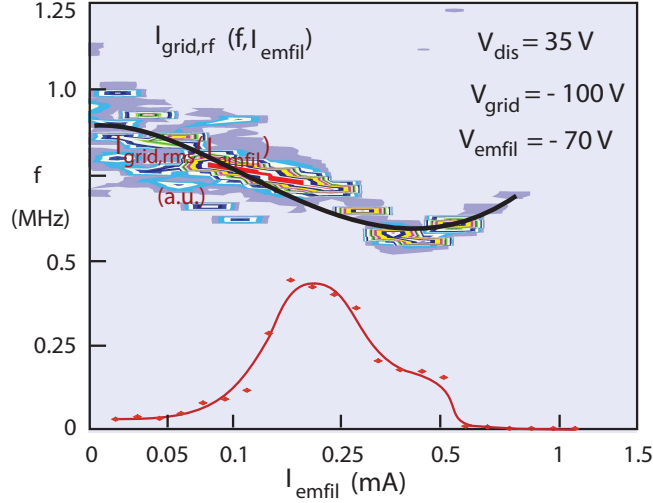


Figure 36. Frequency and amplitude of the sheath instability vs electron emission current. The grid is biased so as to exclude electrons from the ambient plasma. The frequency drops when electrons reduce the space charge in the sheath. A large electron supply quenches the instability. Without electrons virtual anode oscillations remain.

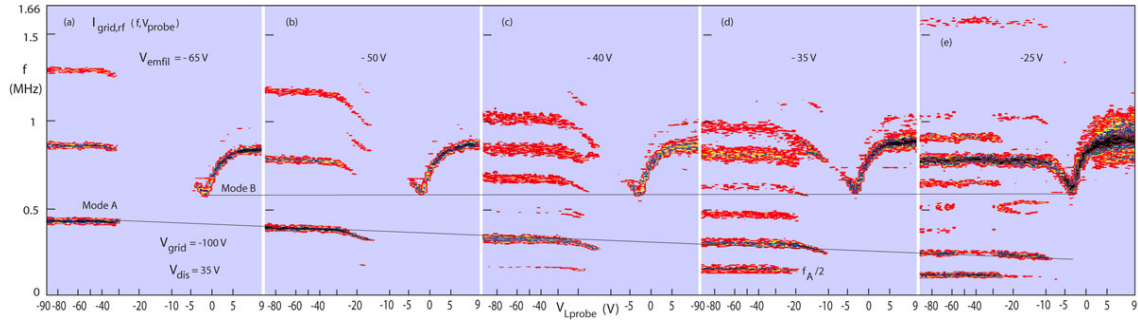


Figure 37. Spectrum of the sheath instability $I_{\text{grid,rf}}$ vs Langmuir probe voltage V_{probe} for different emissive probe voltages, V_{emfil} . The grid bias prevents electrons from the ambient plasma to enter into the bubble. The Langmuir probe changes the amplitude and frequency of the instability because it collects electrons from the emissive probe which modifies the plasma potential and sheath properties. Interesting features are multiple modes, copious harmonics and a frequency dip when V_{probe} is close to the ambient plasma potential.

and modify the sheath instability.

Two modes of oscillations can clearly be distinguished in Fig. 37(a). Mode A arises when the probe collects ions but no electrons. The frequency f_A is independent of V_{probe} until the probe begins to draw electrons. Then the frequency drops and the instability is quenched as clearly seen in Fig. 37(b). Mode A has a rich spectrum of harmonics including odd half harmonics, $nf_A/2$ where $n = 1, 2, \dots, 8$.

As the probe is biased positively mode B is excited. It has a pronounced frequency minimum when V_{probe} is close to the ambient plasma potential. Further increase of V_{probe} raises the frequency toward that of virtual anode oscillations. No dip is seen when $|V_{\text{grid}}| < |V_{\text{emfil}}|$ and the emissive filament supplies abundant electrons.

Based on the previous investigations the probe perturbation can be explained as follows: The emissive probe and the Langmuir probe form an anode-cathode system where the plasma potential is determined by the anode potential. The probe raises the plasma potential when it collects electrons. Mode B is excited because the probe depletes electrons. The temperature-limited emission current is diverted to the probe rather than to neutralize the injected ions.

When the Langmuir probe raises the internal plasma potential close to the external plasma potential the ion influx is reduced. The decrease in the ion flux compared to the electron flux lowers the frequency of the sheath instability. When the bubble plasma potential exceeds the external plasma potential virtual anode oscillations remain.

When the emissive probe potential is reduced [Fig. 37(a-e)] the frequency of mode A and its harmonics is reduced. As shown in Fig. 2(d) of Ref. [22], I_{emfil} decreases with V_{emfil} , hence the injected ion current must also decrease. A lower ion density leads to a decrease of the instability frequency.

With decreasing electron energy odd-half harmonics of mode A become abundant. They must be the results of nonlinear sheath oscillations since their harmonics are above the ion plasma frequency where ion acoustic waves are evanescent.

The instability depends on many parameters such as V_{grid} , V_{emfil} , I_{emfil} , V_{dis} , I_{dis} and V_{probe} , whose coupling can produce perplexing results. We limit the parameter space by keeping the discharge and V_{emfil} constant while varying V_{grid} and V_{probe} . As shown in Fig. 38(a,b) the frequency dependence on V_{grid} can be completely changed by a biased Langmuir probe. In order to explain these effects it is helpful to display the probe I-V characteristics in Fig. 38(c) keeping however in mind that the electron branch has modified the electron distribution.

When the probe is biased negatively [Fig. 38(a)] the lower frequency mode A is excited with harmonics. For $V_{\text{grid}} \leq V_{\text{emfil}}$ its frequency f_A increases with $|V_{\text{grid}}|$. The probe traces of Fig. 38(c, bottom) show that the ion current, which is not subject to probe errors is nearly independent of $|V_{\text{grid}}|$. Since the emission current equals the injected ion current it must also remain constant requiring a nearly constant plasma potential for space charge limited emission. For constant electron energy and density the electron density in the sheath must decrease as the grid becomes more negative. Since the net space charge density determines the oscillation frequency it increases with $|V_{\text{grid}}|$.

When $V_{\text{grid}} \simeq V_{\text{emfil}}$ electrons stagnate in the sheath and the oscillation frequency assumes its minimum. When the grid is positive with respect to the emissive probe it collects a larger, temperature limited electron current which usually quenches the sheath instability.

For $V_{\text{probe}} = 0$ the probe collects electron currents which for $V_{\text{grid}} \leq V_{\text{emfil}}$ are supplied by the emissive probe and for $|V_{\text{grid}}| \leq V_{\text{dis}}$ are from the ambient plasma. Mode B is excited whose frequency has a maximum at $V_{\text{grid}} \simeq V_{\text{emfil}}$ which coincides with a minimum in the electron current to the probe. For $V_{\text{grid}} < V_{\text{emfil}}$ the probe electron saturation current increases with lowering $|V_{\text{grid}}|$, hence more energetic electrons are able to penetrate into the sheath which lowers the frequency. The frequency also decreases when $|V_{\text{grid}}| \leq V_{\text{dis}}$ since both Langmuir probe and the grid collect electrons from the ambient plasma and the emissive probe. The penetration of electrons into the sheath lowers the oscillation frequency until the instability is quenched by the abundance of electrons.

An alternative display is the frequency dependence on V_{probe} for different values of V_{grid} which reveals further details of the instability. Figure 39(a) displays spectra of $I_{\text{grid,rf}}$ vs V_{probe} for 10 different values of V_{grid} . Mode A is excited for negative probe voltages and mode B when the probe collects electrons. For grid voltages $V_{\text{grid}} < V_{\text{emfil}}$ the conditions are similar to those of Fig. 37: The neutralizing electrons are only supplied by the emissive probe. As long as the probe collects only ions its bias hardly affects the frequency of mode A. But when the probe starts to collect electrons the frequency of

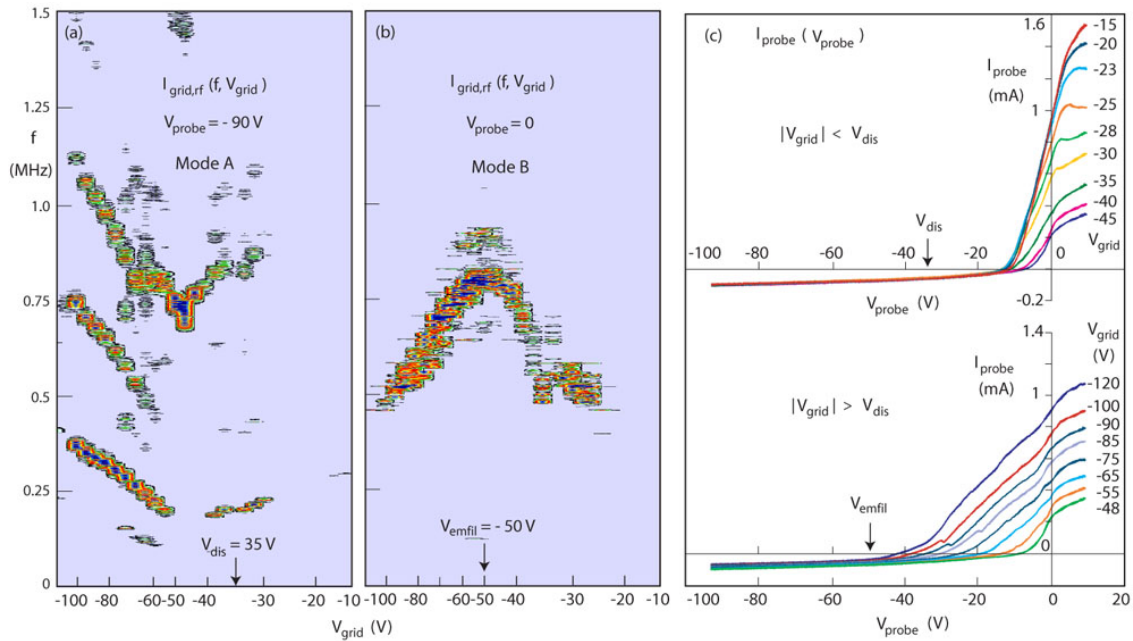


Figure 38. Spectrum of grid current oscillations vs dc grid voltage perturbed by Langmuir probe currents. (a) Spectrum $I_{\text{grid,rf}}$ vs $V_{\text{grid,dc}}$ when the probe draws ions which produces negligible perturbations. (b) $I_{\text{grid,rf}}$ vs $V_{\text{grid,dc}}$ when the probe draws electrons, which changes the frequency and its dependence on V_{grid} . (c) Probe I-V characteristics for different $V_{\text{grid,dc}}$. For $|V_{\text{grid}}| > V_{\text{dis}}$ the electrons are supplied from the emissive probe, for $|V_{\text{grid}}| < V_{\text{dis}}$ electrons from the ambient plasma also enter into the bubble. When the Langmuir probe collects electrons the plasma potential rises with increasing probe bias.

mode A drops and the instability is quenched.

The instability reappears in mode B when the probe voltage is close to the ambient plasma potential. Mode B exhibits a sharp dip in frequency at $V_{\text{probe}} \simeq 0$ irrespective of V_{grid} . Since there is no enhanced electron emission it is thought that the ion inflow is reduced when the probe pulls the plasma potential close to the ambient plasma potential.

Decreasing the grid voltage to $|V_{\text{grid}}| = V_{\text{emfil}}$ raises the frequency of mode B while lowering that of mode A. The latter has been explained by the penetration of electrons into the ion rich sheath as the potential difference between grid and emissive probe decreases. Electrons lower the charge density which drops the oscillation frequency. The frequency increase of mode B indicates a loss of electron flux with decreasing $|V_{\text{grid}}|$. Figure 37(c) and Fig. 38(c, bottom) show that the probe current for $V_{\text{probe}} = 0$ decreases with $|V_{\text{grid}}|$, reaching a minimum at $V_{\text{grid}} \simeq -45$ V. While the electron current decreases the ion current slightly increases. Thus, the frequency increase in mode B is due to the increasing ratio of ion flux to electron flux.

In the regime $|V_{\text{grid}}| > V_{\text{dis}}$ the plasma potential is determined by the injection of ions through the grid and the emission of electrons from the hot filament and their respective loss rates. As shown in Fig. 39(b) the floating potential becomes increasingly negative with increasing $|V_{\text{grid}}|$ since the electrons are trapped for $V_{\text{grid}} < V_{\text{emfil}}$ while the ion flux gradually decreases with $|V_{\text{grid}}|$ [Fig. 39(c)]. Measurements of the floating potential and ion current are non-perturbing. But for a positive probe bias the probe raises the plasma potential when it is the only electron sink which is the situation for mode B. Thus, the frequency increase for mode B is due to the increased ratio of ion to electron flux [see Fig. 39(d)] which produces an increasingly positive space charge density in the sheath and a rising frequency of oscillations up to $|V_{\text{grid}}| \simeq V_{\text{dis}}$. The sharp frequency dip at $V_{\text{probe}} \simeq 0$ occurs when the probe pulls the plasma potential close to the ambient plasma potential such that the ion inflow is reduced and the ion outflow enhanced. No virtual anode is formed since neutralizing electrons are present. Few harmonics are observed when the probe and grid collect the electrons.

Mode A is observed when the emitted electrons have no sink other than surface recombination, provided both grid and probe are biased below V_{emfil} . Although not measurable the electron flux must decrease with $|V_{\text{grid}}|$ for the following reason: The emissive probe emits relative to the plasma potential which must be above but close to the floating potential. As the plasma potential decreases with $|V_{\text{grid}}|$ the space charge limited emission also drops. A dwindling emission and decreasing electron energy increases the space charge density in the sheath which in turn results in a high oscillation frequency for large negative grid voltages.

When the grid voltage is comparable to the emissive probe voltage the emitted electrons stagnate in the sheath. Mode A assumes a frequency minimum and produces copious harmonics and odd half harmonics. Thus, slow electrons in the sheath appear to be associated with nonlinear oscillations. Previously, subharmonics have only been observed when the sheath instability is driven by an oscillating grid voltage [33]. For

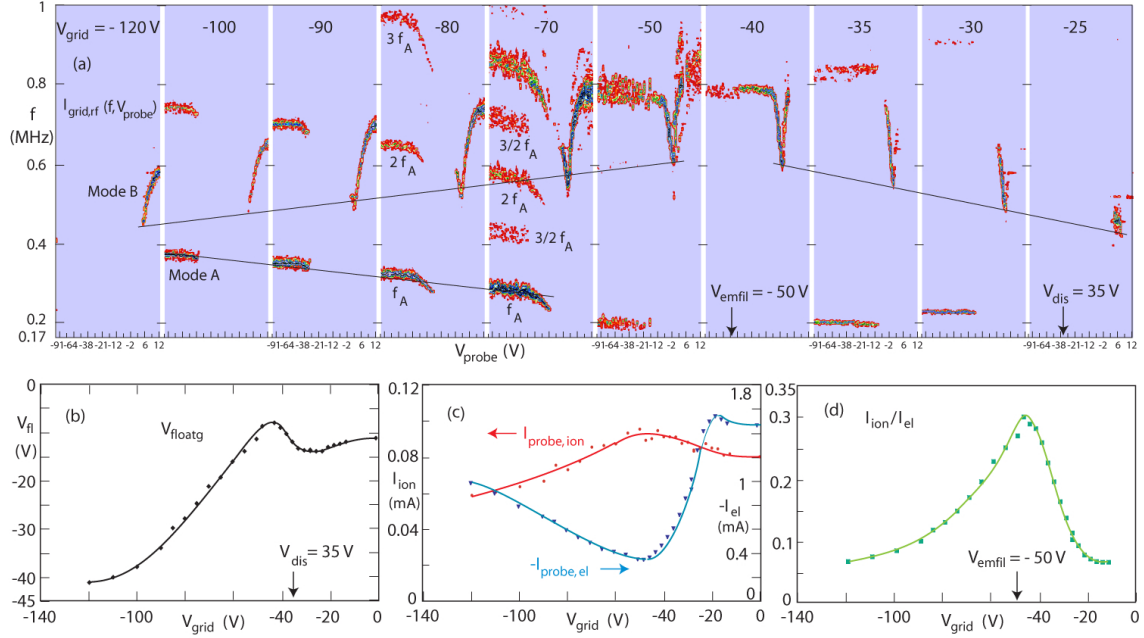


Figure 39. Bubble plasma parameters and instability properties for different Langmuir probe voltages and grid voltages. (a) Spectrum of $I_{\text{grid},\text{rf}}$ vs V_{probe} for different V_{grid} and fixed $V_{\text{emfil}} = -50 \text{ V}$ and $V_{\text{dis}} = -35 \text{ V}$. When $|V_{\text{grid}}| > V_{\text{dis}}$ the electrons in the bubble are supplied by the emissive probe which excites mode A for negative probe bias and mode B for probe bias $V_{\text{probe}} > V_{\text{emfil}}$. For $|V_{\text{grid}}| \leq V_{\text{dis}}$ electrons from the ambient plasma enter the sphere which reverses the frequency dependence $f(V_{\text{probe}})$. A pronounced frequency dip occurs when the probe is biased close to the ambient plasma potential. Copious harmonics arise when the electrons are neither collected by the grid ($V_{\text{grid}} \leq V_{\text{emfil}}$) or probe ($V_{\text{probe}} \leq V_{\text{emfil}}$). (b) Floating potential of the Langmuir probe vs grid voltage showing that the emissive probe prevents the formation of a virtual anode. (c) Probe electron and ion saturation currents vs V_{grid} . (d) Ratio of ion to electron current vs V_{grid} , showing a pronounced maximum when $V_{\text{grid}} \simeq V_{\text{emfil}}$ where mode B has a frequency maximum, mode A a minimum.

$V_{\text{grid}} \geq V_{\text{emfil}} = -50 \text{ V}$ the emitted electrons are collected by the grid and/or the probe whichever is more positive with respect to the emissive probe. Harmonics and odd half harmonics disappear when the plasma potential is tied by electron sinks. When the probe pulls the plasma potential close to the ambient plasma potential the rejection of ions produces the pronounced frequency dip in mode B. There is no enhancement in the electron current at the dip. It is noteworthy that the sheath can oscillate simultaneously at two different frequencies not related as harmonics [see $V_{\text{grid}} = -50$ or -35 V , $V_{\text{probe}} < -20 \text{ V}$]. Virtual anode-like oscillations are observed for very positive probe voltages.

Energetic electrons from the ambient plasma enter the bubble when $|V_{\text{grid}}| \leq V_{\text{dis}}$. As $|V_{\text{grid}}|$ decreases the electron supply increases which raises the electron saturation current

[Figs. 38(c, top traces) and Fig. 39(b)] and, at a constant ion flux lowers the oscillation frequency of mode B. The instability vanishes at low $|V_{\text{grid}}|$ since abundant electrons stabilize the sheath.

Mode A reappears when $|V_{\text{grid}}| \simeq V_{\text{dis}}$. Electrons from the ambient plasma and the emissive probe are mainly lost on the large grid rather than the small Langmuir probe, hence the frequency becomes independent of V_{probe} . It slightly increases as $|V_{\text{grid}}|$ drops before being quenched by the increasing ambient electron flux.

Although mode A and its subharmonic fall into the ion acoustic branch they are not unstable sound waves but sheath instabilities. For $f = 200$ kHz and $(kT_e/m_i)^{1/2} \simeq 2 \times 10^5$ cm/s the wavelengths would be $\lambda = 1$ cm which have not been observed in phase measurements. If the oscillations were due to ion transit times through an 8 cm sphere the ion energy would have to be > 64 eV which is not possible for the observed potential drop between ambient and bubble plasmas.

4.8.10 Electron Leakage Through Coarse Grids

As shown in Fig. 7(b), the mesh size of the grid plays an important role in determining the electron flux through the grid. The two spheres are located in the same ambient plasma and biased to the same negative voltage well above the discharge voltage or peak electron energy. The Langmuir probe trace in the center of the fine-mesh grid indicates essentially an empty bubble while that of the coarse grid shows that electrons and ions entered the bubble. Since the grid forms a closed surface the electrons must have entered through the mesh openings. This implies that the equipotential surfaces $\phi = \text{const}$ are not parallel to the grid and the potential in the center of the mesh openings is insufficient to stop primary electrons of energy eV_{dis} .

The equipotential surfaces between the grid wires depend on the ratio of the Debye length to the wire spacing. As shown in Fig. 29(a), varying the Debye length via the discharge current modifies the bubble properties. The grid voltage is chosen well above the discharge voltage. For low densities or large Debye lengths, electrons are rejected and the frequency of the instability scales like the plasma frequency, $f \propto f_p \propto I_{\text{dis}}^{1/2}$. The frequency drops at $I_{\text{dis}} = 150$ mA and at $I_{\text{dis}} \simeq 200$ mA harmonics appear which are signatures of electrons in the sheath. The floating potential drops from near zero to a value of the discharge voltage. Thus primary electrons have entered the bubble and changed the virtual anode oscillations to a sheath instability with electrons. The mode change also affects the instability amplitude.

Mode changes are also observed as a function of grid voltage. For a plane sheath obeying Child-Langmuir's law the sheath thickness scales proportional to $(eV_{\text{grid}}/kT_e)^{1/4}$, but for a coarse grid the equipotential surfaces have a more complicated 3D geometry. A leaky grid does not control the electron flux like a plane sheath, hence the frequency dependence on grid voltage depends on the grid properties. Figure 40(a) displays $f(V_{\text{grid}})$ for the 3.5 cm diam sphere. Over a wide range of $0 < |V_{\text{grid}}| < 100$ V the grid does not change the

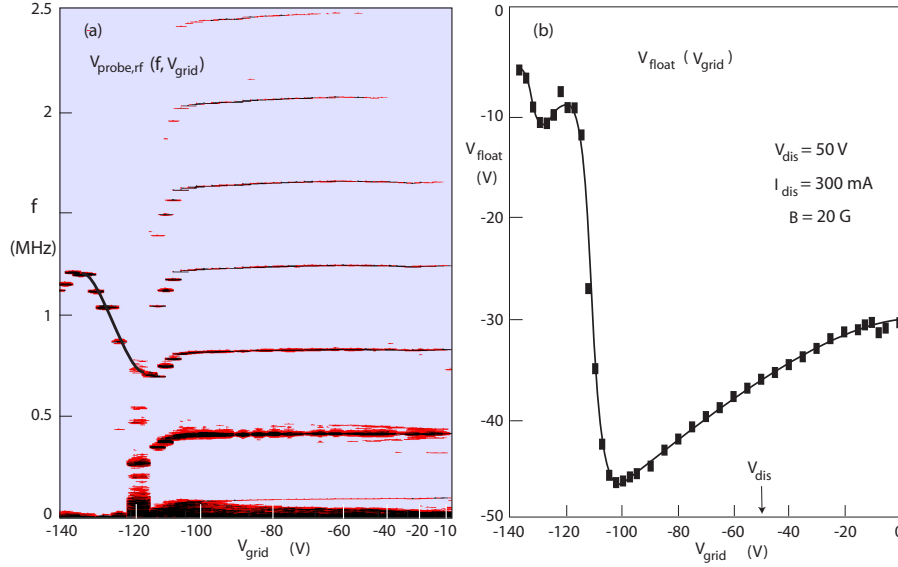


Figure 40. Grid bias variation in a 3.5 cm diam. sphere of coarse mesh. (a) Spectrum of $V_{\text{probe,rf}}$ vs V_{grid} . For $|V_{\text{grid}}| < 110$ V the leaky grid has no control over the electron supply, hence $f=\text{const}$. For $|V_{\text{grid}}| > 110$ V the grid restricts the electron supply which increases the frequency and suppresses harmonics. (b) Floating potential vs V_{grid} showing a sharp rise at $V_{\text{grid}} > -110$ V when the electron leakage stops.

frequency, hence has no control of the electron flux. In this regime the floating potential decreases with grid voltage [Fig. 40(b)]. The plasma potential which is above the floating potential also decreases as V_{grid} becomes more negative. The reason is that the plasma potential adjusts itself to maintain charge neutrality. With increasing $|V_{\text{grid}}|$ the injected electrons have a higher energy and must be slowed down to increase their density which requires a lower plasma potential. At the same time ions are accelerated which lowers their density by flux conservation. The plasma potential drops until the rising electron density matches the decreasing ion density.

When the potential in the mesh openings exceeds the discharge voltage ($V_{\text{grid}} \leq -110$ V) the electron inflow is finally suppressed, the potential rises, the frequency increases with $|V_{\text{grid}}|$ and the harmonics disappear, all signs that the sheath approaches the state of a virtual anode.

The dependence of the floating/plasma potential on V_{grid} is also reflected in the probe current when biased to collect electrons. It has a maximum near or above V_{dis} , depending on grid leakage. In an afterglow plasma the peak decreases and shifts to lower voltages as the electron energy decays.

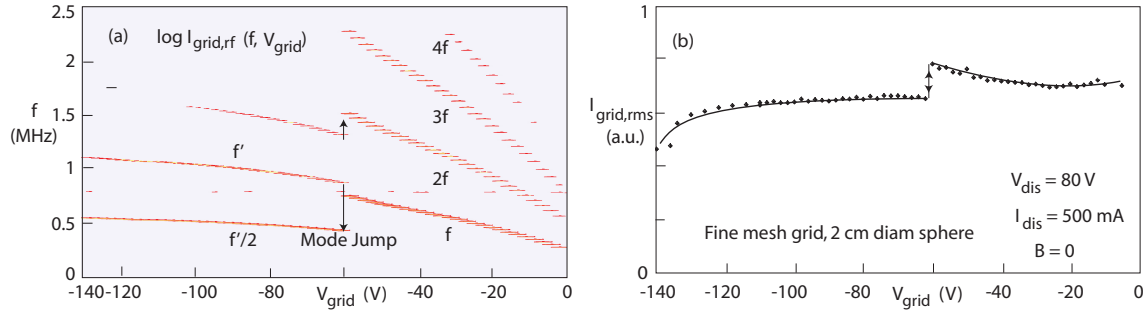


Figure 41. Spectrum of $I_{\text{grid,rf}}$ in a 2 cm diam sphere of *fine mesh* grid, exhibiting a mode jump at $V_{\text{grid}} \simeq -60$ V. (b) Amplitude $I_{\text{grid,rms}}$ vs V_{grid} . The mode jump is not caused by electron leakage through the grid.

4.8.11 Mode Jumps And Sidebands

The instability has been observed to exhibit a jump in frequency and amplitude as a function of V_{grid} . Frequently a subharmonic frequency is excited which in rf driven sheaths is explained by a nonlinear sheath capacitance [34]. The jumps could arise from several mechanisms such as onset of grid leakage, gradients across the bubble creating different sheaths, magnetic field effects, ionization, etc. Here we focus on the grid mesh size.

Figure 41(a) shows a mode jump observed in a 2.5 cm diam sphere made of *fine mesh*. The negative grid bias reduces the electron supply which raises the frequency. At $V_{\text{grid}} \simeq -60$ V the frequency suddenly splits from f to $f' > f$ and to $f'/2$. The amplitude also has a discontinuity [Fig. 41(b)]. The new mode f' has created a subharmonic. Multiple harmonics of $f'/2$ are visible and indicate the presence of electrons in the sheath, even when $|V_{\text{grid}}| > V_{\text{dis}}$. Thus, at a high discharge current of 500 mA even a fine mesh grid leaks electrons into the bubble. The mode jump occurs at $B=0$ hence is not due to magnetic field effects. The mode jump also occurs in a 1 cm diam sphere, hence is not a matter of density gradients across the sphere. There is no hysteresis with V_{grid} , hence it is not an ionization effect.

A second example for mode jumping is shown in Fig. 42(a) which is obtained with the 3.5 cm diam sphere of coarse mesh in a weakly magnetized plasma. The spectrum of grid current oscillations clearly shows a similar frequency jump at $V_{\text{grid}} \simeq -90$ V. The presence of harmonics before and after the jump indicate continued electron leakage when $|V_{\text{grid}}| > V_{\text{dis}}$. Just after the mode jump Fig. 42(b) shows a narrowband spectrum with many harmonics.

A new and interesting feature arises when $|V_{\text{grid}}| \geq 110$ V where a multitude of narrowly spaced sidebands appears on each of the main lines. Figure 42(c) indicates that the sideband spacing is an integral fraction of the fundamental line, typically $\Delta f/f_0 = 1/6$. The spacing is identical for all harmonics, hence the sidebands cannot be created by amplitude modulation of the fundamental. The grid current has no significant low

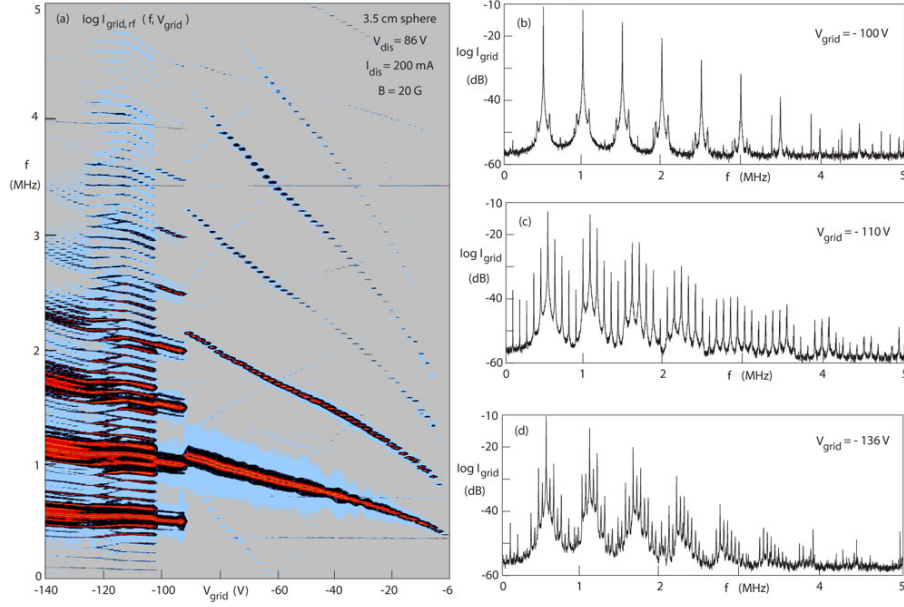


Figure 42. (a) Spectrum of a coarse wire sphere with mode jump and formation of multiple sidebands. (a) $I_{\text{grid,rf}}$ vs f and V_{grid} with subharmonic creation at $V_{\text{grid}} \simeq -95$ V. (b-d) Spectra of $I_{\text{grid,rf}}$ at different V_{grid} showing main instability, sidebands and sub-harmonics.

frequency oscillation at $\Delta f = f_0/6$. In the time domain, the waveform shows a nonsinusoidal fundamental with a nonsinusoidal beat envelope at the sideband frequency. Subharmonic generation also occurs for the sidebands. Figure 42(d) shows that between the first sidebands additional lines with spacing $\Delta f/f_0 = 1/12$ have formed.

The reason for a fixed ratio of the modulation frequency to the sheath oscillation frequency still remains to be determined. Sidebands are not caused by acoustic eigenmodes of the sphere since they also occur for different geometries. They are seen with and without external magnetic field, hence are not due to magnetic effects. Sidebands are only seen for the coarse mesh. It happens to have a ratio of wire thickness to mesh opening is $1/6$. The sheath of a coarse grid is rippled and may exhibit normal and transverse oscillations.

4.9 Recommendations

4.9.1 Further Work

The work above demonstrates that a turbulent layer will be created when ions propagate through a stationary plasma. The turbulence has a spectrum centered about the ion sound frequency and its reproducibility makes it possible to conduct studies on the scattering of electromagnetic waves. As we proposed in an earlier addendum, the logical extension of this work is to launch e-m waves and map their propagation in three-dimensional space in order to fully describe the conversion process outlined in subsec. 3.4.

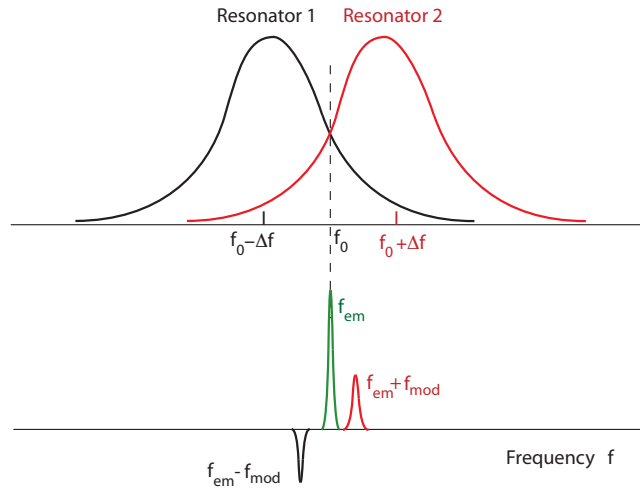


Figure 43. Schematic picture how to eliminate the phase modulation of an electromagnetic wave passing through a noisy plasma.

Another research topic would be to study how the turbulence layer is affected by an obstacle, as demonstrated in subsec. 4.2, and how it affects the scattering of e-m waves. This area of investigation would be useful if there is a need to understand the boundary effect on the scattering processes.

Finally, we could introduce a radially segmented anode inside the source plasma in order to force the source ions to have a well defined difference in velocity in the manner described, for example, by Kaneko et al [35]. Such an anode would establish a potential difference in the separating grid that mirrors the anode geometry thus imparting different accelerating potentials across the sheath of the grid. This would ensure that the ions injected into the stationary target plasma have indeed a shear in velocity and should match more closely the model depicted in Fig. 1 of Sotnikov et al's paper [17].

4.9.2 Proposal To Ameliorate Electromagnetic Scattering Effects

The laboratory experiments suggest a new method to eliminate the modulation of high frequency signals by plasma density fluctuations. The following method is proposed:

It was shown in Fig. 22 that the amplitude modulation of the microwave signal has opposite signs on the rising and falling sides of the resonance curve. Thus, if one microwave signal is applied with frequency $f_0 + \Delta f$, where f_0 is the center frequency and Δf the half width at half maximum, and a second one at $f_0 - \Delta f$, the addition of the two amplitude perturbations with opposite signs would cancel.

Of course, the objective is to eliminate the modulation on a single electromagnetic wave. As schematically shown in Fig. 43, this can be accomplished by using two resonators which are detuned, one to $f_0 + \Delta f$, the other to $f_0 - \Delta f$, where f_0 is now the frequency of

the incident electromagnetic wave, f_{em} . The resonators should be oriented at right angles around their axis so that they are not coupled. The output signals of the two resonators have opposite amplitude polarities when perturbed by the same density modulation. In the high frequency domain of the electromagnetic signal, the sidebands have opposite phases upon passing through the two resonators. This is a consequence of the phase reversal when tuning through a resonance. Thus, the addition of the two phase-modulated signals cancels their sidebands at $f_{em} \pm \Delta f_{mod}$ while the pure center frequency f_{em} remains. This should greatly improve the navigation accuracy when capturing a GPS signal in a noisy plasma.

4.10 ALTERNATE APPROACHES

4.10.1 Introduction

Here we propose an alternate method to produce shear flow instabilities without two ion populations. When an ion beam passes through a stationary plasma and exceeds the ion

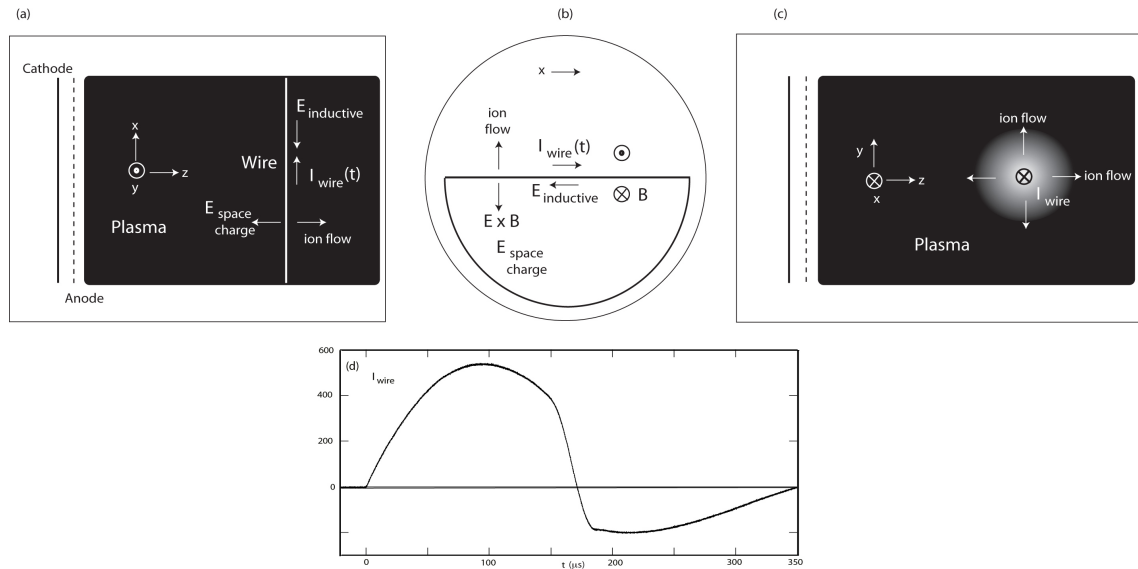


Figure 44. (a) Schematic setup for producing supersonic ion flows with shear. (a) Side view of plasma device, showing cathode and anode for producing a plasma column (in black). An insulated wire traverses the plasma and carries a pulsed current in x-direction. The unmagnetized ions flow are radially away from the wire at supersonic speeds. (b) End view of the device. The rising wire current produces an opposing inductive electric field which together with the B field around the wire causes an electron $E \times B$ drift. The ions are unmagnetized. A radial space charge electric field is created which accelerates the ions radially outward. The ion flow is supersonic and has shear due to the up-down asymmetry produced by the circular return current loop. (c) Side view in the y-z plane showing the radial ion outflow from the wire during the rise of the wire current. (d) Waveform of the wire current. Only the rise up to I_{max} is considered here.

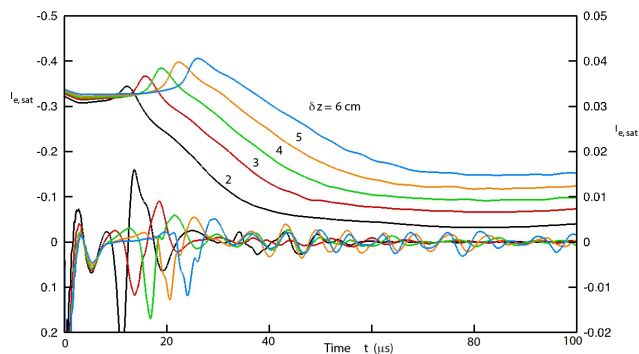


Figure 45. Snapshot of the radial density profile and its fluctuations. The density is proportional to the measured electron saturation current of a small Langmuir probe at $z = 5$ cm from the wire. The peak in the density profile occurs at the front of the expanding plasma. Density fluctuations arise during the ion flow (I_{rms}). The flow depletes the density at the wire and leaves a radial density gradient.

sound speed it is well known to excite an instability. When there is no background plasma a uniform stream of plasma does not excite instabilities. However, just like in other fluids an instability can arise if the fluid velocity exhibits a shear, i.e. the velocity varies orthogonal to its direction. The Kelvin Helmholtz instability is an example of a shear velocity instability.

We have previously investigated the case when an ion beam with shear passes through a stationary background plasma. Observations showed that the shear instability was weak compared to the ion beam-plasma instability. Thus, the effort shifted to creating a flowing plasma without stationary ions. In this plasma ion acoustic waves grew spontaneously. We will first describe the experimental setup, then the observation of ion acoustic turbulence due to velocity shear.

We will conclude with describing further research plans such as microwave scattering off the turbulence and the possible removal of a plasma layer around a reentry vehicle.

4.10.2 Experimental Setup

In order to accelerate a plasma an electric field has to be applied. However, if an electric field is imposed on an unmagnetized plasma the electrons and ions drift in opposite directions which creates a current-driven instability. In order to move electrons and ions in the same direction the electrons have to be magnetized while the ions remain unmagnetized. The electrons are accelerated by a magnetic force across the magnetic field while the ions do not respond to the magnetic force. A space charge electric field arises which accelerates the ions to the same drift speed as the electrons. Variations

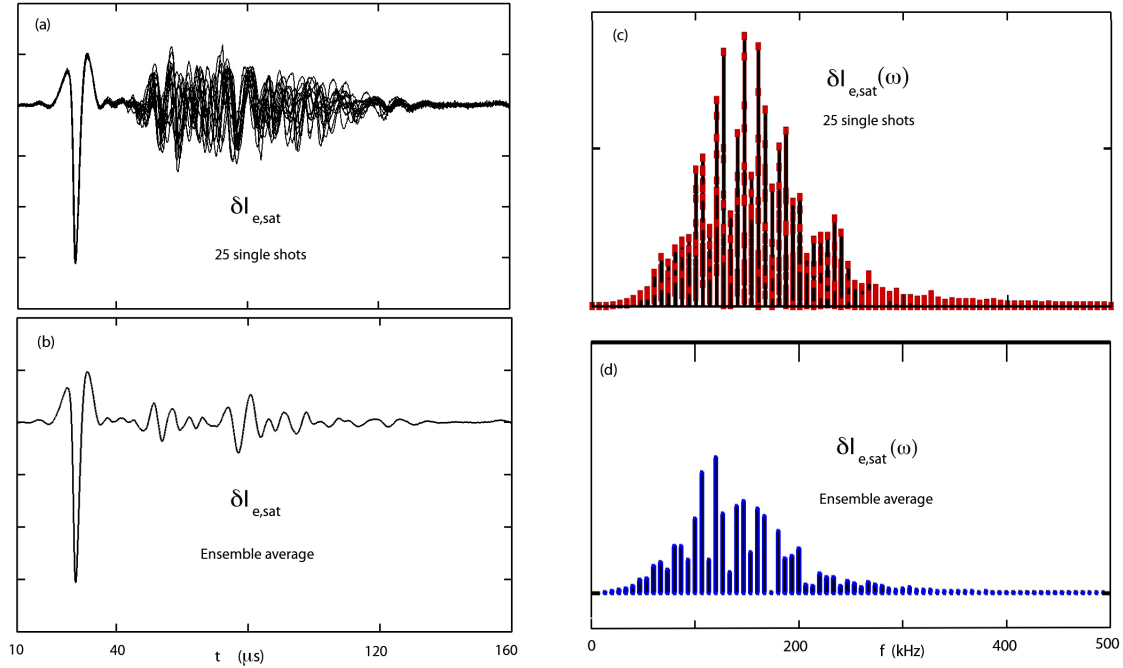


Figure 46. Properties of the density fluctuations in the time and frequency domain. (a) Fluctuations in the electron saturation current ($\propto n_e$) at a fixed position ($y = 0, z = 5$ cm) for 25 repeated shots. The expansion front (first pulse) is repetitive while the waves have amplitude and phase fluctuations. (b) Average over the traces in (a), showing the repetitive part of the waves. (c) Frequency spectra of 25 repeated traces from (a). (d) Frequency spectrum of the averaged waveform which has the same center frequency but fewer high frequency components due to phase mixing by averaging.

perpendicular to the drift velocity create shear and a possible instability.

Figure 44 summarizes the experimental setup. A plasma column is created by a dc discharge between a 1 m diam oxide coated cathode and a gridded anode with about 50 V potential difference. In a magnetic field free region a straight wire is passed across the plasma column as shown in two side views [Fig. 44(a,c)]. An end view shows that the wire current closes in a semicircle parallel to the chamber wall [Fig. 44(b)]. The return current modifies the field symmetry of an infinitely straight line current, resulting in a velocity shear. The wire is insulated and carries a large pulsed current (500 A peak, 100 μs rise time, see Fig. 44(d)).

The rising wire current creates an opposing inductive electric field which together with the magnetic field produces a radial electron $\mathbf{E} \times \mathbf{B}$ drift. As the electrons drift radially away from the wire they leave a positive space charge behind. It creates a radial space charge electric field which accelerates the ions radially away from the wire. All ions near the wire are drifting radially, but not at the same speed. The front ions have the highest velocity since they have experienced the electric field for the longest time. The ions further from

the wire are accelerated later and move slower. The radial ion flow reduces the ion density near the wire and forms a radial density gradient. The radial flow also varies in azimuthal direction since at the same radius the B-field above and below the wire is not identical.

4.10.3 Experimental Results

Figure 45 shows a snapshot of the radial density profile and density fluctuations. The density is obtained from the electron saturation current of a small Langmuir probe at $x = 5$ cm from the wire. The peak in the density profile occurs at the front of the expanding plasma which moves at a velocity $v \simeq 5 \times 10^5$ cm/ μ s which corresponds to Mach 15 for a sound speed of 300 m/s. Density fluctuations arise shortly after the moving front when all ions flow out radially. The ion outflow depletes the density at the wire and leaves a radial density gradient.

Properties of the excited waves are summarized in Fig. 46. The plasma expansion repeats from shot to shot producing the first negative pulse in Fig. 46(a). However, the waves are fluctuating in phase and amplitude for the 25 repeated shots shown. Thus, the waves are not remnant oscillations excited by the expansion front. The waves must be excited by an instability in the flowing plasma. A fraction of the waves show coherency from shot to shot, as seen in the average of Fig. 46(b). The frequency spectra of the waveforms are shown in Figs. 46(c,d). The spectrum peaks in the low ion acoustic branch. The averaging reduces some high frequency components but has a similar center frequency ($f \simeq 150$ kHz) as the individual spectra. Thus, the propagation of the average waveform should be similar to that of the instantaneous waves.

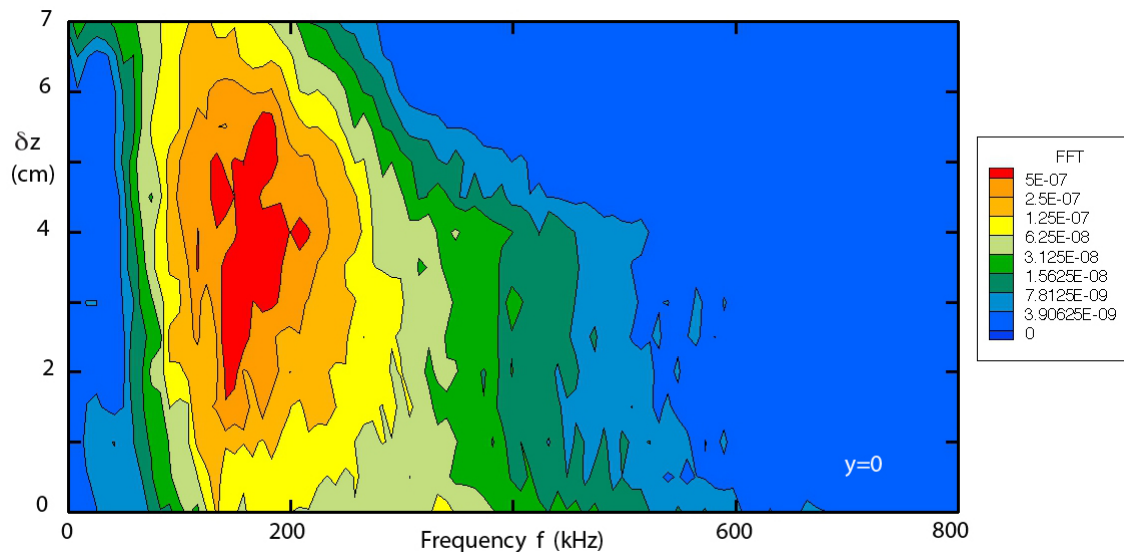


Figure 47. Contours of the Fast Fourier Transform (FFT) of the density fluctuations vs radial position , $\delta I_{e,sat}(f, z, y=0)$. The center of the spectrum shifts slightly due to the radial density gradient.

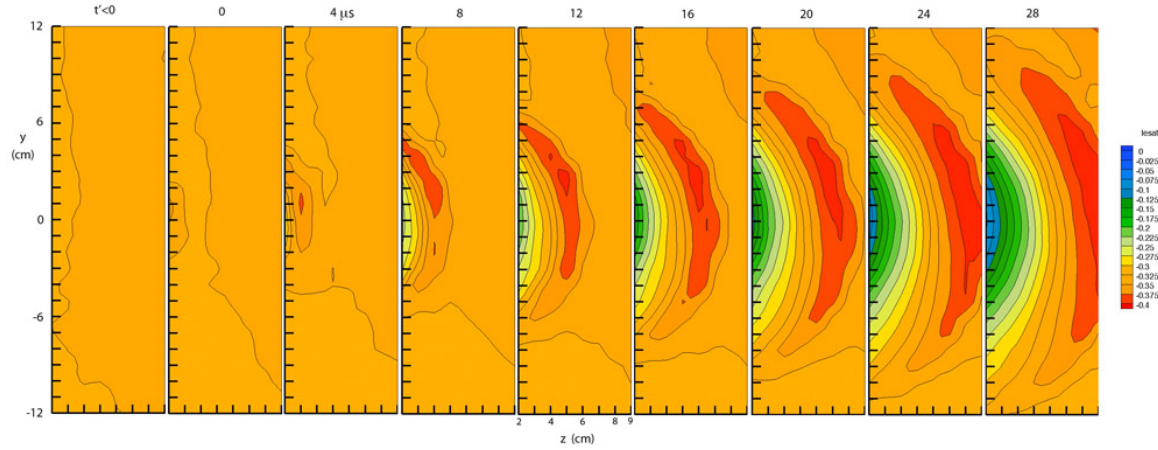


Figure 48. Contour plot of the plasma density in the half plane to the right of the wire, located at $y = z = 0$, taken during the radial plasma expansion front whose peak is the red contour. The density before the expansion ($t' < 0$) and outside the expansion front are uniform and at rest. Between the wire and expansion front the plasma streams radially outward. In this region ion acoustic waves are created. The radial flow has an azimuthal asymmetry hence a shear, $dv_r/d\phi \neq 0$.

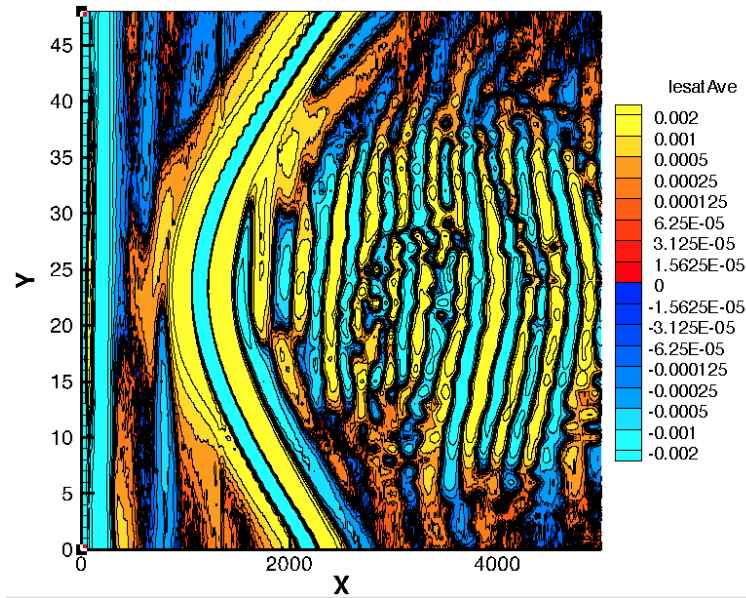


Figure 49. Space-time plot of the density fluctuations. The probe electron saturation current is plotted at $z=3\text{cm}$ vs y and time t during the rise of the wire current. First large contour is the expansion front ($v_y \simeq 5 \times 10^5 \text{ cm}/\mu\text{s}$), followed by a multitude of oscillations during the sheared ion outflow. The wave propagation is not radially outward. The wave properties are obtained from two-probe cross correlations and conditional averaging of probe signals.

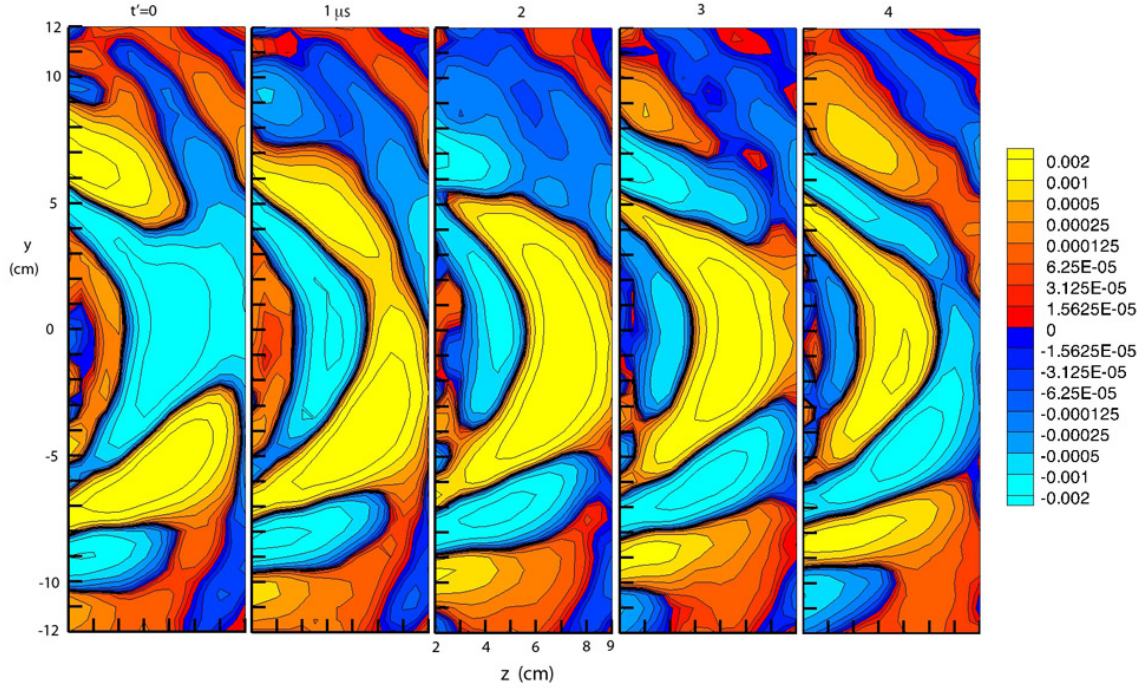


Figure 50. Five consecutive snapshots of averaged density fluctuations in the right half plane of the wire. Wave contours stream from bottom and top toward the mid-plane, forming almost field-aligned phase fronts, then propagating radially inward and outward. Frequency (150 kHz) and wavelength ($\lambda \simeq 2$ cm) show that the waves propagate near the ion sound speed, $c_s \simeq 3 \times 10^5$ cm/ μ s.

Figure 47 displays the Fast Fourier Transform (FFT) of the density fluctuations vs radial position, $\delta I_{e,sat}(f, z, y=0)$. The center of the spectrum shifts slightly due to the radial density gradient. The amplitude decreases with distance since the flow velocity decreases. Very close to the wire the amplitude also vanishes since the plasma has been expelled.

The profile of the total density in two dimensions is presented in Fig. 48 at different times. Contour plot of the electron saturation current is shown in the half plane to the right of the wire, located at $y = z = 0$. It is taken during the radial plasma expansion whose front exhibits a crescent shaped peak (in red). The ions prior to and outside the expansion front are at rest and uniform. Between the wire and expansion front the plasma streams radially outward. It is in this region that ion acoustic fluctuations are created. The radial flow has an azimuthal asymmetry hence a shear, $dv_r/d\phi \neq 0$. The local ion flow velocity \mathbf{v} in space and time can be obtained from the continuity equation, $\nabla \cdot (n\mathbf{v}) + \partial n/\partial t = 0$.

The density fluctuations have been measured vs position and time. Figure 49 shows the cross-correlation between a fixed probe and a movable probe in the y - t plane at $z = 3$ cm from the wire. The first large amplitude which is delayed in $+y$ direction is due to the radially propagating density peak. It is followed by a multitude of oscillations, part of which propagate toward the center and part away from the center. These are the sound

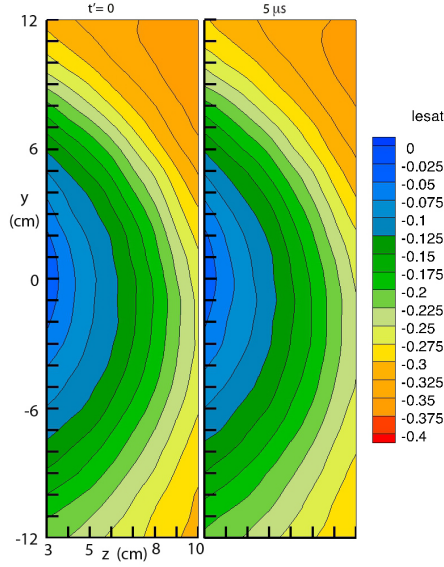


Figure 51. Contours of the plasma density profile in the y-z plane during the time interval of wave propagation. The density profile changes slowly compared to the time scale for wave propagation.

waves which follow the expansion front and are excited in a supersonically propagating ion flow with azimuthal shear. The slope of the first curve yields a propagation velocity $v_y \simeq 5 \times 10^5 \text{ cm}/\mu\text{s}$.

In order to display the wave properties in two dimensions and time a sequence of consecutive shots of the averaged $\delta I_{e,sat}(y, z)$ is shown in Fig. 50. The phase fronts are roughly aligned with the magnetic field that circles around the wire located at $y = z = 0$. But these waves do not propagate radially. Instead they start at the top and bottom ($y = \pm 12 \text{ cm}$, $z = 0$), move toward the center ($y = 0$), from where they propagate radially both in $+z$ and $-z$ direction. Thus, the unstable waves are not simply convected with the radial plasma flow. However, the shear may produce a vortex flow of the plasma which affects the wave propagation.

During the wave propagation time the density profile remains essentially stationary. Figure 51 displays two density contour maps spaced apart by about one rf period. Little change is observed in the density profile, which has therefore no significance for the wave propagation.

4.10.4 Conclusions Of This Experiment And Suggestions For Further Work

In summary, ion sound turbulence has been observed in a supersonic plasma flow with shear. The oscillations have been measured in time, frequency and space.

As soon as contractual support is resumed we can start to perform microwave scattering

off the ion sound turbulence.

We can expand the correlation measurements to three dimensional space to identify the source and mechanism of the instability.

We can lengthen the current rise time to obtain a longer duration of the plasma flow and a wider density depletion. A microwave signal can be propagated from the outside of the plasma toward the wire with a density depletion. If the signal penetrates through the depleted density region the blackout problem is solved. Further details can be found in the literature [24].

4.11 Recent Publications

[20]. "Oscillating plasma bubbles 1. Basic properties and instabilities", R. L. Stenzel and J. M. Urrutia, Phys. Plasmas 19, 082105 (2012). <http://dx.doi.org/10.1063/1.4743019>

[21]. "Oscillating plasma bubbles 2. Pulsed experiments", R. L. Stenzel and J. M. Urrutia, Phys. Plasmas 19, 082106 (2012). <http://dx.doi.org/10.1063/1.4743020>

[22]. "Oscillating plasma bubbles 3. Internal electron sources", R. L. Stenzel and J. M. Urrutia, Phys. Plasmas 19, 082107 (2012). <http://dx.doi.org/10.1063/1.4743021>

[23]. "Oscillating plasma bubbles 4. Grids, gradients and geometry", R. L. Stenzel and J. M. Urrutia, Phys. Plasmas 19, 082108 (2012). <http://dx.doi.org/10.1063/1.4743022>

[24]. "A new method for removing the blackout problem on reentry vehicles", R.L. Stenzel and J. M. Urrutia, Journal of Applied Physics 113 (10), 103303 (2013). <http://dx.doi.org/10.1063/1.4795148>

5. Conclusions

We have conducted experiments designed to test the influence of spatial gradients on the ion acoustic turbulence created when an ion beam propagates through a plasma containing stationary ions. It was found that while there is enhancement on the turbulence, it is not as significant as theoretically predicted. Understanding the physics of the observed turbulence enhancement requires that careful experiments be conducted to explore what is essentially wake physics.

Through the use of in situ probes, the turbulence was characterized and found to consist of waves traveling with the ion beam with frequency centered near the local ion sound speed. A particularly low value of beam energy was found to be an optimum condition for the generation of strongest turbulence, while strong beams were found to generate little to no turbulence. Large amplitude turbulence was driven when the ratio of $n_{\text{beam}}/n_{\text{plasma}}$ was large.

The turbulence was then diagnosed with a microwave resonator probe. The shift of the resonance curve provided a measure of the fluctuation in density caused by the turbulence. Using this diagnostic then provided information on the amount of electro-magnetic wave scattering caused by the turbulence.

Although sound waves are the only low frequency modes in an unmagnetized plasma, it is desirable to verify that the noise consists of ion sound waves. For this purpose, we propose to use two identical probes, at least one of which is movable, and perform cross-correlation measurements. Filtering one frequency component out of the spectrum, the spatial correlation function yields the wavelength such that a dispersion relation ω vs \mathbf{k} can be determined. From probe movements in three dimensions, the \mathbf{k} -vector components will be obtained which specifies the direction of wave propagation [36]. By establishing transverse gradients in the beam, the effects of velocity shear, if any, can be obtained.

This research suggests a possible method to eliminate the scattering of electromagnetic waves that are propagating through the ion sound turbulence region, which is outlined in the next section.

A plasma volume enclosed by a negatively biased grid forms a plasma bubble. Electrons and ions from the ambient plasma leak into the bubble at a rate determined by the grid bias. In steady state, charge neutrality and current closure have to be satisfied and are established self consistently by the sheath or plasma potential. Without current sources or sinks, the bubble draws no current from the ambient plasma. In this case the ion inflow is balanced by an equal ion outflow which conserves particle continuity or a constant density. The latter is determined by partial trapping of ions which is due to scattering from the sheath for oblique incidence. Neutralizing electrons are supplied from the ambient plasma at a rate limited by the grid bias. When the electron supply is reduced, the plasma potential rises which limits the ion supply correspondingly. When all electrons are prevented from entering the bubble, an ion space charge layer or virtual anode forms at the inner sheath which reflects all ions and leaves the bubble empty. Alternatively,

neutralizing electrons can be supplied from an internal electron source such as an emissive probe. It supplies an electron current equal to the total ion current flowing into the bubble which balances ion losses by surface recombination. The emission increases from space charge limited to temperature-limited emission when the electron source is biased below the grid potential. The emitted electrons are no longer trapped and the current closes via the ambient plasma to ground.

The plasma potential in the bubble is observed to oscillate at frequencies below but close to the ion plasma frequency, creating displacement currents in the grid and probes with constant bias. The potential oscillates uniformly throughout the bubble, hence no waves are excited and the potential drop occurs at the inner sheath. The ambient plasma potential does not oscillate, thus the outer sheath is stable and contains no oscillating ion bunches. The instability frequency scales with the ion plasma frequency of the bubble sheath. The frequency depends on the net charge density in the sheath which includes electrons. Since the grid voltage controls the electron supply, it also determines the frequency of oscillations. Furthermore, the grid voltage changes the plasma potential affecting the ion density in the bubble. For increasingly negative grid bias, the frequency first decreases with $|V_{\text{grid}}|$ since the ion density drops. It reaches a minimum for $|V_{\text{grid}}| \simeq V_{\text{dis}}$ when energetic electrons stagnate inside the sheath. For larger $|V_{\text{grid}}|$, the frequency rises and finally approaches virtual anode oscillations. Mode jumps, harmonics and amplitude discontinuities are also observed.

The time-dependence for creating a bubble with its instabilities has been investigated by pulsing relevant plasma parameters. The trapping of electrons in a bubble has been demonstrated by comparing discharge and afterglow plasmas. The instability persists throughout the afterglow without a supply of ambient electrons. From the frequency decay of the sheath instability, the density decay inside the bubble has been found to be comparable to the ambient density decay.

Pulsing the grid voltage yields the time rate for filling and emptying the plasma bubble. The rate is controlled by the lowest particle flux, which is the electron flux for highly negative grid voltages. It is not possible to rapidly modulate the density of a bubble with fast grid voltage pulses.

Inserting biased probes into the bubble upsets the flux balance and thereby perturbs the plasma potential and modifies the sheath oscillations. The I-V characteristics of a Langmuir probe develops a negative differential resistance near the plasma potential and is not useful for diagnostic purposes. A positively biased probe can destroy the electron trapping in an afterglow plasma and raise the instability frequency to that of virtual anode oscillations. Pulsing the probe voltage shows that the time scale for potential relaxation increases as the electron inflow is reduced by biasing the grid more negatively.

Using a short trigger pulse transient sheath oscillations have been excited. Low frequency ringing has been observed for $|V_{\text{grid}}| \leq V_{\text{dis}}$ and explained by transit time effects of ballistic ions through the bubble. For $|V_{\text{grid}}| \geq V_{\text{dis}}$, the sheath instability has been triggered. By comparing the potential oscillations across the sheath, the mechanism of the

instability has been clarified. Due to the limited electron flux ($I_e < I_i$), the ions determine the sheath potential perturbations. Due to inertia, the ions lag by 180° behind the space charge electric field which results in the sheath oscillation. Electrons in the sheath reduce the net space charge which lowers the frequency below the ion plasma frequency. The frequency dependence on V_{grid} is explained by the effects of electrons in the sheath.

The frequency of the instability is frequently discussed in terms of the ion transit time through a sheath which does not address the role of electrons in the sheath [33]. Here we take a different approach and consider the basic oscillation frequency of a charge layer in its own space charge electric field. Ion inertia and space charge density determine the frequency, $\omega^2 = (n_i - n_e)e^2/m_i\epsilon_0$. The oscillation frequency depends on the net space charge density in the sheath, which is determined by *both* ions and electrons. It scales proportional to the ambient ion plasma frequency but drops below it when electrons are present in the sheath. The electron supply is controlled by the grid voltage or other electron sources and sinks. A decreasing electron supply raises the frequency which reaches a maximum for virtual anode oscillations, i.e. a pure ion sheath. Vice versa, an increasing electron supply lowers the frequency as well as the amplitude until the instability is quenched.

The dependence of the instability frequency on grid voltage is not unique. The frequency depends sensitively on the supply of electrons which is not only controlled by the grid voltage but also the emission and collection of electrons by probes. In afterglow plasmas the frequency is independent of the grid potential since it stops the flow of low energy electrons through the grid, provided the grid mesh size is small compared to the Debye length. Coarse grids are leaky to electrons even when the grid potential energy exceeds the electron kinetic energy. If the electron distribution is not isotropic different parts of the grid contribute different electron flows into the bubble which modifies the frequency dependence with grid bias. Multiple sidebands are observed on coarse grids which have 3D equipotential surfaces and could support higher order modes of sheath oscillations.

Mode jumps are commonly observed when the electron supply is decreased. Typically a half frequency mode with multiple harmonics is excited when $|V_{\text{grid}}| \simeq V_{\text{dis}}$. Harmonics are associated with electrons inside the sheath. Since electrons and ions respond differently to an oscillating sheath, electric field the net current is not sinusoidal or monochromatic. Harmonics vanish in afterglow plasmas, at the edge of a magnetized plasma column and in virtual anode oscillations. Mode jumps are not due to the effects of energetic electrons, magnetic fields and grid properties. It also occurs when applied voltages are constant while plasma parameters slowly change, e.g., in afterglow plasmas. Fine structure sidebands are predominantly observed with a coarse mesh and occur only in limited ranges of $|V_{\text{grid}}|$. They are beat phenomena with the same beat period 6:1 which appears to be related to the grid structure. Virtual anode oscillations are typically bursty or broadband since an empty bubble does not couple the locally oscillating sheath regions.

The sheath instability is in many respects similar to that observed in double plasma devices [37, 38, 39, 33, 40, 41]. The explanations for the instability mechanism differ widely [42, 43, 44]. Here we consider the oscillation frequency of a charge layer in its

own space charge electric field. Ion inertia and *net* space charge density determine the frequency, $\omega^2 = (n_i - n_e)e^2/m_i\epsilon_0$. The presence of electrons in the sheath lowers the oscillation frequency below the ion plasma frequency, as observed experimentally. It is controlled by the grid voltage or other electron sources and sinks. In general, a frequency decrease indicates an increased electron supply or a decreased ion supply. Without neutralizing electrons virtual anode oscillations are observed which have the highest frequency. The strongest instability usually arises for $|V_{\text{grid}}| \simeq V_{\text{dis}}$ where the entire bubble potential oscillates, creating harmonics, subharmonics and sideband eigenmodes. These global oscillations lock to the most unstable mode producing a fairly monochromatic instability in spite of gradients across the grid. A large electron flux stabilizes the sheath, as in the case of the outer grid sheath. There is no evidence for traveling potential relaxation processes [39] or beam-plasma instabilities.

As regards applications a small bubble could be used for diagnostics of fast electrons which produce a frequency minimum for $f(V_{\text{grid}})$ at the peak electron energy. In a larger pulsed bubble, the expansion of ions into vacuum can be modeled. Electrostatic confinement has been demonstrated for electrons with energy lower than given by the negative grid voltage. The same holds for ion confinement by a virtual anode on the outside grid when the discharge is produced inside the bubble and no neutralizing electrons are outside the bubble. With neutralization the setup would become a Kaufman ion source, useful for ion-surface interaction in spherical or cylindrical geometries.

Further experimental research is needed to establish the physics of harmonic and subharmonic generation, sidebands, mode jumps and instability gaps. Wave propagation in a bubble with trapped particles have not yet been investigated. Bubbles in rf discharges or in dusty plasmas have neither been explored.

6. References

- [1] R.A. Hartunian, G. E. Stewart, S.D. Fergason, T. J. Curtiss, and R. W. Seibold. Causes and mitigation of radio frequency (rf) blackout during reentry of reusable launch vehicles. Aerospace Report ATR-2007(5309)-1, The Aerospace Corporation, 2007. Available from the Federal Aviation Administration's Office of Commercial Space Transportation.
- [2] F. P. Russo and J. K. Hughes. Measurements of the Effects of Static Magnetic Fields on VHF Transmission in Ionized Flow Fields. Technical Report TM X-907, NASA, March 1964. Available at NASA Technical Reports Server, <http://ntrs.nasa.gov/>.
- [3] K. M. Lemmer, A. D. Gallimore, and T. B. Smith. Using a helicon source to simulate atmospheric re-entry plasma densities and temperatures in a laboratory setting. *Plasma Sources Sci. Technol.*, 18(2):0250198, 2009.
- [4] K. M. Lemmer. *Use of a Helicon Source for Development of a Re-Entry Blackout Amelioration System*. PhD thesis, The University of Michigan, 2009.
- [5] M. K. Kim. *Electromagnetic Manipulation of Plasma Layer for Re-Entry Blackout Mitigation*. PhD thesis, The University of Michigan, 2009.
- [6] N. D'Angelo and S. v. Goeler. Investigation of the Kelvin-Helmholtz instability in a cesium plasma. *Phys. Fluids*, 9(2):309–313, 1966.
- [7] G. Ganguli, S. Slinker, V. Gavrishchaka, and W. Scales. Low frequency oscillations in a plasma with spatially variable field-aligned flow. *Phys. Plasmas*, 9(5):2321–2329, 2002.
- [8] P. A. Bernhardt, G. Ganguli, M. C. Kelley, and W. E. Swartz. Enhanced radar backscatter from space shuttle exhaust in the ionosphere. *J. Geophys. Res.*, 100(A12):23,811–23,818, 1995.
- [9] S. Depierreux, C. Labaune, J. Fuchs, and H. A. Baldis. Application of Thomson scattering to identify ion acoustic waves stimulated by the Langmuir decay instability. *Rev. Sci. Instrum.*, 71(9):3391–3401, 2000.
- [10] R. J. Taylor, K. R. MacKenzie, and H. Ikezi. A large double plasma device for plasma beam and wave studies. *Rev. Sci. Instrum.*, 43(11):1675–1678, 1972.
- [11] D. Grésillon and F. Doveil. Normal modes in the ion-beam-plasma system. *Phys. Rev. Lett.*, 34(2):77–80, 1975.
- [12] T. Honzawa. Controlled excitation and dispersion relations of nonlinear multimode waves in ion-beam-plasma system. *J. Phys. Soc. Jpn.*, 57(11):3802–3808, 1988.
- [13] J. L. Chau and E. Kudeki. First E- and D-region incoherent scatter spectra observed over Jicamarca. *Ann. Geophys.*, 24(5):1295–1303, 2006.

- [14] J. Willig, R. L. Merlino, and N. D'Angelo. Experimental study of the parallel velocity shear instability. *Physics Letters A*, 236(3):223–226, 2006.
- [15] C. Teodorescu, E. W. Reynolds, and M. E. Koepke. Experimental verification of the shear-modified ion-acoustic instability. *Phys. Rev. Lett.*, 88(18):185003, 2006.
- [16] P. J. G. Perron, J.-M. A. Noël, and J.-P. St.-Maurice. Velocity shear and current driven instability in a collisional F-region. *Ann. Geophys.*, 27(1):381–394, 2009.
- [17] V. I. Sotnikov, J. N. Leboeuf, and S. Mudaliar. Scattering of electromagnetic waves in the presence of wave turbulence excited by a flow with velocity shear. *IEEE Trans. Plas. Sci.*, 38(9):2208–2218, 2010.
- [18] R. J. Taylor, K. R. MacKenzie, and H. Ikezi. A large double plasma device for plasma beam and wave studies. *Review of Scientific Instruments*, 43(11):1675 – 1678, 1974.
- [19] A. Rohde, A. Piel, and H. Klostermann. Simulation of the nonlinear dynamics of grid sheath oscillations in double plasma devices. *Phys. Plasmas*, 4:3933, 1997.
- [20] R. L. Stenzel and J. M. Urrutia. Oscillating plasma bubbles. I. Basic properties and instabilities. *Phys. Plasmas*, 19:082105–1–10, 2012.
- [21] R. L. Stenzel and J. M. Urrutia. Oscillating plasma bubbles. II. Pulsed experiments. *Phys. Plasmas*, 19:082106–1–10, 2012.
- [22] R. L. Stenzel and J. M. Urrutia. Oscillating plasma bubbles. III. Internal electron sources and sinks. *Phys. Plasmas*, 19:082107–1–10, 2012.
- [23] R. L. Stenzel and J. M. Urrutia. Oscillating plasma bubbles. IV. grids, geometry and gradients. *Phys. Plasmas*, 19:082108–1–10, 2012.
- [24] R. L. Stenzel and J. M. Urrutia. A new method for removing the blackout problem on reentry vehicles. *J. Appl. Physics*, 113(10):103303, 2013.
- [25] Y. Nakamura, Y. Nomura, and R. L. Stenzel. Sheath expansion of plane probe by ion-beam reflection. *J. Appl. Physics*, 52(3):1197–1201, 1981.
- [26] R. L. Stenzel. Microwave resonator probe for localized density measurements in weakly magnetized plasmas. *Rev. Sci. Instr.*, 47(5):603–607, 1976.
- [27] I. G. Kondratev, A. V. Kostrov, A. I. Smirnov, A. V. Strikovskii, and A. V. Shashurin. Two-wire microwave resonator probe. *Plasma Phys. Rep.*, 28(11):900–905, 2002.
- [28] R. B. Piejak, V. A. Godyak, R. Garner, B. M. Alexandrovich, and N. Sternberg. The hairpin resonator: A plasma density measuring technique revisited. *J. Appl. Phys.*, 95(7):3785, 2004.

- [29] H. J. Hartfuss, T. Geist, and M. Hirsch. Heterodyne methods in millimetre wave plasma diagnostics with applications to ECE, interferometry and reflectometry. *Plasma Phys. Control. Fusion*, 39(11):1693-1769, 1997.
- [30] R. L. Stenzel. Experiments on current-driven three-dimensional ion sound turbulence. II. Wave dynamics. *Phys. Fluids*, 21(1):99-108, 1978.
- [31] R. L. Stenzel and J. M. Urrutia. Pulsed currents carried by whistlers. VIII. Electrode current disruptions by plasma erosion. *Phys. Plasmas*, 4(1):26-35, 1997.
- [32] R. L. Stenzel, M. Ooyama, and Y. Nakamura. Potential double layers formed by ion beam reflection in magnetized plasmas. *Phys. Fluids*, 24:708-718, 1981.
- [33] A. Piel, H. Klostermann, A. Rohde, N. Jelic, and R.W. Schrittwieser. Ion sheath oscillations in double plasma machines. *Physics Letters A*, 216(6):296-302, 1994.
- [34] P.A. Miller, L.A. Romero, and P.D. Pochan. Subharmonics and rf-plasma sheaths. *Phys. Rev. Lett.*, 71:863-866, 1993.
- [35] T. Kaneko, Y. Odaka, E. Tada, and R. Hatakeyama. Generation and control of field-aligned flow velocity shear in a fully ionized collisionless plasma. *Rev. Sci. Instrum.*, 77(12):4218-4222, 2002.
- [36] R. L. Stenzel. Experiments on current-driven three-dimensional ion sound turbulence. I. Return-current limited electron beam injection. *Phys. Fluids*, 21(1):93-98, 1978.
- [37] P. J. Barrett and R. G. Greaves. Double-plasma instability near the ion plasma frequency. *Phys. Fluids*, B 1:1776, 1989.
- [38] J. Chutia, S. Sato, H. Kubo, and Y. Nakamura. Low-frequency instability excited by a mesh grid in a double-plasma device. *Journal of Plasma Physics*, 46(3):463-471, 1991.
- [39] G. Popa and R. Schrittwieser. Resonant coupling between ion bounce in a potential well and the potential relaxation instability. *Physics of Plasmas*, 1(1):32, 1994.
- [40] A. Sarma, H. Bailung, and J. Chutia. Characteristics of sheath instability in a double plasma device. *Phys. Plasmas*, 4:61, 1997.
- [41] H. Klostermann, A. Rohde, and A. Piel. Van der pol behavior of virtual anode oscillations in the sheath around a grid in a double plasma device. *Physics of Plasmas*, 4(7):2406, 1997.
- [42] T.E. Sheridan. Model for ion oscillations at a negatively-biased grid. *Physics Letters A*, 235(3):253-258, 1997.
- [43] C. B. Dwivedi, R. A. M. Prakash, and V. M. Bannur. Theoretical model for ion-rich sheath driven low frequency instability. *Physica Scripta*, 60(2):166, 1999.

- [44] B. P. Pandey and S. Roy. An explanation of the sheath instability. *Phys. Plasmas*, 10(1):5–8, 2003.